UNIVERSITÄT
KOBLENZ · LANDAU

Reconstruction and Visualization of Neuronal Pathways with Applications in Neuroscience

**Vom Promotionsausschuss des Fachbereichs 4: Informatik
an der Universität Koblenz-Landau
zur Verleihung des akademischen Grades
Doktor der Naturwissenschaften (Dr. rer. nat.)
genehmigte**

DISSERTATION

von

Dipl.-Inform. Diana Röttger

Koblenz - 2012

Abstract

Diffusion imaging captures the movement of water molecules in tissue by applying varying gradient fields in a magnetic resonance imaging (MRI)-based setting. It poses a crucial contribution to in vivo examinations of neuronal connections: The local diffusion profile enables inference of the position and orientation of fiber pathways. Diffusion imaging is a significant technique for fundamental neuroscience, in which pathways connecting cortical activation zones are examined, and for neurosurgical planning, where fiber reconstructions are considered as intervention related risk structures.

Diffusion tensor imaging (DTI) is currently applied in clinical environments in order to model the MRI signal due to its fast acquisition and reconstruction time. However, the inability of DTI to model complex intra-voxel diffusion distributions gave rise to an advanced reconstruction scheme which is known as high angular resolution diffusion imaging (HARDI). HARDI received increasing interest in neuroscience due to its potential to provide a more accurate view of pathway configurations in the human brain.

In order to fully exploit the advantages of HARDI over DTI, advanced fiber reconstructions and visualizations are required. This work presents novel approaches contributing to current research in the field of diffusion image processing and visualization. Diffusion classification, tractography, and visualizations approaches were designed to enable a meaningful exploration of neuronal connections as well as their constitution. Furthermore, an interactive neurosurgical planning tool with consideration of neuronal pathways was developed.

The research results in this work provide an enhanced and task-related insight into neuronal connections for neuroscientists as well as neurosurgeons and contribute to the implementation of HARDI in clinical environments.

Kurzfassung

Die Diffusionsbildgebung misst die Bewegung von Wassermolekülen in Gewebe mittels variierender Gradientenfelder unter Verwendung der Magnetresonanztomographie (MRT). Diese Aufnahmetechnik stellt eine große Chance für in vivo Untersuchung von neuronalen Bahnen dar, da das lokale Diffusionsprofil Rückschlüsse über die Position und Richtung von Nervenbahnen erlaubt. Zu den Anwendungsgebieten der Diffusionsbildgebung zählt die Grundlagenforschung in den Neurowissenschaften, in denen Nervenbahnen als Verbindungen kortikaler Areale bestimmt werden, und die neurochirurgische Operationsplanung, in der rekonstruierte Bahnen als Risikostrukturen für Interventionen angesehen werden.

Die Diffusionstensor-MRT (DT-MRT) ist aufgrund ihrer schnellen Aufnahme- und Rekonstruktionsgeschwindigkeit derzeitig klinischer Standard zur Bestimmung von Nervenbahnen. Jedoch erlaubt die DT-MRT nicht die Darstellung von komplexen intravoxel Diffusionsverteilungen. Daher etablierte sich eine weitere Modellierungstechnik, die als High Angular Resolution Diffusion Imaging (HARDI) bekannt ist. HARDI-Techniken erhielten wachsendes Interesse in den Neurowissenschaften, da sie großes Potential zur exakteren Darstellung der Nervenbahnen im menschlichen Gehirn besitzen.

Um die Vorteile von HARDI-Techniken gegenüber DT-MRT voll auszuschöpfen, werden fortgeschrittene Methoden zur Rekonstruktion und Visualisierung der Bahnen benötigt. In der vorliegenden Arbeit werden neue Techniken vorgestellt, welche zur aktuellen Forschung hinsichtlich der Verarbeitung und Visualisierung von Diffusionsbildgebungsdaten beitragen. Ansätze zur Klassifizierung, Traktographie und Visualisierung wurden entwickelt um eine aussagekräftige Exploration neuronaler Bahnen und deren Beschaffenheit zu ermöglichen. Des Weiteren wurde eine interaktive Software für die neurochirurgische Operationsplanung implementiert, welche Nervenbahnen als Risikostrukturen berücksichtigt.

Die vorgestellten Forschungsergebnisse bieten einen erweiterten und aufgabenorientierten Einblick in neuronale Verbindungen sowohl für Neurowissenschaftler als auch für Neurochirurgen und tragen zum Einsatz von HARDI-Techniken in einer klinischen Umgebung bei.

Contents

II   Diffusion profile classification   63

4   HARDI-based diffusion characteristics   65

III   Neuronal pathway reconstruction   87

5   Tractography   89

VI Conclusion 177

List of Abbreviations and Symbols

Abbreviations

3D	three-dimensional
ISMI	isotropic single multiple diffusion classification index
MFC	morphological fiber classifier
AD	Alzheimer's disease
ADC	apparent diffusion coefficient
CBT	corticobulbar tract
CC	corpus callosum
CR	corona radiata
CSD	constrainted spherical deconvolution
CST	corticospinal tract
dODF	diffusion orientation distribution function, also written as ODF
DSI	diffusion spectrum imaging
DTI	diffusion tensor imaging
DWI	diffusion weighted imaging
FACT	fiber assignment by continuous tracking
FLAIR	fluid attenuated inversion recovery
fMRI	functional magnetic resonance imaging
fODF	fiber orientation distribution function
FRT	Funk-Radon transform

GD   diffusion gradient pulse

HARDI   high angular resolution diffusion imaging

MCI   mild cognitive impairment

MFACT   multiple fiber assignment by continuous tracking

MFG   middle frontal gyrus

MRI   magnetic resonance imaging

MS   multiple sclerosis

ODF   orientation distribution function

PDD   principal diffusion direction

PDF   probability density function

PGSE   pulsed gradient spin-echo

QBI   Q-ball imaging

RF   radiofrequency pulse

S1   primary somatic sensory area

SD   spherical deconvolution

SE   spin echo

SLF   superior longitudinal fasciculus

SNR   signal to noise ratio

TMS   transcranial magnetic stimulation

Symbols

Δ diffusion time, time between two gradient pulses

δ gradient pulse duration time

γ gyromagnetic ratio

$\lambda_1, \lambda_2, \lambda_3$ eigenvalues of the diffusion tensor

$\mathbf{D}$ diffusion tensor

$\mathbf{d}$	displacement vector
$\mathbf{e_1}, \mathbf{e_2}, \mathbf{e_3}$	eigenvectors of the diffusion tensor
$\mathbf{G}$	diffusion gradient vector
$\mathbf{q}$	diffusion gradient
$\mathbf{T}$	Tesla
$\mathbf{u}$	diffusion direction of interest
ω	Larmor frequency
$\Psi(\mathbf{u})$	ODF for direction $\mathbf{u}$
τ	effective diffusion time
$\vec{\mathbf{B}}$	applied magnetic field in MRI
$|\mathbf{d}|$	distance of molecule displacement
b_0	baseline image: MRI sequence without applied diffusion gradient and a b-value of 0
D	diffusion coefficient
N	number of observed molecules
n	number of displaced molecules
$P(\mathbf{d}, t)$	diffusion probability distribution function
S	diffusion signal
S_0	signal in absence of diffusion gradients
t_0	initial point in time
b	b-value
q-space	three-dimensional coordinate system, organizing diffusion acquisitions defined by $\mathbf{q}$

List of Figures

List of Tables

List of Code Examples

Acknowledgements

"We need only view a Dissection of that large Mass, the Brain, to have ground to bewail our Ignorance... We admire... the Fibres of every Muscle, and ought still more to admire their disposition in the Brain, where an infinite number of them contained in a very small Space, do each execute their particular Offices without confusion or disorder."
– Nicolaus Steno, 1669

Part I

Introduction

1 Background and organization

1.1 Motivation

The Brownian motion of water molecules in fibrous material such as muscles or brain white matter is restricted and thus anisotropic. Diffusion imaging is a magnetic resonance imaging (MRI)-based technique, utilizing the directionality of molecular movement and is thereby able to characterize organized tissue. It poses a large achievement in neuroscience since it is currently the only non-invasive technique to gain information about the course and integrity of neuronal pathways in vivo.

Applications of diffusion imaging include fundamental neuroscience and neurosurgical planning. In fundamental neuroscience, information about activation area connectivity via white matter fibers is crucial. Neuronal connections obtained by diffusion imaging answer important questions such as: Which cortical zones are potentially involved in a certain task? A further neuroscientific application is neurosurgical planning, a preoperative stage in which risk structures are examined and access paths are defined in order to minimize postoperative damages. White matter pathways pose such risk structures since cortical activation zones are connected via neuronal fibers; they are also responsible for signal transfer and therefore, enable communication amongst activation zones. As a result, harming connections disables communication and damage to both causes severe patient impairment.

Diffusion tensor imaging (DTI) is the widely used technique, representing the acquired signal with a second order tensor. This model assumes a Gaussian diffusion process and reconstructs a probability density function (PDF). The PDF describes the diffusion distribution of water molecules within one voxel by using the minimum of six MRI gradient directions. Tractography techniques esti-

mate trajectories using the principal eigenvector of the diffusion tensor. The resulting pathways are considered to approximate fiber courses and are the most common diffusion imaging visualization used by clinicians. However, in regions with complex fiber distributions, a DTI diffusion profile is unable to adequately model the underlying fiber structure. The Gaussian assumption only supports a single diffusion magnitude within one voxel. Therefore, more sophisticated models were developed, such as high angular resolution diffusion imaging (HARDI), to overcome the limitations of DTI. Most characteristic for HARDI techniques is the use of up to a few hundred gradients and a higher b-value to acquire the diffusion signal. Several reconstruction algorithms using this signal exist. Their outcome, the so called orientation distribution function (ODF), is a spherical probability function which describes the underlying diffusion profile.

As a result of the detailed diffusion profile, HARDI is more advantageous than DTI for in vivo white matter examination. The contribution of advanced fiber visualizations to neuroscience and neurosurgery is the topic of ongoing research. Resulting from the ability to acquire and model complex diffusion patterns, various issues in terms of diffusion image processing as well as visualization emerged: First, a significant description of intra-voxel diffusion patterns in the form of diffusion indices is needed. DTI classifiers are no longer sufficient to describe the advanced diffusion distribution function. Second, the huge contribution of HARDI is the ability to resolve complex fiber distributions. Novel white matter tract reconstruction algorithms have to be designed in order to take full advantage of the information provided by the HARDI diffusion profile. Third, advanced visualization approaches are required in order to facilitate white matter exploration. HARDI-based fiber pathways are intricate and simple line visualizations are no longer intuitive. Subsequently, the contribution of diffusion imaging to many neuroscientific questions is an open issue.

1.2 Contribution

The developed and here presented approaches are contributions to an active field of research and complete the diffusion data analysis pipeline, ranging from diffusion data processing steps and visualizations to neurosurgical and neuroscientific applications. Figure 1.1 shows the main contributions of this thesis: Approaches are categorized and named, and the scientific conferences in which they were published indicated. The according sections in this thesis are included as well as illustrations showing representative visualizations. All contributions are built on each other and are presented successively in the following:

1. **HARDI Analysis - Diffusion Classifiers**
   The ODF describes the distribution of water molecules within a voxel. However, the spherical probability function is of a complex nature and not easy for clinicians to interpret. This is where diffusion indices contribute and provide crucial information in terms of anisotropy and intra-voxel diffusion profiles. Two ODF-based indices were developed in the course of this thesis and published in [101] and [95]. Both classifiers have the same goal: The discrimination of voxels containing no white matter structures or a single, two or multiple fiber pathway distributions.

2. **Fiber Reconstruction - Tractography**
   The most intuitive visualization of diffusion data is the reconstruction of anatomically meaningful fiber bundles which characterize certain neuronal pathways. Tractography techniques benefit from the detailed information provided by the ODF. However, multiple fiber populations in one voxel lead to more than one ODF maximum and hence require novel, more sophisticated tractography approaches than those existing for DTI. Using algorithms designed for one diffusion direction wastes the additional information. Therefore, a tractography approach for HARDI was developed and published [100]. The algorithm evaluates local and global white matter properties for streamline propagation. The approach was evaluated by computing pathways of a hardware phantom with known ground truth

information, as well as fibers running in the *centrum semiovale*, a region in the human brain comprising challenging pathway configurations.

3. **Visualization - Advanced Fiber Rendering**
   Line representations of HARDI tractography approaches are more complex than those resulting from DTI since multiple fibers potentially run within one voxel. For this reason, visualizations often suffer from visual clutter. An advanced line rendering approach was developed and published in [93] in order to enhance spatial depth perception and facilitate diffusion data interpretation. Proposed methods include spatial depth enhancing techniques as well as diffusion classifier colormapping.

4. **Visualization - Intra-Bundle Diffusion Characteristics**
   In neurosurgical examinations clinicians are interested in the extent of certain bundles. For this reason, a pipeline was designed in which fiber encompassing hulls were computed. Subsequently, they are used to visualize intra-bundle diffusion characteristics, with the aim of improving tract-related examinations. Illustrative rendering and lighting approaches were applied in order to enhance 3D perception. A clinical study was designed in which the proposed visualizations were evaluated by neuroscientists. Questions concerning the general understanding of the methods, the spatial perception of the enhancements, and possible applications in neuroscience were discussed. Parts of the approach were published in [94] and a clinical evaluation in [96].

5. **Visualization - Focus and Context Rendering**
   Visualizations combining both fiber and bundle renderings provide crucial context information about the global bundle structure. At the same time they are able to encode characteristics about fiber properties such as the local degree of anisotropy or details concerning inner-bundle fiber configurations. A focus and context approach for diffusion visualizations was designed and published in [99].

6. **Neurosurgical Application - Multimodal Visualization**
   In terms of neurosurgical examinations for brain tumor resection, multiple

datasets such as DTI, fMRI, as well as contrast enhanced and anatomical MRI are acquired. Certain structures represented in different datasets have to be considered in conjunction for efficient data exploration and intervention planning. However, the simple combination of all datasets suffers from visual cluttering and therefore, requires an intelligent multimodal visualization approach. Methods unifying the multivalued volumes in an intuitive and resection-focused visualization were developed including an evaluation of potential risk structures. In this context, a tool was realized providing the surgeon with enhanced insights into the neurosurgical case in order to define and examine risk structures. Parts of the multimodal visualization approaches were published in [98] and as a submission to the IEEE Visualization Contest 2010 in [97].

7. **Neurosurgical Application - Preoperative Planning**
After combining all relevant information within one visual representation, the next step is to develop a user-friendly and target-oriented interaction method in which the surgeon determines the most adequate access path to the lesion. To accomplish this task, the multimodal visualization tool was extended to define and highlight potential risk structures with respect to an access path, but avoid visual cluttering. Parts of the developed access path planning metaphors were published in the course of the IEEE Visualization Contest 2010 in [97] and in [98].

An in-depth understanding of diagnostic processes, therapeutic decisions, and intraoperative information is achieved by medical visualizations [82]. Enhanced visualization of spatial as well as functional properties of structures is beneficial: The available time for diagnosis and therapy planning is a well-known issue in most clinical environments. Using advanced visualization techniques in order to highlight significant characteristics of the respective medical case poses a huge contribution. The resulting representations facilitate a faster understanding and assessment. For example 3D visualizations reveal the spatial relation between structures of interest and thereby, the mental fusion of individual 2D scans becomes obsolete. Furthermore, medical visualizations guide the users attention to significant features, such as visual encodings of the bundle

integrity in terms of diffusion imaging. Visualizations provide the potential not only to save vital time but also to reveal important findings.

Commonly, medical visualization approaches include the following steps: Analysis of clinical questions as well as state of the art methods, software design and implementation, and a subsequent evaluation of the software in the course of a user study. These steps are performed in close clinical collaboration and often iteratively since evaluation leads to new feature requirements. Many factors, such as advanced acquisition techniques and their clinical implementation influence research in medical image processing and visualization. In the here presented work, the focus is to discuss the contribution of HARDI to neuroscience and to develop innovative diffusion image processing and visualization approaches. A further contribution is the implementation of 3D visualizations with respect to specific neurosurgical questions. The presented object of research includes novel and innovative approaches which are currently not applied in clinical routine examinations. In the case of HARDI, this is due to long acquisition and reconstruction times as well as the fact that optimal acquisition parameters are not completely defined. In the case of visualization, 2D slice representations are still popular in everyday clinical examinations. This is because they do not require any preprocessing and clinicians are familiar with them. On the other hand, many medical questions take advantage of 3D image processing and visualization methods. In fact, image processing and computer graphics techniques offer a great variety of algorithms, applicable to medical datasets. These approaches facilitate a fast data interpretation and thereby, provide more detailed insights into the data. In order to make a contribution to ongoing research, novel methods beyond those implemented in todays clinical settings are needed. The development of innovative approaches, which aim to solve current clinical questions, influence future data processing and is meaningful even though not yet considered for routine examinations.

Summarizing, neither HARDI nor 3D medical visualization is applied in everyday examinations and further research is required. However, both have great potential to answer vital questions in neuroscience. This work concentrates on discussing aspects and presenting innovative ideas in order to contribute to both challenges. A detailed evaluation with respect to applications in

everyday clinical examinations is however, beyond the scope of this thesis and is therefore not performed.

The presented approaches were realized using *MeVisLab*, a development environment for medical image processing and visualization. It was developed and is used by MeVis Medical Solutions AG and Fraunhofer MEVIS in Bremen, Germany [65].

1.3 Organization

The organization of the developed approaches is presented in the following. Topics are divided into 4 parts: Part II discusses two indices for ODF classification. A tractography approach for HARDI using the previously introduced HARDI classifier follows in Part III. Part IV comprises three visualization approaches for white matter structures: single fiber and bundle illustrations as well as a combined approach using focus and context rendering methods. Part V introduces a system for neurosurgical planning.

Part I - Chapters 2 and 3 provide the medical motivation and background information for neuronal pathway reconstruction as well as basic knowledge for understanding diffusion imaging and HARDI.

Part II - Chapter 4 introduces the developed classifier for ODF characterization: a global approach called *MFC* in Section 4.5 and an ODF-based index called *ISMI* in Section 4.6. These classifiers are designed to differentiate gray matter from white matter. In the case of gray matter the distribution is isotropic. However, in the case of white matter, the proposed indices successfully separate into further compartments: single or multiple fiber distribution. Based on a white matter mask, the idea of *MFC* is to morphologically eliminate voxels in such a way that only clusters remain. These clusters represent an estimation of regions containing multiple fiber populations. *ISMI* consists of a computation pipeline, where white and gray matter are distinguished by analyzing the deviation of the ODF from a sphere defined by the maximal radius of the ODF. This step is followed by a classification into singular and multiple fiber populations by analyzing the number of local ODF maxima.
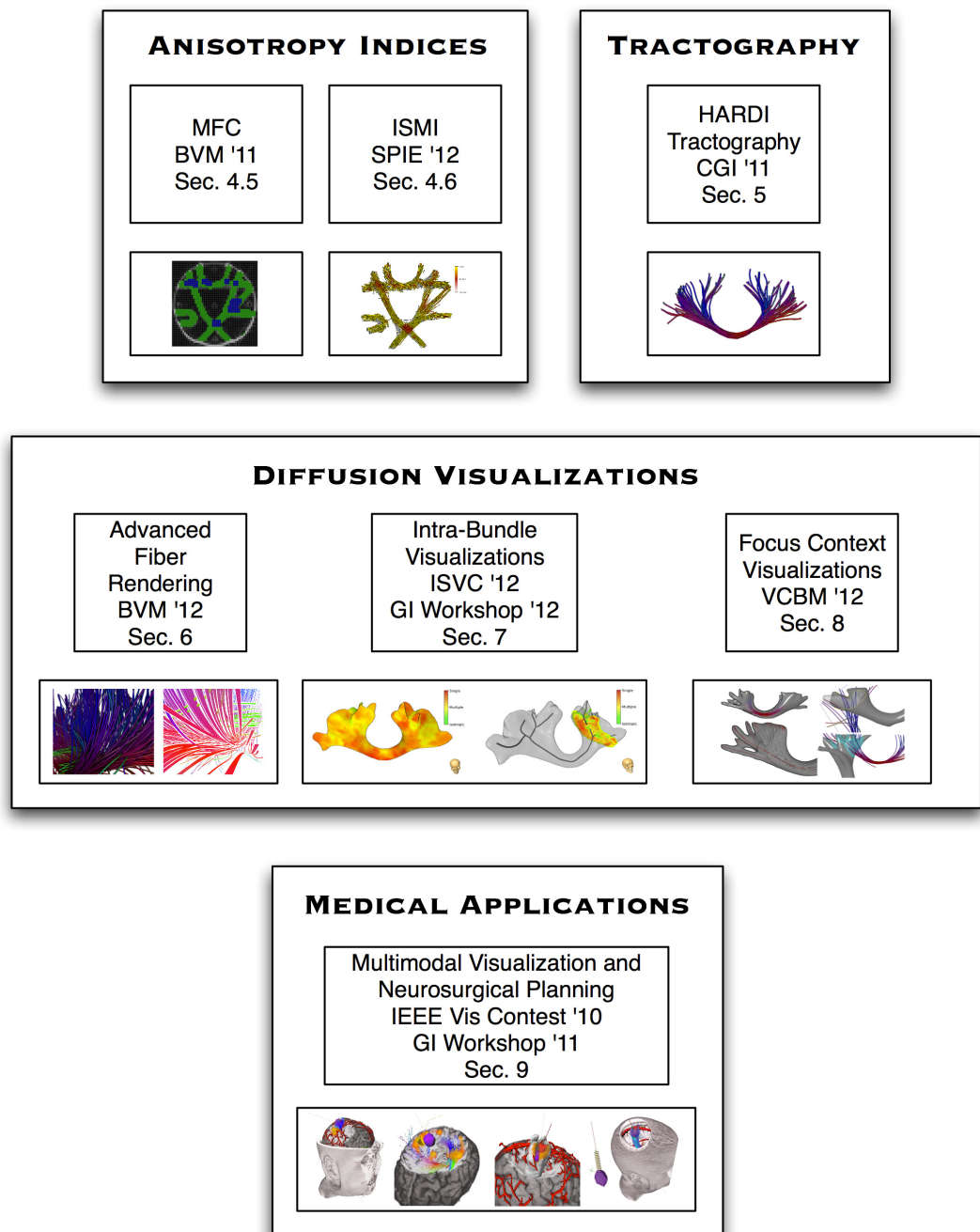
Figure 1.1: Overview of main contributions in the presented work. Emerging issues for diffusion data processing and visualizations are considered successively and are categorized in groups: The pipeline starts with extracting information about the local anisotropy (Anisotropy Indices) followed by white matter tract reconstruction (Tractography), visualizations (Diffusion Visualizations), and applications to neuroscience (Medical Applications). Subgroups are indicated by a box containing the name of the approach, the scientific publication, the section, and in addition display a representative picture of the approach.

Part III - Chapter 5 addresses the deterministic tractography approach for fiber reconstruction. HARDI provides more detailed information about local diffusion distributions within one voxel than DTI. As a result, streamline tractography algorithms dealing with multiple diffusion directions are required. However, defining the most adequate next step for propagation is challenging and requires advanced ODF analysis. The developed deterministic method includes an evaluation of initial tracking orientations using the seed point's ODF and distances to white matter boundaries computed from vectors orthogonal to the current orientation. Furthermore, several tracking characteristics, such as curvature thresholds, information about local fiber population and the position of the current tract within the bundle are used to determine the most adequate propagation direction from the ODF. The approach was evaluated using a phantom dataset and discussed with neurosurgeons considering challenging regions is the human brain.

Part IV - Chapters 6, 7, and 8 introduce innovative visualization approaches for diffusion MRI data, using the analysis methods explained in the previous parts. In terms of visualizing the reconstruction results, various challenges exist: First, contrary to DTI, HARDI tractography line representations comprise more complex configurations since various ODF directions are significant for independent line propagations. For this reason, visualizations suffer from visual clutter and weak spatial perception in complex regions. To address this problem, enhanced visualization approaches such as streamtube rendering, colormapping, ambient occlusion, and depth-dependent halos are introduced in Section 6. Second, the computation of fiber encompassing hulls is beneficial in cases where the extent or the shape of a bundle is crucial. For example in neurosurgical examinations to evaluate potential postoperative damages. However, fiber hulls provide no information about the inner-bundle diffusion characteristics obtained from diffusion classifiers. Therefore, an intra-bundle raycasting approach was developed which encodes information about the local intra-bundle fiber distributions on the hull surface. In addition, a centerline slicing approach was developed which reveals local diffusion information on a plane perpendicular to the bundle centerline. The resulting visualizations are enhanced with spatial depth encodings such as Phong illumination and ambi-

ent occlusion and were evaluated in the course of a user study. The approach as well as the results are discussed in Section 7. The third contribution in terms of white matter visualization combines line and bundle renderings within a focus and context approach and is called the *BundleExplorer* (Section 8). A conjunction of both visualization modalities was achieved using cutting techniques such as plane slicing and view-vector dependent rendering. Furthermore, inner-bundle fiber configurations, such as distance to the bundle hull and bundle intersections, are highlighted by visual enhancements.

Part V - Chapter 9 introduces medical applications for diffusion imaging. Contributions discuss novel visualization and interaction methods for neuro-surgical planning. In cases of deep-seated brain tumors, multiple datasets are acquired to provide information about the extent of the tumor and the spatial relation to risk structures such as vessels, activation areas or neuronal pathways. Therefore, multimodal volume rendering approaches were designed, fiber filtering methods developed, and visual enhancements realized in order to support the surgeon in diagnosis and preoperative planning. The multimodal visualization tool is discussed in Section 9.5. Section 9.6 introduces approaches for intuitive user interaction to define the access path and extends the previously presented preoperative planning tool. The identification of risk structures, such as neuronal pathways, activation areas or vessels is addressed as well as access path definition issues: Path positioning, visualization, and evaluation are enhanced by computer graphics techniques. The last step of the proposed surgical planning workflow forms a presurgical view which facilitates the spatial comprehension of the opening. Parts of the developed tool were submitted to the IEEE Visualization Contest 2010, where they were rated by neuroscientists as well as visualization experts. Results are given in the course of this section.

2 Neuroanatomy and neuroscientific questions

2.1 Overview

Understanding the anatomical connectivity of the brain has long been a subject of great interest in both fundamental neuroscience as well as neurosurgery and the study of neurological disorders. The development of diffusion imaging provides new opportunities in terms of white matter examination: Connectivity analysis between functional regions allows a step forward in understanding the organization and functioning of the brain. On the other side, the reconstruction of major white matter tracts facilitates insight into the severity of the neurosurgical case and potential postoperative damages. In addition, neurological and psychiatric disorders such as stroke, schizophrenia, and multiple sclerosis can be examined using information about tract integrity. However, in order to develop and evaluate contributions to diffusion image processing and visualization, it is crucial to understand the anatomy of the neuronal network as well as the impact of the MRI diffusion signal. Furthermore, HARDI models as well as the ODF, the spherical probability function, have to be examined in order to provide a benefit for diffusion visualization. Therefore, the history of neuroscience is introduced briefly in Section 2.2 as well as white matter microstructures in Section 2.3 and major white matter fiber bundles in Section 2.4. Neuroscientific questions, categorized in fundamental neuroscience (Section 2.5.1), neurological disorders (Section 2.5.2) and neurosurgical planning (Section 2.5.3) are also discussed. The literature on human anatomy, and neuroanatomy in particular, is extensive [7, 106]. Detailed information about white matter structures in the

brain is introduced for example by Mori et al. [69]. An introduction to diffusion imaging is published by Jones [45] and was presented by Hagmann et al. [37].

2.2 History of neuroscience

The human brain is by far the most complex and not yet fully understood system in the human body. In history of neuroscience Johann Christian Reil (1759-1813) and Karl Friedrich Burdach (1776 - 1847) stand out with their important findings. In 1809 Johann Christian Reil, Professor at the University of Halle, developed a brain preparation method: He suggested a soaking of the brain in alcohol. This procedure facilitates brain dissection and thereby reveals the course of major white matter fiber bundles [87]. Figure 2.1 shows an illustration of Reil's findings, published in *Archiv für die Physiologie* between 1809 and 1812. Later, his findings were confirmed by Karl Friedrich Burdach, Professor of anatomy, physiology, and forensic medicine at the University of Dorpat. His studies were combined in his publication *Vom Baue und Leben des Gehirns* [16]. However, Theodor Hermann Meynert (1833-1892) was the first who classified major white matter tracts. In addition, he suggested a novel theory of brain function: Information from multiple sources are required and integrated for every brain task. In [66] Meynert suggested the classification of neuronal fibers into *projection*, *commissural* and *association* fibers (Section 2.4). Based on this work, he subdivided and categorized neuronal pathways in more detail with a focus on association pathways, illustrated in Figure 2.2. In 1994 Peter J. Basser, James Mattiello and Denis LeBihan published their initial paper on MR diffusion tensor imaging [4]. This was the beginning of non-invasive examination of white matter architecture.

2.3 White matter microstructures

Neurons are cells, responsible for transporting information through the body using electrical signals. Neuronal cells are connected to form the *neuronal network* and belong to the *nervous system*. They consist of a *cell body*, *dendrites*, an *axon*,
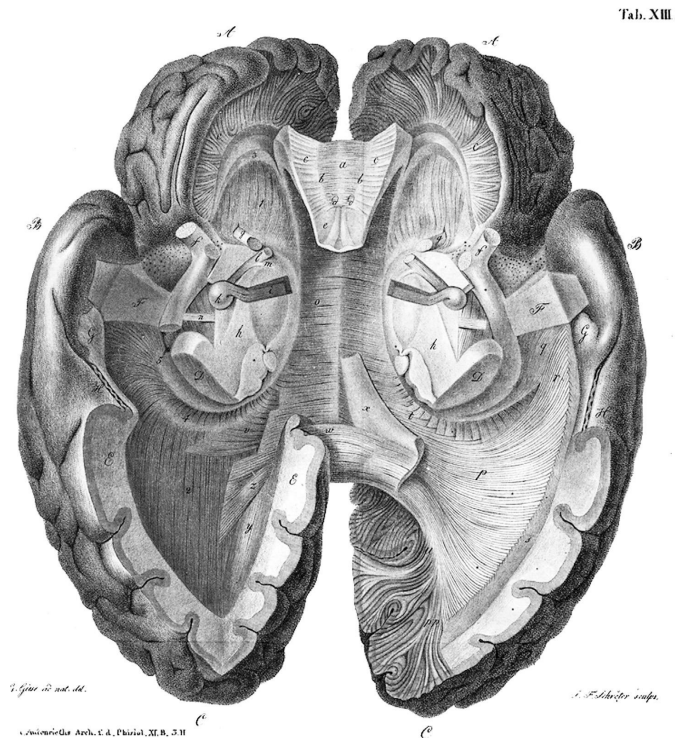
Figure 2.1: Illustration of commissural fibers by Johann Christian Reil [86], view from below.

and *axon terminals*, as displayed in Figure 2.3. Multiple dendrites branch from a cell body, however, only a single axon exists within a neuron. An axon is the extension of the cell body and ranges up to one meter in a human brain. It is surrounded by a *myelin sheath* which provides an insulating function and therefore, facilitates signal conduction. The combination of the axon and the myelin sheath forms the actual neuronal fiber. Neuronal signals are passed through the network along axons terminals, which form *synapses* with neighboring neurons. Signals are received through a neuron's dendrites, processed in the cell body, and transfered through the axon by so called *action potentials*. The cell body of a neuron lies in the gray matter of the brain, whereas the axon, wrapped in myelin, is found in the white matter. The actual signal processing is a gray matter task. Whereas information transfer, realized by axons, is performed in the white matter. Axons of white matter are well organized. In fact, the connectivity
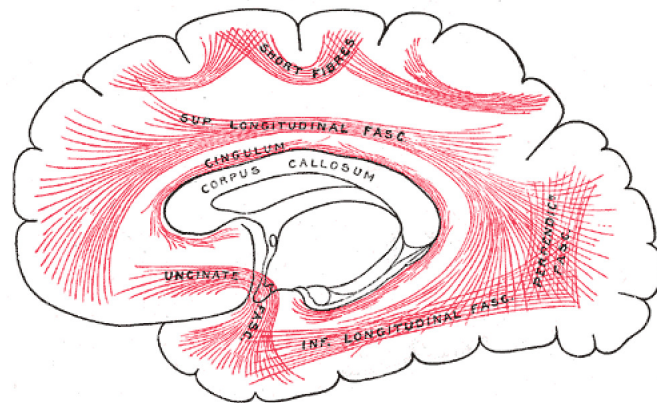
Figure 2.2: White matter fiber pathways: Illustration of principal association fibers in the human brain. Image adapted from Gray's Anatomy [36].
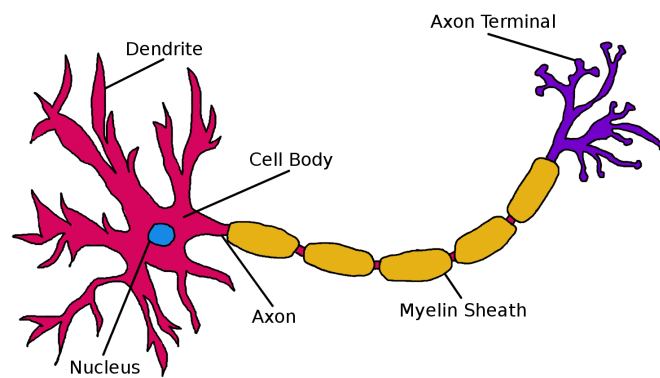
Figure 2.3: Schematic illustration of a neuronal cell: The neuron consists of a cell body, dendrites, an axon, and axon terminals.

of certain gray matter brain regions, realized by axonal pathways, is essential for neuronal connectivity. Therefore, the functioning of axonal conduction is crucial. Myelin acts as an insulator of axons and determines the propagation speed of nerve impulses. However, the integrity of myelin sheath is influenced by many factors such as brain development and neurological disorders and are discussed in Section 2.5.

2.4 Neuroanatomy

The brain consists of gray and white matter and weights about 1400 grams in adults. Brain gray matter includes the cortex: the approximately 3-mm-thick surface of the brain which contains the neuronal cell bodies. White matter however, consists of densely packed fibers, the axons. The *cerebrum* is the largest part of the brain and is divided into left and right hemispheres. It features a large amount of *gyri* and *sulci*, which extend the surface of the cortex. Each cerebral hemisphere is redivided into the *frontal lobe*, the *parietal lobe*, the *temporal lobe*, and the *occipital lobe*, as illustrated in Figure 2.4. The frontal lobe is responsible for tasks such as voluntary motor function, motivation, and aggression. Reception and the evaluation of sensory information, except for smell, hearing, and vision is the task of the parietal lobe. The frontal and parietal lobes are separated by the *central sulcus*, which is anteriorly framed by the *precentral gyrus* also known as the *primary motor cortex*, and posteriorly by the *postcentral gyrus*, which is the *primary somatic sensory cortex*. The occipital lobe handles visual input. The temporal lobe is dedicated to evaluating smell as well as hearing. Furthermore, it is essential in memory related tasks.

Neuronal pathways are categorized into the following three main compartments: *association fibers*, which connect certain areas of the cerebral cortex within the same hemisphere, *commissural fibers* also known as *commissures*, which connect one cerebral hemisphere with the other, and *projection fibers*, which connect parts of the spinal cord with the cerebrum. *Cranial nerves*, in contrast to spinal nerves, emerge directly from the brain. A cranial nerve has one or more of the following three functions: *sensory*, including senses such as vision, *somatic motor*
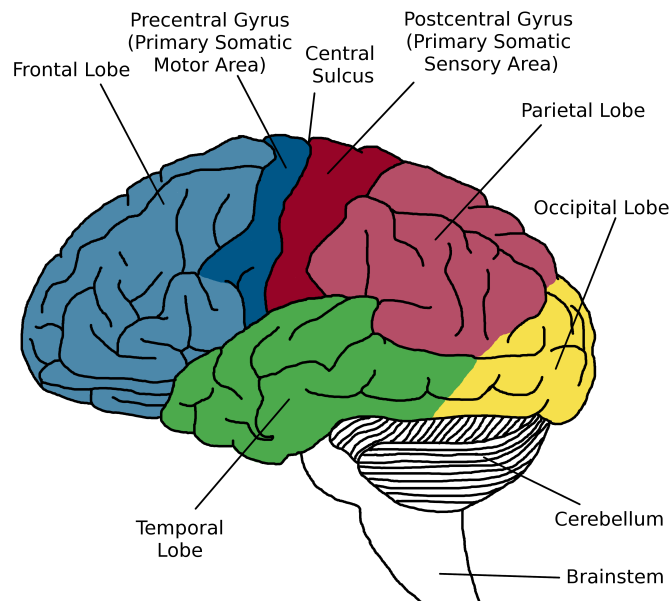
Figure 2.4: Illustration identifying gray matter areas of the brain surface: The frontal
           and parietal lobe are divided by the primary somatic sensory and primary
           somatic motor gyrus.

function or muscle control, and *parasympathetic*, which is dedicated to controlling smooth muscles such as cardiac muscles.

In the following, the major human pathways which are important throughout this thesis are named and their function briefly explained.

Corpus callosum

The *corpus callosum* (CC) is a major neuronal pathway, connecting the two cerebral hemispheres. It is the largest fiber bundle in the human brain and contains more than 300 million axons. Degeneration studies in monkeys showed that the entire cortex is connected by commissural fibers of the CC. Figure 2.5 shows the CC in a coronal and an axial cross-section. Since the CC is one of the most important as well as the largest neuronal fiber system, it has been a target of tractography approaches since the beginning of diffusion imaging. However, DTI-based fiber reconstruction often fails to make all of the connections due to its intrinsic assumption. In particular, commissural connections to lateral ar-

eas of both hemispheres are not detectable using DTI-based approaches. This is caused by the fact that the association fibers, the *superior longitudinal fasciculus* and projection fibers belonging to the *corticospinal tract*, run within the same region.

(a) (b)
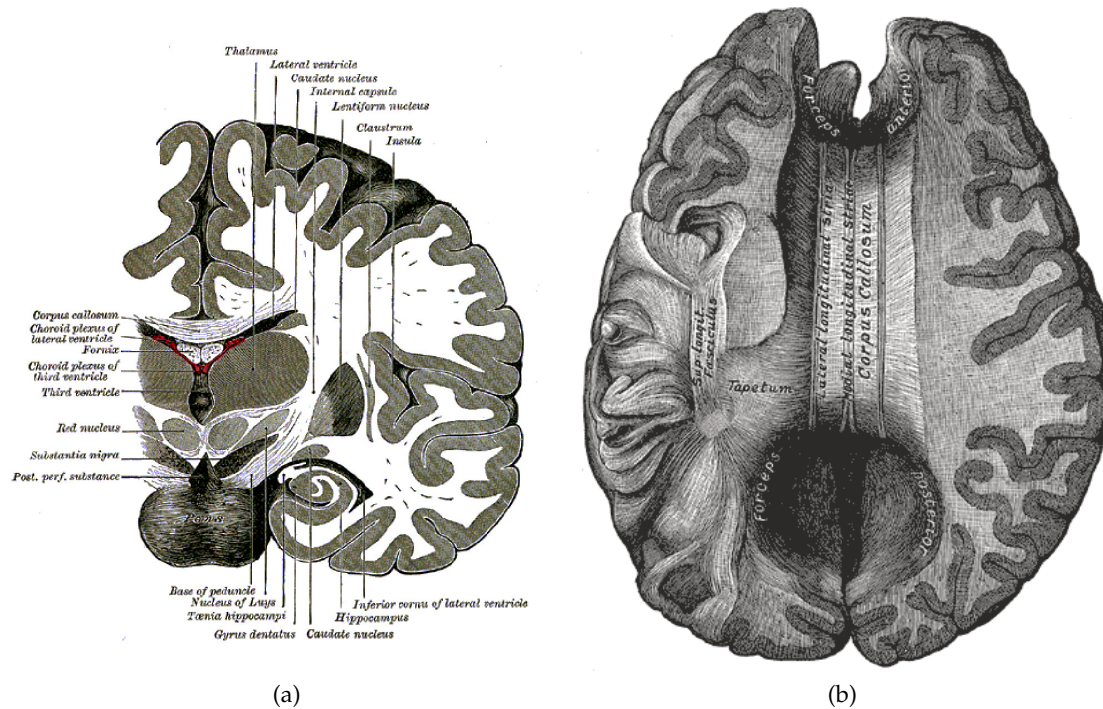
Figure 2.5: Schematic illustration of the *corpus callosum*: Callosal fibers displayed in coronal (2.5a) and axial (2.5b) cross-sections of the human brain. Image adapted from Gray's Anatomy [36].

Pyramidal system

The *pyramidal system* is a descending neuronal pathway and includes two fiber tracts: the *corticospinal tract* and the *corticobulbar tract*. The course of the *pyramidal system* in a coronal view is shown in Figure 2.6. The *corticospinal tract* (CST) is a motor pathway associated with cortical control of movements below the head, especially the hands. It originates in the cerebral cortex, more precisely in the primary motor and premotor areas of the frontal lobes and the somatic sensory

parts of the parietal lobes, and it terminates in the spinal cord. Damage of the
CST results in reduced muscle tone, clumsiness, and weakness but not complete
paralysis. The main function of the CST is to add speed and agility, especially
to the movement of the hands. However, spinal cord lesions affecting both the
indirect and the direct pathways results in complete paralysis. The *corticobulbar
tract (CBT)* is involved in direct control of head and neck movements. It origi-
nates in neighboring regions of the CST and follows the same route down to the
brainstem.
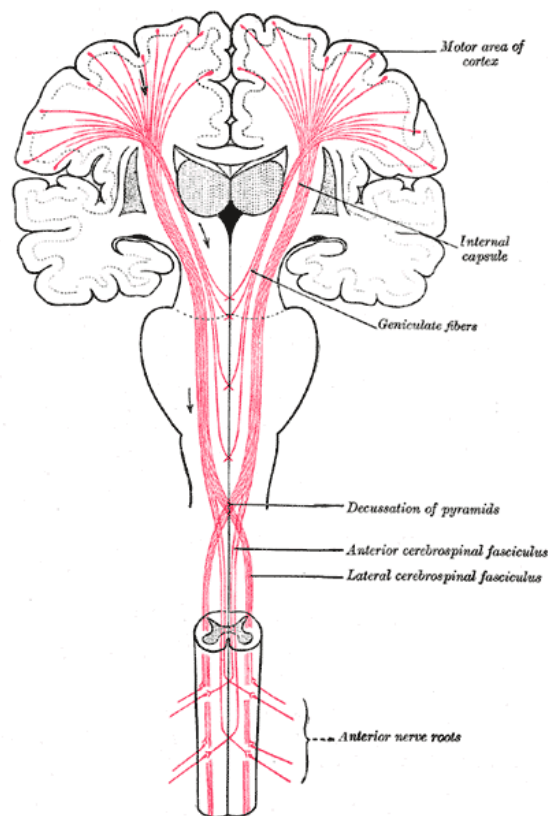
Figure 2.6: Schematic illustration of the *pyramidal system*: The white matter tract asso-
ciated with movement originates in the brainstem and fans into both hemi-
spheres. Image adapted from Gray's Anatomy [36].

Superior longitudinal fasciculus

The *superior longitudinal fasciculus* (SLF) belongs to the association pathways in the brain and forms a large arc, also known as the *arcuate fasciculus*. It branches in the frontal, parietal, occipital, and temporal lobes, as illustrated in Figure 2.2.

Centrum semiovale

The *centrum semiovale* is a white matter region in the human brain where the CC, the CST, and the SLF cross. Voxels belonging to this region comprise challenging diffusion profiles, potentially a two-fiber or three-fiber crossing distribution. The CC and the CST cause a fanning within one plane for single voxels. Furthermore, the SLF adds a crossing diffusion distribution to the probability function. In fact, these voxels cause the inability of DTI-based tractography approaches to reconstruct commissural fibers of the CC. Figure 2.7 shows a directional color coding of the region of the *centrum semiovale*.
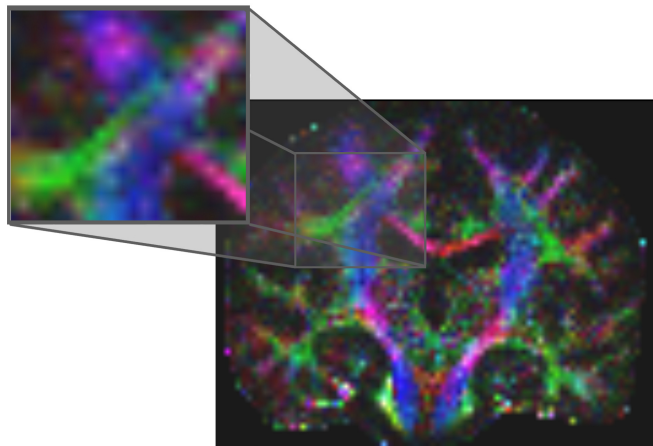
Figure 2.7: Directional color coded image with zoom of the *centrum semiovale*, coronal slice: Fibers belonging to the CST are shown in blue, fibers of the CC in red, and those belonging to the SLF in green.

2.5 Neuroscientific questions

As diffusion imaging emerged, the accompanying unique possibility of visualizing and analyzing fibrous structures lead to great attention in the field of neuroscience. Medical questions concerning either white matter tracts or muscles arose. In the course of the presented research on diffusion visualization, questions related to neuroscience as well as neurosurgery are addressed. Potential contributions of diffusion imaging, especially HARDI, to neuroscience were examined with neuroscientists as well as neurosurgeons. Neuroscientific questions were discussed with the department of neurosurgery at the *Universitätsklinikum Marburg* in Marburg, Germany and the department of neurosurgery at the *Stiftungsklinikum Mittelrhein* in Koblenz, Germany. In terms of fundamental neuroscience, approaches were examined with members of the Neuroscience Unit at the Institute of Biomedicine/Physiology, University of Helsinki in Helsinki, Finland. In order to connect the developed approaches to the elaborated medical questions, the main contributions of the thesis are subsequently linked to neuroscientific questions. In the following, tasks related to fundamental neuroscience (Section 2.5.1), neurological disorders (Section 2.5.2), and neurosurgical planning (Section 2.5.3) are introduced and potential contributions of diffusion imaging and visualization approaches discussed.

2.5.1 Fundamental neuroscience

Neurophysiology aims to understand the biological mechanism of the nervous system, which is in charge of collecting, distributing, and integrating information. Little is known about the complex white matter architecture in the human brain and the anatomical connectivity of certain functional regions of the brain. Diffusion imaging provides information about local molecular diffusion and forms the basis for tract reconstruction. DTI was the first technique that allowed the course and integrity of major fiber tracts to be determined. However, to make a true contribution to fundamental neuroscience, small pathways and more intricate axonal connections are of great interest to further understanding of how the brain functions. This is where HARDI offers a significant contribu-

tion by successfully capturing and modeling more detailed diffusion profiles. Furthermore, HARDI-based tractography approaches (Part III) provide a more precise approximation of fiber pathways. Fiber reconstructions emerging from defined cortical regions help neuroscientists to understand which brain regions are related to certain tasks and in addition, which cortical zones are involved. For example in transcranial magnetic stimulation (TMS) studies, cortical regions related to certain tasks are determined and used as a region of interest for tractography. TMS provides the unique possibility to achieve immediate feedback when blocking certain cortical areas by inducing electric current. As a result, brain regions, which are involved with certain tasks, are identified individually. More important, their impact on certain tasks is examined in the course of an TMS experiment. Figure 2.8 shows the setup of an TMS experiment.
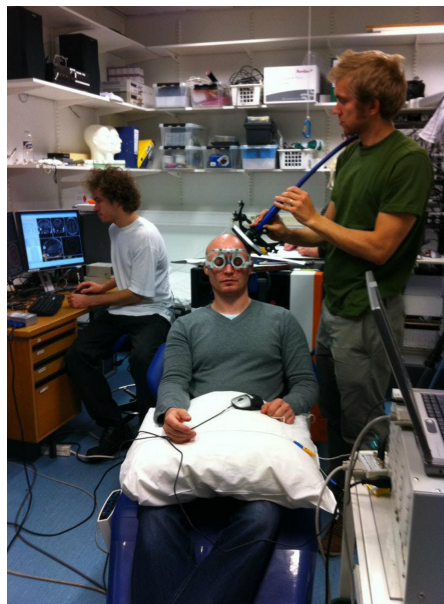
Figure 2.8: Setup of a TMS experiment related to the study; undertaken by Hannula et al. [40] at the BioMag Laboratory at Helsinki University Central Hospital using the Nextim [71] TMS navigation system: The subject sitting in the chair wears marker equipped glasses in order to localize the head and match it with preoperatively acquired data, such as DTI. Reflecting markers are added to the coil in order to localize it and perform blocking or stimulation with high precision.

In terms of understanding brain functioning, TMS offers a huge contribution: Task-related cortical zones are not only identified but also triggered by stimulation; as such, their impact is examined with immediate feedback. In the course of an TMS experiment, scientists examine the behavior of a subject performing a specific task while they blocked or stimulated involved cortical activation zones. The inclusion of a previously acquired diffusion dataset also facilitates task-related tractography by using a seed region for fiber reconstruction, which is defined by the TMS target region. Therefore, further white matter connections lead to secondary activation areas being additionally involved in the specific task. In a subsequent step these areas can be subject to TMS stimulation or blocking in order to examine their influence on the task. HARDI tractography approaches have further potential to enhance research in this field since hypothesis concerning task-involved cortical activation areas include small pathways. As a result of HARDI tract reconstruction, more intricate and small fiber configurations can be examined. A TMS study including DTI was performed by Hannula et al. [40]. The authors successfully reconstructed the connection between the *primary somatic sensory cortex* (S1) and the *middle frontal gyrus* (MFG). In addition they could corroborate their hypothesis that a single TMS pulse to the MFG plays an important role in tactile-related working memory performance.

Furthermore, a combination of diffusion imaging and functional magnetic resonance imaging (fMRI) is promising. fMRI reveals task-related activation zones by measuring the blood oxygenation level in the brain when performing a specific task such as finger tapping. A multimodal analysis approach, using acquired fMRI hot spots, directly relates white matter tracts as the anatomical connection of activation areas (Section 9.5). Therefore, both TMS- and fMRI-related tract reconstructions lead to anatomical as well as functional meaningful information about white matter connectivity which is beneficial in terms of fundamental neuroscience and neurosurgical planning.

It has been reported that the degree of diffusion anisotropy is related to age and gender. Myelinization is the process of myelin growing around axons, which acts as an insulating membrane that facilitates the conduction of nerve impulses. For this reason, myelinated fiber tracts comprise a higher anisotropy than non-myelinated ones. In fact, the degree of fiber-myelinization is related

to the maturity of the brain: Newborns show less myelin around fiber tracts. Consequently, brain development is examined using diffusion imaging and diffusion classifiers, showing the integrity of fiber pathways (Section 4.5 and 4.6). On the other hand, an age-related loss of regional white matter is reported. This anatomical change results in decreased anisotropic diffusion. Diffusion imaging provides quantitative data by analyzing the diffusion probability function using diffusion anisotropy classifiers. As a result, diffusion imaging is used to monitor both brain development and aging.

2.5.2 Neurological disorders

Since diffusion imaging measures the degree of free diffusion, quantitative analysis of regions is also feasible. Differences in white matter diffusion profiles indicate abnormalities in terms of tract location or integrity.

Multiple sclerosis (MS) is a chronic inflammatory demyelinating disease, featuring a relapsing-remitting course in which symptoms emerge and improve over a certain period. Studies have shown that MS not only causes demyelination but also axonal damage. This leads to a white matter directionality loss in the diffusion profile which is detected by diffusion imaging. Using tract reconstructions in combination with anisotropy classifiers (Section 7) or regional anisotropy examination (Section 4.5 and 4.6) is helpful in diagnosing, understanding, and monitoring MS.

In terms of neurodegenerative diseases such as *mild cognitive impairment* (MCI) or *Alzheimer's disease* (AD), diffusion imaging provides important information: Anisotropy classifiers, ODF-based fiber visualization (Section 6) or whole bundle visualization (Section 7) are beneficial in order to predict type, location, as well as timing of tissue degeneration. For example, MCI has been proven to be a precursor of AD; therefore an early diagnosis of MCI is vital in terms of identifying white matter degeneration and examining the development of AD. In addition, detailed diffusion analysis is beneficial in staging neurodegenerative diseases and monitoring the progress.

2.5.3 Neurosurgical planning

Brain lesions, such as tumors, are one of the most common abnormalities in the brain. Essential brain properties such as functional zones located on the cortex and white matter tracts connecting these are considered as risk structures in surgical interventions. In fact, damage to both activation zones as well as neuronal fibers, can lead to severe postoperative impairment. Therefore, the aim in neurosurgical planning is the minimization of postoperative damages. Nowadays, neurosurgery is feasible for deep-seated lesions or even lesions located close to essential white matter tracts. This is due to sophisticated MRI technology such as fMRI and diffusion imaging. Preoperatively, essential information about the spatial relationship between the lesion and vital brain structures is obtained through imaging and visualization. Challenging neurosurgery is preceded by a planning phase in which multiple volumes are combined (Section 9.5) and risk structures as well as safest access paths are defined (Section 9.6).

One of the leading clinical questions in terms of neurosurgical planning and pathology examination is whether a white matter tract is displaced or infiltrated by a lesion. Combining diffusion classifiers and tractography approaches within one visual representation (Section 6 and Section 7) provides vital information for answering this question. Fiber characteristics such as integrity information are directly visualized on the bundle hull and are thereby combined with information about the spatial position of the lesion.

3 Diffusion imaging

3.1 Overview

Diffusion imaging is able to characterize organized tissue due to the fact that the movement of water molecules in fibrous material largely occurs with the fiber course. It poses a large achievement in neuroscience since it captures information about the organization of neuronal pathways in vivo. Applications include fundamental neuroscience and neurosurgical planning. Diffusion imaging models the probability density function that describes the diffusion of water molecules in one voxel. Diffusion tensor imaging is a technique that fits the acquired signal into a second order tensor. This model uses a minimum of six gradient directions and assumes a Gaussian diffusion process. However, because of the model assumption of DTI, only one diffusion direction can be represented. To overcome this limitation, more sophisticated models were introduced and called high angular resolution diffusion imaging (HARDI). Here, advanced imaging and reconstruction techniques are applied in order to model the underlying diffusion profile properly.

The previous chapter comprises a brief introduction to human brain white matter structures as well as contributions of diffusion imaging to neuroscience and neurosurgical planning. However, principals of molecular diffusion, MRI and HARDI techniques are crucial to understanding, designing, and evaluating reconstruction and visualization methods for medical purposes. For this reason, this chapter is dedicated to providing the necessary background information for diffusion imaging. Fundamentals in terms of molecular diffusion as well as reconstruction techniques that transforms the acquired signal into a meaningful representation are introduced. Subsequently, the constitution of diffusion datasets is presented. This chapter starts with an introduction into the

physics of diffusion (Section 3.2) followed by an existing diffusion profile description (Section 3.3) and an illustration of diffusion in the human brain (Section 3.4). Subsequently, the concept of diffusion magnetic resonance imaging is introduced (Section 3.5), including the basics of magnetic resonance imaging (Section 3.5.1), the extension of MRI to acquire diffusion information (Section 3.5.2), as well as the reconstruction methods diffusion weighted imaging (Section 3.5.3) and diffusion tensor imaging (Section 3.5.4). The challenge of acquiring, modeling, and visualizing complex diffusion profiles such as fiber crossings is an important subject within this thesis and therefore subsequently discussed in greater detail (Section 3.6). First, an introduction to challenging white matter configurations is provided (Section 3.6.1). Second, a review as well as an evaluation of state of the art HARDI reconstruction methods is presented in order to motivate the decision for the applied reconstruction method within this thesis (Section 3.6.2). Furthermore, since the acquisition of HARDI datasets requires an intense study of MRI parameters and because an adequate dataset is always influenced by many competing factors, an introduction to acquisition aspects of HARDI is also provided (Section 3.6.3). The chapter closes with the presentation of the utilized diffusion datasets (Section 3.7).

3.2 Physics of diffusion

Einstein was the first who formally described molecular diffusion [27], which is also referred to simply as diffusion or Brownian motion. In 1827, the botanist Robert Brown discovered the jostling of pollen grains under the microscope. Einstein later explained that the pollen grains were subject to the thermal movement of the surrounding water molecules. Hence, the jostling indirectly exhibited the movement of water molecules: the process of diffusion. Generally speaking, molecular diffusion is the displacement of any type of molecule in fluid agitated by thermal energy. The displacement occurs randomly since molecules constantly collide with one another. Figure 3.1 illustrates a so called random walk of a single molecule. Molecular movement is best described by a
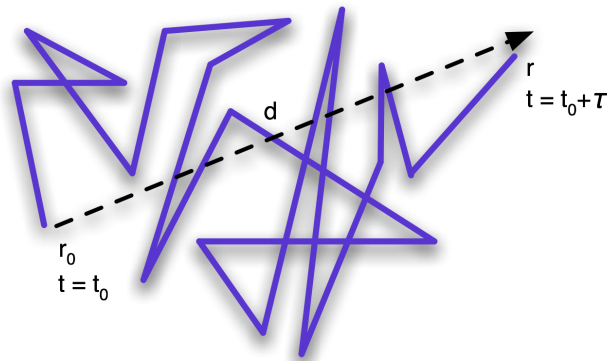
Figure 3.1: Brownian motion: Thermal energy causes molecular movement, which leads to constant collision and a random walk. The displacement observation starts at position $\mathbf{r}_0$ and time t_0 and ends at position $\mathbf{r}$ after time interval τ. The arrow illustrates the displacement vector $\mathbf{d}$.

displacement probability density function which indicates how likely a molecule will travel in a certain direction with a certain distance.

To demonstrate the concept of diffusion, let us schematically analyze the displacement of N water molecules. First, one records a molecule's position at time $t = t_0$, which is referred to as $\mathbf{r}_0$. The effective diffusion time is indicated by $\tau = \Delta - \delta/3$ and represents the time when the gradients are active. After gradient activation, the current point in time is $t = t_0 + \tau$ and the molecule's position is indicated by $\mathbf{r}$. Figure 3.1 illustrates the random walk of a molecule. For each displacement vector $\mathbf{d} = \mathbf{r} - \mathbf{r}_0$ one now computes the amount of water molecules, n, which traveled the distance $|\mathbf{d}|$, during the time interval τ. In the following, τ will be referred to simply as the diffusion time. Most of the water molecules pass short distances, while others travel long distances. Figure 3.2 shows the histogram of the described diffusion process for a displacement vector $\mathbf{d}$, the associated displacement distribution $P(\mathbf{d}, t)$.

According to Einstein [27] the process of diffusion can be mathematically formulated: Diffusion is characterized by the mean-squared displacement that molecules travel for a certain time interval (m^2/s), leading to
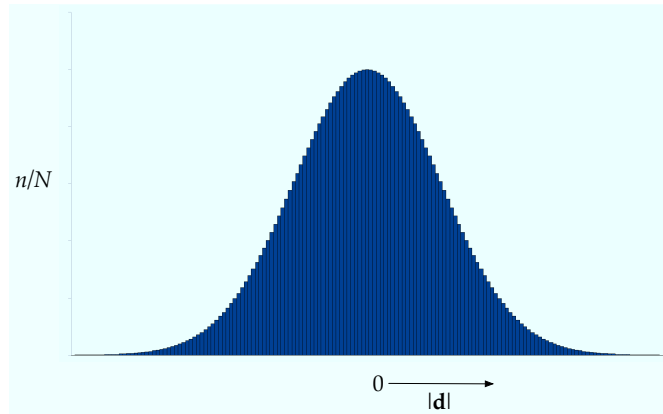
Figure 3.2: Diffusion probability displacement distribution: The histogram presents the diffusion of water molecules for a specific distance $|\mathbf{d}|$ (x-axis), defined by the displacement vector $\mathbf{d}$ during diffusion time τ. The y-axis shows the probability for each distance based on the proportion of molecules traveled that far during the diffusion time.

$$< \mathbf{r}, \mathbf{r}_0 >= 6D\tau, \tag{3.1}$$

in 3D. D is referred to as the diffusion coefficient, the viscosity of the medium and $<>$ denotes the ensemble average which is the average mean-squared diffusion distance along the direction $\mathbf{d}$.

3.3 Diffusion profiles

In order to understand the directionality of diffusion, imagine a drop of ink in a glass of water; water is a free diffusion medium. If there is no flow, the center of the ink does not move and the shape of the ink eventually becomes a sphere. In this case, only the diffusion coefficient D, which is the magnitude of the movement, is sufficient to describe the diffusion. The diffusion coefficient is related to the diameter of the sphere: The faster the diffusion, the larger the diameter of the sphere. Now, imagine a piece of paper, woven with dense vertical fibers and sparse horizontal fiber. If a drop of ink fell on that paper, the ink-pattern would
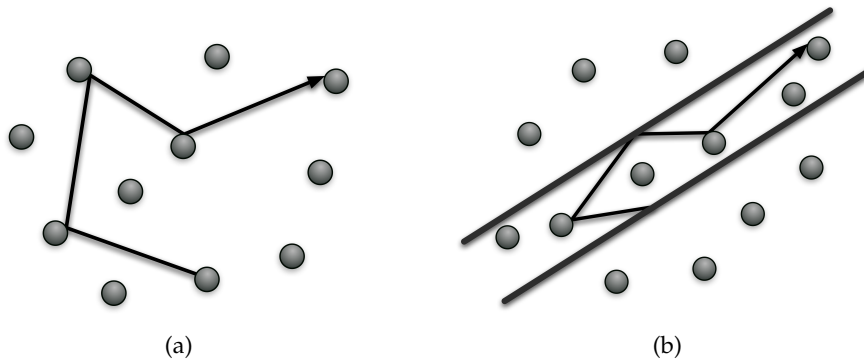
Figure 3.3: Simple diffusion profiles: Diffusion is either free (3.3a) or restricted (3.3b).

occur in a larger scale vertically than horizontally. In this case, the process of diffusion is directional and characterized by an orientation and a strength.

Water molecules moving into any direction in space in equal measure are referred to as isotropic diffusion, whereas a displacement which is aligned with a certain axis is called anisotropic diffusion. Free diffusion occurs isotropically, as depicted in Figure 3.3a. A restricted diffusion, as described in the second example, is present if the molecular movement is hindered by certain barriers, as shown in Figure 3.3b.

To demonstrate the concept of diffusion barriers and restrictions in more detail, one can think of a second illustration: Imagine a glass filled with water. Molecular diffusion itself is free and isotropic, hence water molecules move randomly within the glass. For this reason, the barrier for molecular movement is the boundary of the water glass. If one inserts water filled impermeable spheres into the glass, the water molecules within the spheres move randomly and isotropically within their boundary and the molecules outside move around the spheres. If one inserts water-filled cylinders, the molecular movement is restricted as before. However, the shape of the barrier facilitates a larger diffusion displacement in the direction of its extent rather than perpendicularly. Hence, the overall diffusion within the cylinder is anisotropic. Each of the presented cases leads to a different diffusion profile, which are illustrated in Figure 3.4. The first case features free diffusion with a large diffusion magnitude,
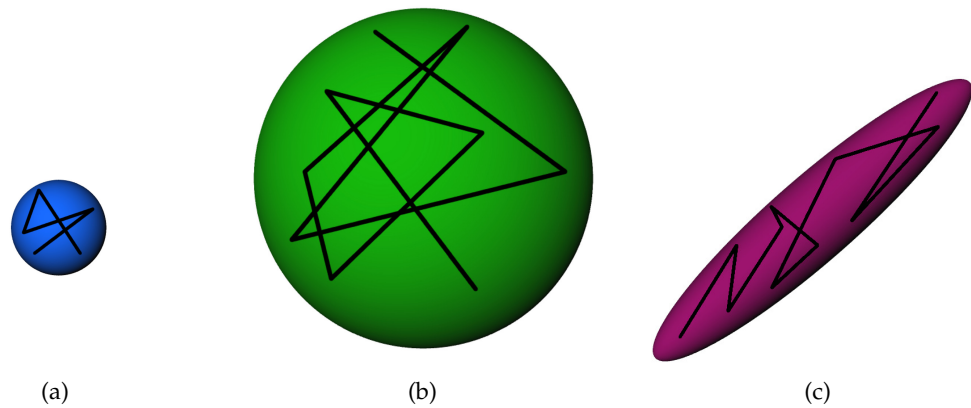
Figure 3.4: DTI diffusion profiles: Isotropic diffusion with a low diffusion magnitude (3.4a) and isotropic diffusion with a high magnitude (3.4b). Both profiles show no directionality; however, they differ in the distance the water molecules travel. Contrarily, anisotropic diffusion favors a specific direction (3.4c).

whereas the second case, including the water filled spheres, shows free diffusion as well, but a smaller displacement distance. The diffusion is restricted for the water filled cylinders since the molecular movement is defined by the anisotropic shape of the object.

3.4 Diffusion in the human brain

Previously, diffusion was explained as the thermally induced random movement of molecules which is categorized as either isotropic or anisotropic. Based on this, in the following, diffusion profiles of neuronal microstructures are discussed and the question of how fibrous tissue can be identified by diffusion imaging answered.

Human brain white matter consists of neuronal pathways which feature a fibrillar structure. They are organized as bundles consisting of coherently aligned axons surrounded by myelin sheaths (Section 2.3). Recall the free and restricted diffusion profiles introduced in Section 3.2: Molecular movement with approximately the same magnitude in all spatial directions is classified as isotropic

diffusion; whereas restricted movement, favoring one direction, as anisotropic diffusion. In the case of neuronal pathways, water molecular movement is restricted by barriers and as a result directed. In fact, to this day it is not clearly defined which kind of microstructure, within an axon, plays the important role in causing anisotropy. It was long time thought that the degree of myelinization, which influences the integrity of the insulating sheath around the axons, was the leading designator. However, current research considers intact axonal cell membranes as the primary cause for directional molecular movement. Nevertheless, myelin is still an important factor in terms of determining the directionality of diffusion, even though it only further modulates anisotropy. Certainly in either case, water molecules travel to a greater extent in the direction of the fiber course rather than perpendicular to it. For this reason, local diffusion is oriented along the course of an axon; subsequently, the measured degree of directionality, magnitude, and direction is considered as an indicator of microstructures as well as integrity.

3.5 Principles of diffusion magnetic resonance imaging

Earlier in this chapter it was mentioned that Einstein formulated molecular diffusion after Brown discovered the motion of pollen grains, which were indirectly affected by the thermal movement of water molecules. In the following, the relation of molecular diffusion in brain white matter and the course of neuronal fibers was discussed. However, one issue remains: How can the diffusion of water molecules in the brain be measured in order to obtain a diffusion distribution and thereby infer the neuronal network? How can diffusion be linked to an imaging signal? This chapter aims at providing basic knowledge to answer these questions.

The fundamental technique for measuring diffusion is magnetic resonance imaging which is extended by an advanced gradient scheme to record molecular movement. In order to provide a fundamental understanding of diffusion imaging, this section begins with an introduction to MRI (Section 3.5.1). In the following, acquisition aspects for measuring molecular diffusion, and thereby

extending conventional MRI, are introduced (Section 3.5.2). In terms of modeling the signal, the first method that emerged was diffusion weighted imaging (Section 3.5.3). However, this technique is unable to provide information about the diffusion direction as it only indicates the diffusion magnitude. For this reason, diffusion tensor imaging (Section 3.5.4) was developed.

3.5.1 Magnetic resonance imaging

Magnetic resonance imaging (MRI) signals originate from protons located in the nucleus of the hydrogen atom. In particular, the characteristic radio waves which are emitted by protons within a magnetic field are measured. Protons comprise a rotation which is commonly known as the spin. In quantum mechanics, the spin is considered to be a type of angular momentum which creates an individual, randomly oriented magnetic field for each proton. Since proton orientation is distributed randomly, tissue does not have a net dipole. However, within an external magnetic field $\vec{\mathbf{B}}$, the principal axes of protons become aligned with the vertical magnetic field and create a net magnetic field. After applying a second magnetic field horizontally, formed by a radio frequency pulse, the protons begin to precess about their vertical axes with an angular frequency called the Larmor frequency ω, as illustrated in Figure 3.5. With a given gyromagnetic ratio γ, the Larmor frequency is dependent on the magnitude of the applied magnetic field,

$$\omega = -\gamma\vec{\mathbf{B}}. \tag{3.2}$$

Proton precession creates a magnetic field which changes over time and emits an electric current. In fact, the electric current which is sent out by the precessing protons is the signal measured by MRI. The resulting net magnetic field features a horizontal and a vertical component. Changes in these two components are measured as protons respond to magnetic fields and radio frequency pulses. After turning off the horizontal radio frequency pulse, protons realign with the original magnetic field and fall out of synchronicity with each other: they dephase. This dephasing, also known as relaxation, leads to a loss in horizontal magnetization and a weakened signal in the horizontal component. The
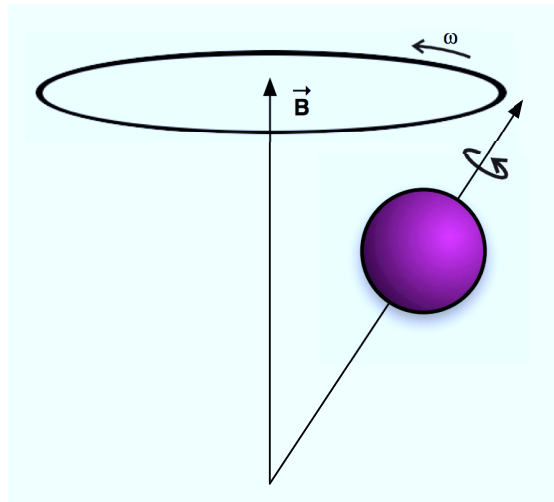
Figure 3.5: Spin of a proton: Illustration of a proton precessing about the magnetic field with Larmor frequency.

measured time constant is called T_2 and describes the falling out of synchronicity of the precessing protons.

On the other hand, the time the protons take to realign with the initial vertical magnetic field is encoded in T_1-weighted MRI scans. Protons have different time constants in which they align with the original magnetic field. This depends on several factors, such as whether they are embedded in fat or white matter. After introducing the actual causes of the MRI signal, the final aspect for consideration is the location of the signal in 3D. This aspect is crucial since it facilitates the acquisition of a volume dataset and the subsequent assignment of the scan to a distinct anatomical region. This is accomplished by using magnetic gradients which generate orthogonally oriented magnetic fields. These gradients are superimposed onto the initial magnetic field $\vec{B}$. The strength of each applied field changes gradually with respect to its axis. As a result, the Larmor frequency of a proton is altered according to its position along the applied axis. Therefore, a precise spatial encoding of the MRI signal, which is sent out from a proton within one volume element (voxel), is achieved. For complete 3D encoding, the first gradient is used to select a single slice. The following two

gradients further subdivide the slice in columns and rows. A Fourier transform is then applied in order to assign the acquired signal to a voxel.

3.5.2 Diffusion magnetic resonance imaging

The aim in diffusion imaging is to define the probability distribution function, which evaluates the likelihood that water molecules displace over a certain distance within a certain time. To extract the displacement probability of molecules, diffusion must be linked to the MRI signal intensity, which was described in the previous subsection. Three major achievements have to be named which were crucial in enabling a characterization of molecular diffusion using magnetic resonance imaging. These findings include the work of Hahn [38] and Torrey [112] as well as that of Stejskal and Tanner [109].

In 1950, Hahn discovered that a signal decrease occurs in a heterogeneous, magnetic field due to the motion of spins. However, it was Torry, who formally described the magnetization of spins in 1956. These findings form the basis for diffusion imaging. Later, in 1965, Stejskal and Tanner performed the first Pulsed Gradient Spin-Echo (PGSE) sequence to measure diffusion. They demonstrated the relation of the magnitude of a spin echo signal in a PGSE sequence to the displacement PDF of spins using a Fourier transform. The PGSE technique uses the observation that protons moving in the direction of the magnetic field gradient are effected by the magnetic field strength. However, this influence depends on their position along the gradient vector. In fact, further applied magnetic field gradients alter the phase of the precessing protons with respect to the magnetic field strength. Implementing this fact in order to monitor molecular movement results in the addition of two magnetic field gradients to those already applied in MRI in order to encode the position within a slice. Gradient pulses (GD) comprise a certain duration δ, indicating how long the GD is, and a separation Δ, which is the time between two gradients applied. Figure 3.6 schematically shows instances of a PGSE sequence, including the signal read out which is the spin echo (SE). The resulting phase shift of the proton spins, caused by the gradients, is proportional to their displacement over time. More precisely, the first gradient pulse aims to label the water molecules: It causes a phase shift
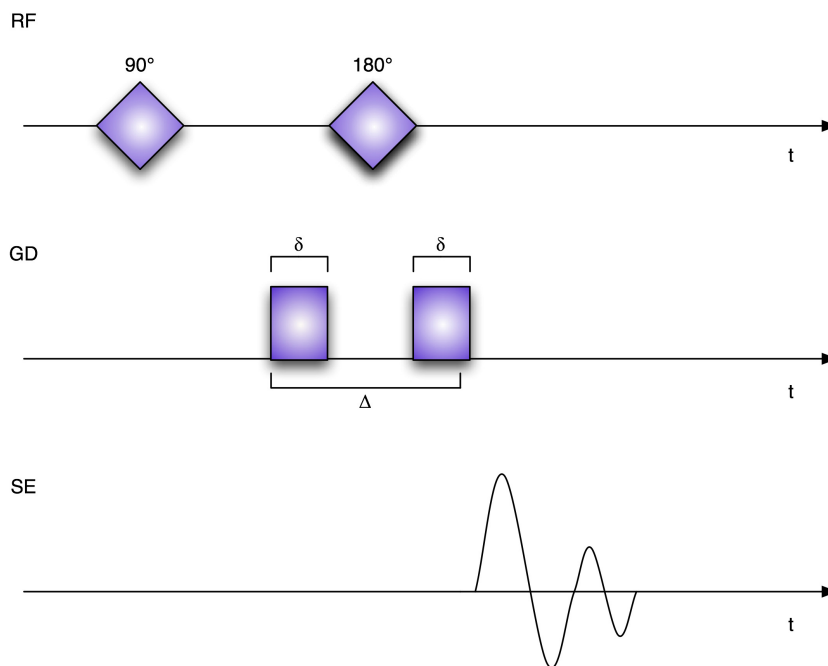
Figure 3.6: PGSE experiment to measure molecular diffusion distributions: Schematic illustration of an MRI Stejskal-Tanner sequence over time for a single diffusion direction of interest. Two diffusion gradient pulses are added to conventional MRI with a gradient pulse duration and a diffusion time interval, resulting in a spin echo.

depending on the strength of the gradient at the molecule's position for the time $t = 0$. Afterwards, a $180°$ radiofrequency pulse (RF) is applied to reverse the phase shift of the spins. The second gradient pulse exhibits the molecular displacement caused by diffusion for the time interval Δ. In fact, all spins remaining at the same position with respect to the gradient vector, return to their initial orientation. Those have traveled along the gradient vector are now subject to a different field strength and do not align with their initial orientation but undergo a further phase shift. The additional phase shift decreases the signal intensity for the voxel under consideration. As a result, voxels with underlying anisotropic diffusion, and which hence comprise large molecular movement, result in a lower diffusion signal. The lower signal results from the fact, that

less spins are aligned in voxels with large molecular movement. This is because underlying spins comprise different phases since they are affected by different magnetic field strengths. Caused by the random orientation of the spins, the overall magnetism within a voxel is reduced. For each applied magnetic field gradient direction, the signal intensity reveals the molecular displacement for a given direction of interest.

Summarizing, for each diffusion direction of interest, two gradient pulses are needed to determine the amount of water molecules which traveled in the specific direction. The output for each PGSE sequence is a scalar value for each voxel. And evident diffusion imaging comprises a longer acquisition time than conventional MRI as a result of the enhanced MRI acquisition. Additionally, the setup of a PGSE sequence, as illustrated in Figure 3.6, shows that enhancing the gradient duration time in order to enhance the diffusion signal, results in a longer acquisition time.

3.5.3 Diffusion weighted imaging

The most simple and earliest approach to measuring the diffusion of molecules in tissue is diffusion weighted imaging (DWI). In fact, DWI is the application of a single PGSE sequence and as follows, uses only one gradient direction. A DWI sequence results in one scalar value for each voxel. This scalar describes the probability that water molecules displace in the direction of interest, which is the gradient.

The attenuated signal, resulting from the PGSE sequence S, is related to the signal in absence of diffusion gradients S_0, which is called the baseline or b_0 image. The b-value is a scalar, representing the diffusion weighting applied in the acquisition. For this reason, a sequence without any diffusion gradient applied has a b-value of 0. This leads to the well-known Stejskal-Tanner equation for diffusion imaging:

$$\frac{S}{S_0} = exp\left(-\gamma^2\delta^2|\mathbf{q}|^2\left(\Delta - \frac{\delta}{3}\right)D\right),\tag{3.3}$$

where $|\mathbf{q}|$ is the gradient strength.

DWI does not include any postprocessing and as a result, bright regions in the resulting images reflect low directional movement. As explained previously, the resulting diffusion signal is high if many spins align, which is the case if less molecules displace. However, the estimation of molecular movement using DWI is apparently not sufficient since only one potential direction is considered and examined which results in two disadvantages: First, a low DWI signal only exhibits that molecules do not displace in the applied direction due to microstructural barriers. However, it is not identified if the diffusion pattern is isotropic or anisotropic. Second, the 3D displacement direction of the whole diffusion process within one voxel is still unknown. For this reason, DWI is only applicable in terms of a rough determination of the degree of anisotropy within a voxel. Applications of DWI include stroke: Diagnosing stroke as well as staging the severity requires a fast acquisition, which is possible using DWI since two additional MRI gradients are sufficient. Affected brain regions feature a local swelling which reduces the overall anisotropy. DWI characterizes restricted diffusion and performs a contribution in defining affected brain regions.

Later, apparent diffusion coefficient (ADC) imaging was introduced by Moseley et al. [70] as an advanced DWI technique. The measured diffusion signal is called apparent since no pure water is under consideration and not the true diffusion coefficient determined. ADC is related to a specific *b*-value and gradient direction:

$$ADC = -b \cdot ln\left(\frac{DWI}{b_0}\right), \tag{3.4}$$

where DWI is the resulting signal of a diffusion weighted sequence for a certain gradient direction. The necessary diffusion weighted gradient can be applied with any arbitrary angle. The authors acquired multiple DWI sequences and assumed a Gaussian diffusion distribution, which reformulates equation 3.3 and results in

$$S = S_0 \, exp\left(-b \cdot ADC\right), \tag{3.5}$$

with $b = \gamma^2 \delta^2 |\mathbf{q}|^2 \left(\Delta - \frac{\delta}{3}\right)$ is the *b*-value, the diffusion weighting factor which is proportional to the gradient strength and the diffusion time. Moseley et al. proposed to measure the ADC using two PGSE sequences with orthogonal gra-

dients and suggested taking the relation ADC_1/ADC_2 as the anisotropy indicator. However, the output signal was still strongly dependent on the chosen gradient direction. Still, the diffusion probability is only obtained in predefined directions. When performing three orthogonal measurements, the output is the trace of a diffusion tensor. As a result, the idea of directly estimating the displacement of water molecules in 3D emerged, which is the topic of the following sections.

3.5.4 Diffusion tensor imaging

As introduced in the previous section, ADC imaging utilizes PGSE sequences in order to measure the degree of directional diffusion for a specific magnetic gradient within one voxel. However, gradients were only applied sparsely and no rotational invariant model to represent the overall diffusion distribution within a voxel was present in the introduced scheme. For this reason, diffusion tensor imaging (DTI) emerged as a novel modeling technique. DTI characterizes
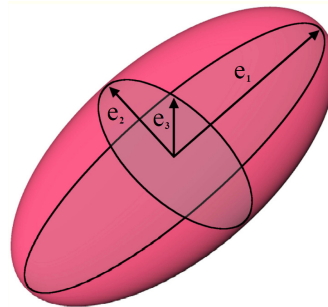
Figure 3.7: Diffusion ellipsoid: The shape of the diffusion ellipsoid is defined by the eigenvalues and eigenvectors of the **D**.

the diffusion signal by focusing on the directionality of diffusion. Contrary to DWI, DTI models directional diffusion profiles by means of a diffusion ellipsoid. The diffusion ellipsoid ca be designated using the scatter pattern produced by molecules which start from the same point but then displace. The shape in which the molecules position themselves after a certain period of time describes the final diffusion ellipsoid.

The diffusion MRI signal is measured along various gradient directions from which the shape and orientation of the ellipsoid is determined. The ellipsoid is computed to best fit the average diffusion distribution within each voxel. In order to describe the diffusion ellipsoid, three perpendicular principle axes and their lengths are needed. Unit vectors defining the orientation of the principal axes, the eigenvectors, are denoted by e_1, e_2 and e_3 and the lengths, corresponding eigenvalues, λ_1, λ_2 and λ_3. Eigenvectors determine the orientation and eigenvalues the shape of the diffusion ellipsoid. In fact, the direction of the eigenvector with the corresponding largest eigenvalue describes the orientation of the main diffusion. A visualization of the diffusion ellipsoid is presented in Figure 3.7.

Reformulating equation 3.5, results in the diffusion tensor $\mathbf{D}$ formulation,

$$S = S_0 \, exp\left(-b \, \mathbf{q}^T \mathbf{D} \mathbf{q}\right). \tag{3.6}$$

The ADC is defined as $\mathbf{q}^T \mathbf{D} \mathbf{q}$. In this reformulation gradient directions are includes as well: The scalar diffusion coefficient D of equation 3.3 is replaced by $\mathbf{D}$. $\mathbf{D}$ is a symmetric 3×3 matrix and characterizes the diffusion ellipsoid through its eigenvectors and corresponding eigenvalues,

$$\begin{bmatrix} D_{xx} & D_{xy} & D_{xz} \\ D_{yx} & D_{yy} & D_{yz} \\ D_{zx} & D_{zy} & D_{zz} \end{bmatrix}. \tag{3.7}$$

In fact, one can measure the ADC for any direction in space. However, since one cannot measure the eigenvectors and eigenvalues of $\mathbf{D}$ directly, one has to measure the diffusion along various orientations and estimate the diffusion ellipsoid. Using a tensor as a model is straightforward since it directly relates the measured signal to the elements in the 3×3 matrix. For example, the ADC_x measured along the x-axis is represented by the tensor value D_{xx}, the ADC_y by D_{yy} and ADC_z by D_{zz}. Thereby, the diagonal elements of the tensor are determined directly. To fill all values of the diffusion tensor one has to measure at least six independent diffusion axes. As a result, equation 3.6 has to be solved

at least six times for each voxel, excluding the b_0-image. For various gradient directions, the actual fitting process is realized by tensor diagonalization.

Using a diffusion tensor for anisotropy modeling, the resulting shape implies a 3D Gaussian diffusion process. Possible diffusion profiles for DTI are shown in Figure 3.8.
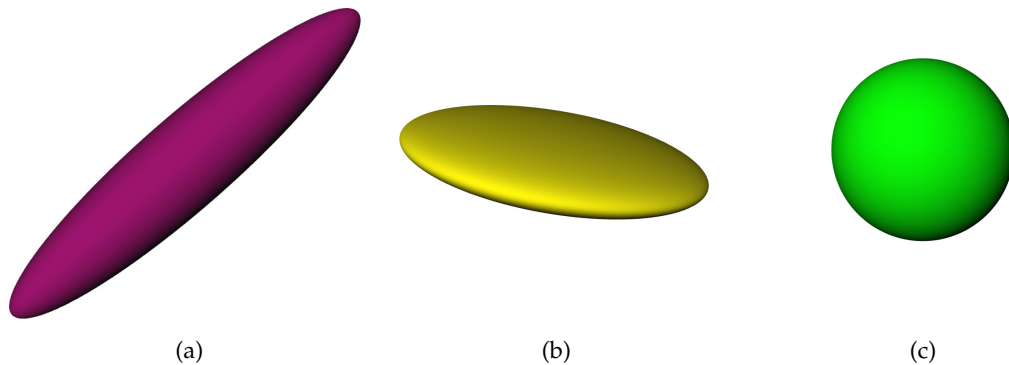
Figure 3.8: Potential diffusion profiles for DTI: Linear diffusion, with $\lambda_1 \gg \lambda_2 \geq \lambda_3$, favoring one orientation (3.8a); planar diffusion, with $\lambda_1 \simeq \lambda_2 \gg \lambda_3$, resulting in a pancake shaped ellipsoid (3.8b); and spherical diffusion, with $\lambda_1 \simeq \lambda_2 \simeq \lambda_3$, not favoring any direction (3.8c).

3.6 Crossing neuronal pathways

The previous section introduced the physics of diffusion and how diffusion is measured. In addition, models to approximate the diffusion signal in order to gain information about neuronal microstructures were proposed. The signal resulting from diffusion imaging describes only an approximation of the underlying diffusion process since an axon radius ranges from 0.1 to $10\mu m$. Conventional diffusion MRI acquisitions comprise a voxel spacing of 1 to $5mm$ [44, 45]. Therefore, voxels contain hundreds of thousands of axons. This leads to the fact that multiple diffusion directions are accumulated to form the final MRI signal, which results in complex diffusion profiles. Of course, diffusion MRI parameters, such as voxel size, diffusion gradient strength, and diffusion time can be

adapted to reduce the mentioned partial volume effect and increase the accuracy of the signal. However, this requires stronger magnetic fields, stronger than the $3T$ MRI scanners commonly used. In addition, adjustments, such as increased gradient strength or diffusion time, eventually lead to higher acquisition times, which are no longer clinically feasible. Furthermore, DTI is a simple reconstruction method, unable to model more than one diffusion maximum caused by the Gaussian assumption. Figure 3.9 illustrates the problem of complex intra-voxel diffusion profiles. Respective diffusion tensor reconstructions are shown in the second row. As one can see, multiple diffusion directions within one plane lead to planar diffusion profiles, which imply no distinct direction.

Evidently, advanced acquisition and reconstruction methods are needed to provide an examination of the true underlying diffusion profile. For this reason, innovative diffusion imaging and reconstruction techniques aiming to overcome the previously mentioned limitations are explained in brief and discussed with respect to their applicability for signal reconstruction. Section 3.6.1 introduces challenging diffusion profiles, which require advanced modeling techniques, followed by HARDI reconstruction methods, discussed in Section 3.6.2. In this course, state of the art reconstruction methods, including their advantages and disadvantages, are listed in order to determine the most appropriate for the issues discussed in this thesis. Acquisition aspects for HARDI are presented in Section 3.6.3.

3.6.1 Challenging diffusion profiles

One has to understand the complex nature of neuronal pathways and resulting possible fiber configurations in order to evaluate diffusion signal reconstruction techniques and the accompanying modeling problems. A brief overview regarding complex diffusion profiles as well as resulting visualization and application issues are presented in the following.

Challenging diffusion profiles occur in cases where neuronal pathways kiss, cross or fan within one voxel. As mentioned before, these diffusion profiles can not be modeled using DTI. The exact percentage of voxels requiring advanced
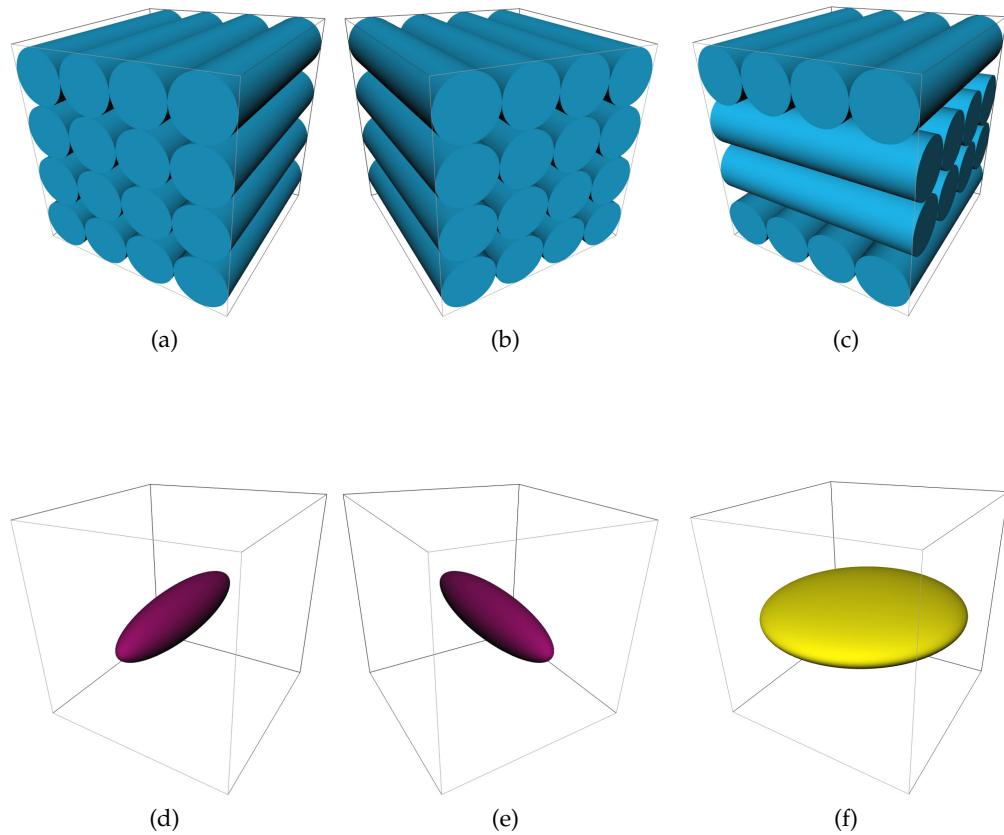
Figure 3.9: Result of DTI-based modeling of complex diffusion profiles: The top row shows the fibers, illustrated as blue tubes, within one voxel and the bottom row describes the resulting DTI diffusion ellipsoid. Single fiber populations (3.9a, 3.9b) result in linear diffusion ellipsoids (3.9d, 3.9e) and multiple intra-voxel orientations (3.9c) in a planar diffusion model (3.9f).

reconstruction strongly depends on the acquisition protocol which defines the voxel extent as well as gradient properties. However, it is assumed that complex intra-voxel distributions have a great impact in terms of fiber reconstruction accuracy [44, 45].

The definition of sufficient acquisition protocols is a challenging task: On the one hand DTI comprises low acquisition requirements, such as low gradient

sampling and timing; on the other hand, DTI leads to planar or even spherical diffusion profiles in cases of challenging intra-voxel populations. Neglecting the potential false information resulting from DTI leads to severe reconstruction and visualization misinterpretations. In terms of tractography, streamline algorithms are prone to integration errors. The uncertainty of neuronal pathway reconstruction is a known problem and discussed in state of the art DTI tractography research [14, 39, 51]. In clinical applications, diffusion imaging poses a promising contribution in terms of fiber integrity examinations and neurosurgical planning. However, confusing fiber crossings and lesions, such as present in tumor infiltrations or MS, can lead to severe subsequent false interpretations. In both cases, similar DTI diffusion distributions occur since lesions cause an isotropic diffusion profile [120]. This is where HARDI contributes to further diffusion image processing since it solves challenging intra-voxel diffusion profiles and therefore, distinguish between crossings and true isotropic distributions.

Figure 3.10 shows a single fiber distribution and existing complex white matter configurations of the brain. In fact, DTI is only able to solve the linear diffusion distribution, as illustrated in Figure 3.10a. Diffusion distributions, shown in Figure 3.10b, 3.10c, and 3.10d result in the same DTI diffusion profile, which is either planar, as shown in Figure 3.8b or spherical, as illustrated in Figure 3.8c.

As introduced in Section 2.4 the *centrum semiovale* is a region in the brain, comprising challenging diffusion profiles. The CC, the CST and the SLF cross within single voxels.

In the following subsection, state of the art methods aiming to reconstruct the true underlying diffusion PDF from the diffusion signal are explained briefly. In addition, a discussion in terms of accuracy and acquisition time is presented in order to define the most appropriate reconstruction method which is used for visualizations in this thesis.

3.6.2 High angular resolution diffusion imaging

The goal of reconstruction methods for HARDI data is to transform the diffusion signal in a probability density function (PDF), describing the degree of
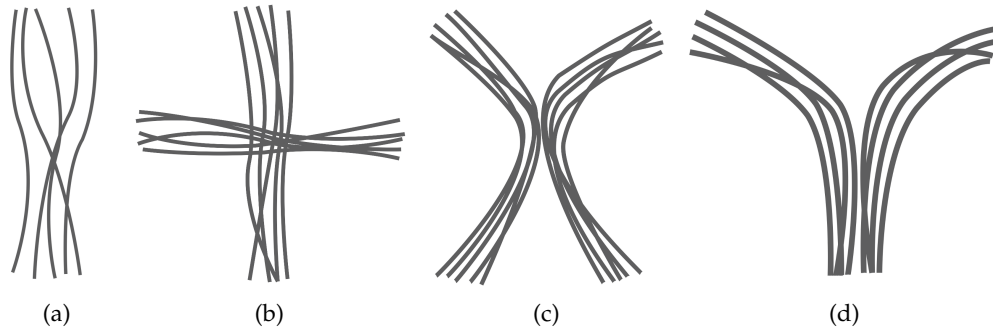
Figure 3.10: Fiber configurations requiring an advanced reconstruction scheme: Single intra-voxel fiber pattern 3.10a and more challenging diffusion distributions, such as fiber crossings 3.10b, kissings 3.10c and fannings 3.10d.

diffusion into any spatial direction. For this purpose, several methods were designed and their concepts are explained and evaluated briefly in the following. For a more detailed discussion see [44, 45].

Popular HARDI reconstruction techniques include diffusion spectrum imaging (DSI) [123], Q-ball imaging (QBI) [117] as well as spherical deconvolution (SD) [114]. The output of each method is a local PDF on a sphere, the orientation distribution function (ODF). The ODF describes the probability of water molecules diffusing into any spatial direction. Thus, it characterizes intra-voxel fiber populations. As in DTI the diffusion ellipsoid, the diffusion glyph is the geometrical representation of the ODF and describes the scatter pattern of molecular movement. For this work, QBI [117] was chosen as a signal modeling technique. Subsequently, QBI and the analytical reconstruction utilizing a spherical harmonic basis are discussed in greater detail. However, in order to understand HARDI acquisition and reconstruction methods, the q-space has first to be introduced and explained.

q-**space**

As discussed earlier, measured signals in MRI are encoded in phase and frequency and result from applied gradients which differ in directions and intensities at distinct acquisition time points. In conventional MRI, signals are arranged in *k*-space, a coordinate system identified by acquisition parameters. A Fourier transform is used to map the MRI signal in *k*-space to the position encoded visual image. In diffusion imaging, a similar coordinate system is defined, the *q*-space. The *q*-space is a three-dimensional space determined by the vector $\mathbf{q}$, which is defined as $\mathbf{q} = \gamma \delta \mathbf{G}$, where $\mathbf{G}$ is the diffusion gradient vector and as previously defined γ represents the gyromagnetic ratio and δ is the gradient pulse duration time. The diffusion orientation is the direction of $\mathbf{q}$, the orientation in question. The diffusion strength, is characterized by the *b*-value. Its length is proportional to the gradient strength $\mathbf{G}$. As a result, each diffusion weighted sequence characterizes a certain position in *q*-space. More precisely, one diffusion sequence determined by a diffusion gradient (strength and direction) for the whole volume has one distinct coordinate in the *q*-space. Varying diffusion strengths result in varying radii and varying orientations of *q* sample different positions of the *q*-space. A single acquisition results in one diffusion weighted brain volume for a specific diffusion gradient. For example, a single DWI sequence reflects one point in *q*-space. To estimate the whole underlying diffusion pattern within one voxel, several acquisitions have to be performed with different $\mathbf{q}$-vectors. Similar to conventional MRI, *q*-space data is subject to a Fourier transform for every position in the brain in order to obtain the actual diffusion pattern: the diffusion signal for a given orientation and strength. In order to further illustrate the reconstruction, the signal has to be reorganized in a way that a *q*-space sample is present at every brain position. The Fourier transform relates raw *q*-space data to a diffusion PDF for each voxel. Figure 3.11 demonstrates the *q*-space and the according volume with the applied gradient.

Orientation distribution function

In challenging fiber configurations, such as crossing intra-voxel distributions, two types of orientation distribution functions are distinguished. Since the mea-

(a)   (b)
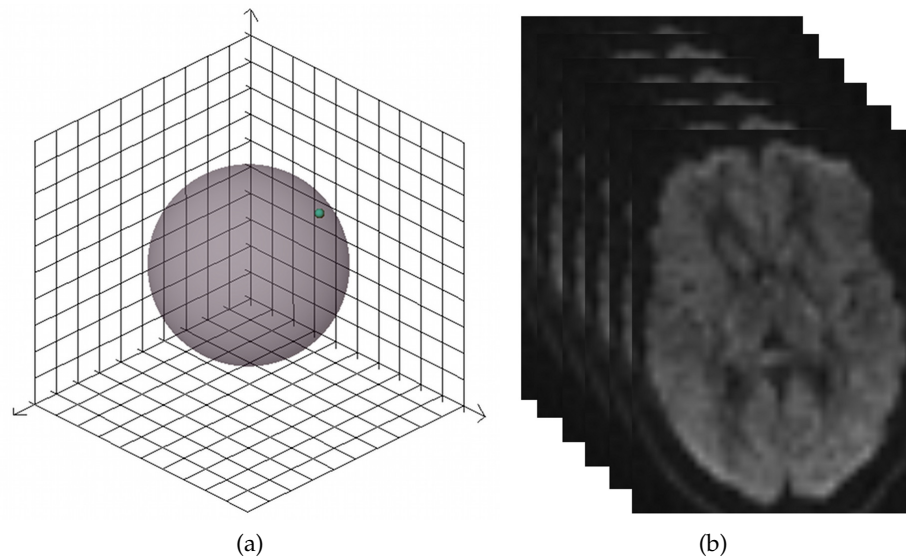
Figure 3.11: Illustration of the *q*-space: One point in *q*-space (3.11a) corresponds to a
diffusion weighted MRI sequence with a certain gradient direction and *b*-
value (3.11b).

surements are based on the diffusion of water molecules and not fiber courses
themselves, the initial ODF is considered as the diffusion orientation distribu-
tion function (dODF). After postprocessing, the fiber orientation distribution
function (fODF) represents the true underlying fiber distributions. Caused by
the fact that diffusion does not only takes place within the fiber course but also
on a smaller, perpendicular scale, the dODF is usually blurred. Increasing the
b-value via increasing the gradient strength leads to a higher angular resolution
and sharper dODFs, thus towards the fODF. However, diffusion MRI settings
are challenging and parameters have to be adjusted carefully. For example, a
higher *b*-value leads to a lower signal to noise ratio (SNR). This is caused by
the fact, that applying a longer diffusion time results in a higher variance since
more molecules displace in general. Furthermore, a crucial factor in diffusion
imaging is the acquisition time: Increasing the *b*-value by increasing Δ leads to
a longer scanning time, which is in many cases not implementable in a clinical
environment. However, increasing the $|\mathbf{q}|$ requires higher Tesla MRI scanners

than commonly available. For this reason, and also because validation of the true fODF is demanding, the dODF is commonly used. In the following, ODF equals dODF.

Diffusion spectrum imaging

DSI was introduced by Wedeen et al. [123]. It is a model-free approach, which means it does not make any assumptions about the shape of the PDF or underlying fiber configurations. It is the most intuitive and earliest approach for HARDI reconstruction. A dense sampling of the whole sphere in q-space is used and a Fourier transform is applied in order to reconstruct the diffusion profile for each voxel. A DSI sequence consists of 515 diffusion weighted images, each acquired with varying $\mathbf{q}$-vectors. As mentioned earlier, different $\mathbf{q}$-vectors, varying in strength and orientation, result in different radii of the sampling sphere, as illustrated in Figure 3.12a. A b-value of 0 has no diffusion weighting and therefore no gradient strength. As such, it represents the diffusion sequence at the center of the sphere in q-space. Due to the dense q-space sampling, DSI leads to a detailed description of the diffusion of complex intravoxel diffusion distributions. Additionally, DSI comprises no hypothesis about the underlying diffusion pattern and maps the entire field of diffusion. However, several profound disadvantages exist which make the use of DSI impractical: The most limiting factor of DSI is the acquisition time. Sampling a whole sphere in q-space requires a large number of q-vectors with varying b-values, which leads to high acquisition times. For this reason, whole brain studies are challenging. In the worst case the image resolution must be decreased, in order to implement DSI acquisitions for clinical use. This, in turn leads to severe partial volume effects. In addition, hardware requirements are high: At least a 3T MRT is required with the capability of high gradient strengths. Furthermore, DSI assumes infinite short gradient pulses, but in practice these are not possible. Summarizing, tractography approaches which successfully reconstruct neuronal pathways, such as the one proposed by Wedeen et al. [124], lead to impressive results, however the acquisition setup is challenging.

(a)   (b)
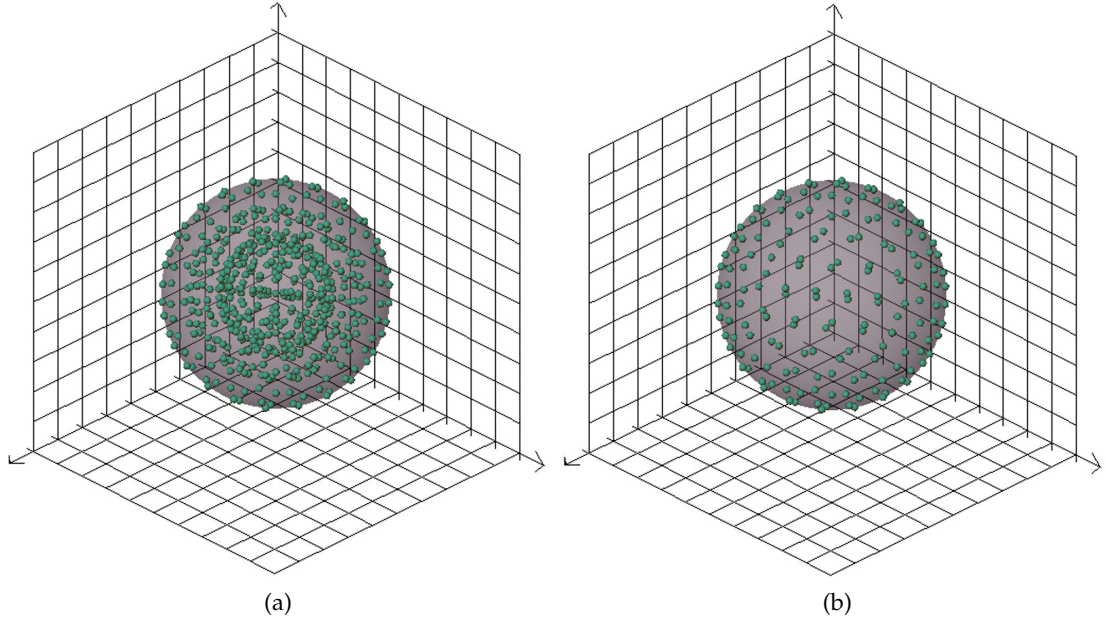
Figure 3.12: Different samplings of the q-space: Green points indicate image sequences defined by a specific q-vector. Sampling the whole sphere requires q-vectors with varying b-values (3.12a), whereas shell-sampling uses a constant b-value (3.12b).

Spherical deconvolution

SD, as introduced by Tournier et al. [114] aims to reconstruct the fODF rather than the dODF directly from the signal. The assumption is that the signal is the sum of single fiber distributions, each weighted with its fiber density: Each signal is considered as a convolution of single fiber populations with the actual fODF. Mathematically, one can write

$$S(\mathbf{v}) = \int f(\hat{\mathbf{x}}) R(\mathbf{v}; \hat{\mathbf{x}}) d\hat{\mathbf{x}}, \qquad (3.8)$$

with S is the measured signal, f is the fODF, $\hat{\mathbf{x}}$ a specific orientation, $R(\mathbf{v}; \hat{\mathbf{x}})$ the measurement for a single fiber population which is the response function, and $\mathbf{v}$ the settings of the pulse sequence. The signal has its peaks in two orientations: $\hat{\mathbf{x}}_1$ and $\hat{\mathbf{x}}_2$. As a result, S is approximated by the sum of R rotated according

to both orientations $\hat{\mathbf{x}}_1$ and $\hat{\mathbf{x}}_2$. SD reconstructs the fODF by deconvolving the signal with the measurements for single fiber populations R for the estimated orientations. Therefore, it is a model-based technique and requires a diffusion profile for a single fiber distribution within the dataset. Commonly, the average diffusion signal of voxels covering the center of the CC is used since these are considered as the most anisotropic in the human brain.

QBI

QBI, introduced by Tuch [117], is a very popular reconstruction method for HARDI. Basics of QBI are explained in the following including a short comparison with previously introduced methods.

Tuch demonstrated in [117] that the Funk-Radon transform (FRT) can be used to compute the ODF value $\Psi(\mathbf{u})$ for a direction of interest $\mathbf{u}$ from the diffusion signal of a single shell in q-space. For this reason, QBI is considered as a so called single shell technique. Recall the previously introduced q-space sampling: different positions in q-space result from different gradient strength and gradient directions. However, in single shell methods, only the gradient direction is modified; the diffusion strength remains the same. Using a constant b-value, the sampling forms a shell rather than a sphere in q-space. Figure 3.12 illustrates different q-space sampling approaches.

Applying the FRT for HARDI reconstruction, the diffusion ODF is the radial projection of the diffusion function: Given a spherical function $f(\mathbf{w})$, with a unit direction vector $\mathbf{w}$, the FRT is the integral over the great circle $C(\mathbf{u})$ lying in the plane perpendicular to direction $\mathbf{u}$ through the origin. Mathematically, one can write

$$\Psi(\mathbf{u}) = \int_{C(\mathbf{u})} f(\mathbf{w})dw. \tag{3.9}$$

Using a spherical harmonic (SH) basis to represent the ODF, results in

$$\Psi(\theta, \phi) = \sum_{l=0}^{l_{max}} \sum_{m=-l}^{l} c_l^m Y_l^m(\theta, \phi), \tag{3.10}$$

where $Y_l^m(\theta, \phi)$ represents a spherical harmonic of order l and phase factor m, c_l^m denotes the SH coefficient and l_{max} the truncation order of the spherical harmonics series. SH coefficients modulate according basis functions in order to approximate the underlying diffusion signal.

Analytical solution

Descoteaux et al. [22] presented an analytical QBI approach in order to reconstruct the ODF. The authors proposed modified SH basis functions as well as a Laplace-Beltrami regularization term. The diffusion signal is modeled using the weighted sum of SH basis functions. The proposed modified basis consists of symmetric, real, and orthonormal SH functions Y with elements Y_j:

$$Y_j = \begin{cases} \sqrt{2} \cdot Re\,(Y_k^m), & \text{if } -k \leq m < 0, \\ Y_k^0, & \text{if } m = 0, \text{ and} \\ \sqrt{2} \cdot Img\,(Y_k^m), & \text{if } 0 < m \leq k, \end{cases} \qquad (3.11)$$

where $Re\,(Y_k^m)$ and $Img\,(Y_k^m)$ denote the real and imaginary parts of Y_l^m, respectively, with index $j = j(k, m) = (k^2 + k + 2)/2 + m$ and $k = 0, 2, 4, \ldots, l$ and $m = -k, \ldots, 0, \ldots, k$. Reformulating Eq. 3.10 according to Eq. 3.11 results in

$$\Psi(\theta, \phi) = \sum_{j=1}^{R} c_j Y_j(\theta, \phi), \qquad (3.12)$$

for each of the N gradient directions (θ, ϕ) with $R = (l_{max} + 1)(l_{max} + 2)/2$, the number of terms in the modified SH basis. With previous SH coefficient estimation, the signal is computed for any diffusion direction of interest (θ, ϕ), using Eq. 3.12.

Assume $\mathbf{S}$ to be an $N \times 1$ vector representing the diffusion signal for each applied diffusion gradient and $\mathbf{B}$ is the $N \times R$ matrix consisting of the modified SH basis:

$$\mathbf{B} = \begin{pmatrix} Y_1(\theta_1, \phi_1) & Y_2(\theta_1, \phi_1) & \ldots & Y_R(\theta_1, \phi_1) \\ \vdots & \vdots & \ddots & \ldots \\ Y_1(\theta_N, \phi_N) & Y_2(\theta_N, \phi_N) & \ldots & Y_R(\theta_N, \phi_N) \end{pmatrix}. \qquad (3.13)$$

Further, $\mathbf{C}$ is the vector $R \times 1$, containing the SH coefficients c_j which are unknown. Coefficients are estimated by solving the over-determined linear system $\mathbf{S} = \mathbf{BC}$. Descoteaux proposed using a least-squares estimation to compute the coefficient vector:

$$\mathbf{C} = (\mathbf{B}^T \mathbf{B} + \lambda \mathbf{L})^{-1} \mathbf{B}^T \mathbf{S}, \tag{3.14}$$

where $\mathbf{L}$ represents the introduced Laplace-Beltrami $R \times R$ regularization matrix, which aims to control the impact of SH basis functions to avoid perturbations caused from noise. The Moore-Penrose pseudo-inverse is used in order to compute $\mathbf{B}^T$. The proposed analytical solution equation 3.12 is used for any spatial direction of interest in order to determine the probability of molecular displacement.

Discussion of HARDI reconstruction methods

QBI features several advantages compared to previously introduced methods. These issues are discussed in the following.

Unlike DSI, QBI samples only the shell of the sphere in q-space and is therefore considered as a single shell method. The single shell approach demands a fixed gradient strength and b-value. This leads to a faster acquisition and reconstruction time for QBI-based methods. Furthermore, using the introduced analytical reconstruction, ODF reconstruction is of low computational complexity. The application of HARDI in clinical environments is challenging mainly due to timings. QBI significantly reduces timings: First, due to its lower acquisition requirements and second, due to the fast reconstructions provided by analytical QBI. For this reason, QBI is considered as a contribution towards implementing HARDI in clinical settings. As a matter of fact, DSI is more precise than QBI due to the denser q-space sampling. However, a comparison of DSI and QBI by Tuch et al. [118] showed good similarities for the ODF peak directions of both methods. As a result, using QBI instead of DSI is reasonable.

The advantage of SD over DSI and QBI is the direct estimation of the fODF. However, this is only superficially true: In fact, SD is susceptible to noise, which easily leads to false positive peaks in the fODF [113]. This is where regularization terms are needed to prevent the modeling of noise. A further limitation

of SD is its strong dependency on a model; the response function, which describes a single fiber diffusion profile. This dependency occurs because the final deconvolution kernel is formed by sums of the response function. In fact, different fiber bundles sizes exist and it is not possible to model different axon sizes, fiber densities, and packing configurations with one diffusion model.

Recently, methods have emerged which consider the mentioned disadvantages: Constrained spherical deconvolution (CSD) [113] incorporates a regularization and the approach, proposed by Kaden et al. [48], uses a different response function for diffusion signal filtering. However, they are in the early stages of development and no overall solution to the named issues or a detailed evaluation exists. For this reason, QBI was considered more advantageous than SD due to SD's sensitivity to false positive detection as well as QBI's flexibility in terms of a priori assumptions.

Choosing an adequate SH model order and weighting faction is an important issue for the presented analytical QBI approach. Studies have shown that a regularization term weighting of $\lambda = 0.006$ and a SH order of $l = 4$ provides sufficient results. More precisely, this order is high enough to classify multiple fiber populations in a voxel [20, 31] and low enough to avoid overmodeling perturbations due to noise in the input diffusion MRI signal [22]. Summarizing, QBI provides a good balance between acquisition requirements, computation time, and a-priori assumptions [22, 116]. It was chosen for ODF reconstruction and implemented as a MeVisLab image processing module according to [22].

Figure 3.13 shows results for ODF reconstruction illustrated via glyph rendering. ODFs are visualized using a GPU raycasting approach for spherical functions, as proposed by Peeters et. al [75]. Large glyph magnitudes reflect high probabilities for molecular movement in the direction of interest. In Figure 3.14 ODF renderings of voxels comprising various neuronal pathways crossing are displayed.

3.6.3 Acquisition and reconstruction aspects of HARDI

HARDI models complex intra-voxel diffusion profiles such as fiber crossings, kissings or fannings. However, results strongly rely on acquisition and re-
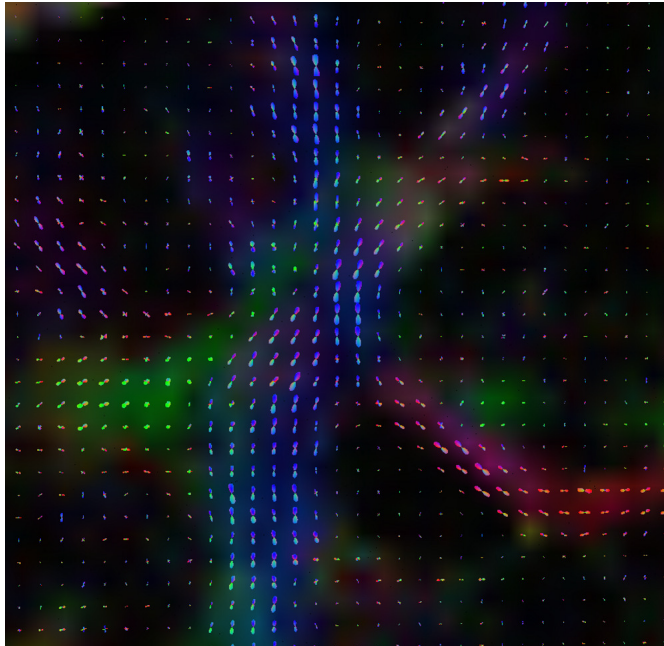
Figure 3.13: Directional color coded GPU glyph rendering: ODFs are normalized and the radius of a glyph highlights the local degree of diffusion in the specific direction.

construction parameters. As a result, a careful definition of the parameters is needed in order to provide a reliable modeling. In the following, acquisition and sampling aspects of HARDI are explained and discussed.

Acquisition parameters

For HARDI acquisitions, parameters such as the b-value, the number of gradients, the signal to noise ratio (SNR), and the spatial resolution of the dataset are important. In addition, isotropic voxel sizes are preferred for subsequent data processing such as tractography. Therefore, the decision of best imaging parameters is challenging. A trade-off between best parameter settings and acquisition time exists: b-values can be enhanced in order to obtain a more accurate mapping of the diffusion process since higher b-values result in a wider sampling of the q-space. However, a trade-off is reported between high b-values and the SNR: As explained earlier, the b-value is proportional to the square of
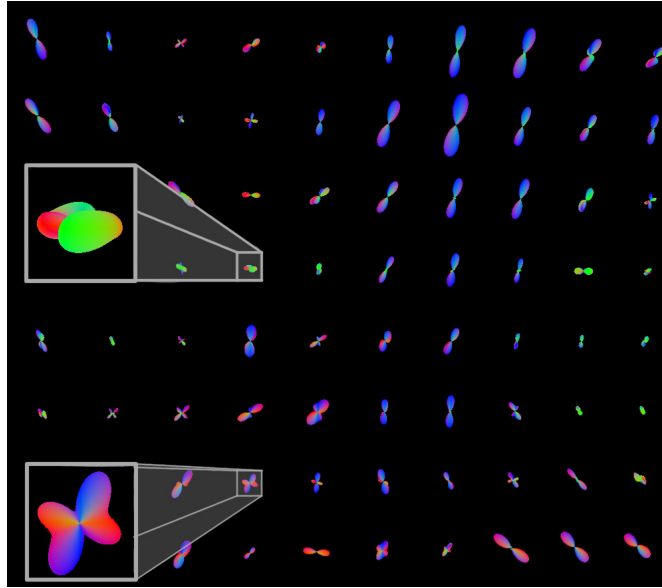
Figure 3.14: Glyph representations for challenging diffusion profiles in the *centrum semiovale*: Red parts belong to the CC, green parts to the SLF, and blue parts partly to the CC and partly to the the CST.

the product of the diffusion gradient strength, $|\mathbf{q}|$, and the diffusion time interval, Δ. As a result, increasing the b-value in order to enhance the angular resolution of the PDF is realized by increasing either the gradient strength or the diffusion time interval. A shorter Δ results in a more isotropic diffusion profile since the water molecules have less time to travel far from the center. Contrary, a larger Δ leads to an increased angular resolution which means a sharper diffusion PDF in cases where the underlying diffusion profile is not isotropic. For isotropic diffusion processes, adapting Δ has no impact on the resolution of the PDF since the movement is stationary and does not change over time. However, increasing the b-value by a larger Δ also results in a lower SNR since more molecules displace in a larger diffusion time interval, provoking additional noise. Therefore, a feasible option for increasing the b-value is to increase the gradient strength $|\mathbf{q}|$, which results in a higher SNR and allows the capture of complicated diffusion profiles such as crossings at low angles [84].

However, the maximum possible gradient strength is subject to the MRI scanner.

The application of more diffusion gradients than in DTI is crucial for HARDI, especially for modeling crossings at low curvature. A lower gradient resolution leads to high angular errors. However, since Δ strongly influences the acquisition time, an optimal solution has to be found for this trade-off. In fact, the most optimal choice depends on the intra-voxel configuration under consideration. Various diffusion profiles require different settings for a most accurate PDF. For example, a reconstruction of fibers in the *centrum semiovale* requires a higher number of applied gradients than those running in the center of the CC which can be mapped by DTI as well. However, in [85] it was reported that after a certain number of applied gradients, the information does not improve significantly. Since the number of gradients is crucial in terms of the acquisition time, the lowest number of gradients is desirable. In addition, the application of many gradients leads to longer acquisition time, which is often not even realistic for research purposes.

After data acquisition, the definition of the appropriate order of the spherical harmonics basis function for analytical QBI is challenging. The adequate model order depends on the underlying diffusion profile in question. For example, according to Prčkovska [84], fiber crossings at high angles, such as 90° require a lower order, $l = 4$, than crossings at low angles, 60° which are best modeled with higher SH orders such as $l = 6$. However, a high SH order can result in modeling noise when a high b-value such as $4000s/mm^2$ is used as well.

Prčkovska et al. [84,85] presented a first study for optimal acquisition schemes for HARDI. The authors acquired diffusion scans with varying HARDI parameters and evaluated them as well as the reconstruction order with respect to intra-voxel fiber configurations. In the *centrum semiovale* of a human brain, neuronal fiber crossings in the range between 60° and 90° are observed within one voxel. More precisely, crossings of 90° are observed in the *centrum semiovale*: The crossing of the corona radiata (CR) and the CC is detected with a b-value of 1000, 24 applied gradients and a SH model order of 4. However, fibers belonging to the SLF require a higher b-value. Summarizing the parameter study in brief, for reconstructing pathways in the *centrum semiovale*, a b-value of 2000,

which does not provoke too much noise, and number of gradients in the range of [48;72] is advised if a SNR of 20 is achieved. This setting meets a clinically feasible acquisition time of 2 to 11 minutes. The suggested model order for QBI is 4 or 6, depending on the diffusion profile of interest. However, the authors did not perform a whole brain scan, but only acquired slices mapping the region in question. Despite this fact, the represented study makes a step forward in implementing HARDI in a clinical environment and therefore, is considered as a huge contribution to diffusion imaging.

Sampling a sphere

Both, gradient determination for diffusion data acquisition as well as ODF evaluation require uniformly distributed points on a sphere. Techniques to compute these points are introduced in the following.

Since the principal diffusion direction within a voxel is previously unknown, a set of gradients is applied along which the distribution of water molecules is measured. These directions and the according signal are used in turn to determine the ODF. The applied gradient directions should be uniformly distributed in three-dimensional space and sample a sphere with high angular resolution in order to appropriately measure diffusion. However, a trade-off between sampling accuracy and acquisition time exists, as described in the previous section. In order to define diffusion directions of interest a certain number of points n have to be placed uniformly on a sphere. The electrostatic repulsion algorithm [46] is one approach to accomplishing this task and can be used for an arbitrary number of points. Imagine the n points to be distributed are equally-charged electrons. The electrons repel each other on the surface of the sphere with a inverse-square force until a convergence criterion is reached.

A further approach to defining point configurations in 3D is a geometric subdivision of an icosahedron, a platonic solid with twenty faces approximating a sphere. This approach does not need a convergence criterion. Instead, the tessellation order is the parameter defining the amount of points, used to sample the sphere. This approach is only possible for certain point numbers: An icosahedron tessellation of order 1 results in 12, order 2 in 42, order 3 in 162, and of

order 4 in 642 points on a sphere. Figure 3.15 shows two different samplings on a sphere, resulting from icosahedron tessellation.

(a)   (b)
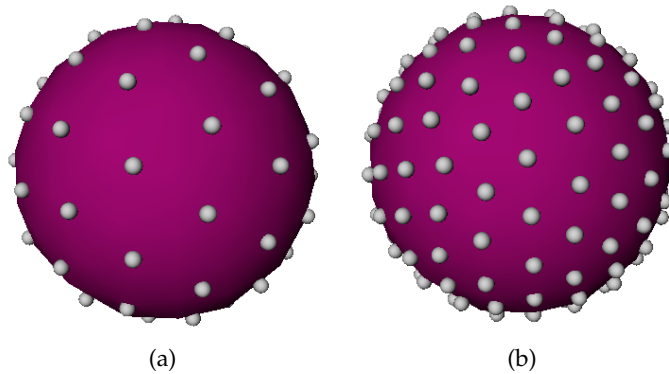
Figure 3.15: Points sampling a sphere with different resolutions: Sampling points are displayed on a unit sphere's surface. A lower angular resolution is obtained by 60 points (3.15a), whereas a higher sampling is obtained by 162 points (3.15b).

The in the following presented approaches use different tessellation orders for ODF evaluation.

3.7 Diffusion datasets

The previous sections provided background information for diffusion acquisition as well as reconstruction methods. Furthermore, the trade-off between clinically feasible acquisition times and diffusion profile accuracy was discussed. As a result, HARDI requires carefully estimated acquisition parameters such as the b-value and the number of gradients as well as reconstruction parameters. In terms of human brain HARDI datasets, acquisitions are currently based on voluntary subjects since scanning times of more than 15 minutes are not clinically feasible. For this reason, HARDI hardware phantoms pose a real contribution. The following sections present details of diffusion datasets in general, as well as parameter details of the datasets available for reconstruction and visualization approaches in this thesis.

3.7.1 Diffusion data

Compared to simple T_1 or T_2-weighted MRI, an additional gradient scheme is applied in diffusion imaging to record molecular movement. The resulting signal describes the diffusion probability for a certain direction. Therefore, the output of a diffusion weighted imaging sequence is not just one scalar but a scalar for each diffusion direction. More precisely, a scalar is obtained for each applied diffusion direction of interest for each voxel. As a result, a diffusion weighted volume has the following extent: *resolutionX* $\times$ *resolutionY* $\times$ *#slices* $\times$ *#diffusion gradients*. In addition to the diffusion weighted sequence, an anatomical volume, the baseline image which is commonly a T_2-weighted MRI sequence, is acquired.

3.7.2 Phantom data

Phantom data comprise several benefits: First, they are independent from acquisition aspects, such as timing and movement. Second, they provide ground truth for method evaluation since fiber pathways are known. Therefore, an evaluation of diffusion reconstruction models, classifiers or tractography approaches is feasible. On the other hand, by making phantom data available for a larger community, evaluation of diffusion approaches amongst different research groups is possible. For this reason, hardware phantoms are considered as vital material for diffusion visualizations.

   In this thesis, a HARDI hardware phantom was used which imitates a coronal human brain slice [30,79,81]. It comprises intra-voxel fiber configurations which are commonly considered as challenging: Fiber crossings, low angle crossings, fannings, kissings as well as pathways with high curvature. The phantom was originally provided by the Laboratoire de Neuroimagerie Assistée par Ordinateur (LNAO, France) for the Fiber Cup, a tractography contest at the MICCAI conference in 2009. This contest was created and designed for the evaluation of existing and novel tractography algorithms. The presented HARDI phantom poses a state of the art diffusion dataset which is beneficial in terms of evaluating and rating own diffusion reconstruction as well as visualization approaches. Furthermore, a direct comparison of own approaches with MICCAI tractogra-

phy contest results is feasible. The according fiber ground truth is shown in Figure 3.16, in combination with the b_0 image. The data was acquired with

Figure 3.16: MICCAI Fiber Cup hardware phantom: The dataset imitates a coronal human brain slice and comprises challenging intra-voxel fiber configurations such as fiber crossings, kissings, and fannings.

two repetitions and 64 image encoding gradients, uniformly distributed over a sphere. For the presented work, the two repetitions were averaged for further processing. The dataset size was 64×64 voxels with a uniform voxel size of $3mm$. Of the different diffusion sensitizations provided, the dataset with a b-value $2000s/mm^2$ was used since higher b-values can easily lead to overmodelings.

3.7.3 Human brain data

A whole human brain HARDI scan was examined besides the previously introduced phantom dataset. The dataset is by the courtesy of Poupon et al. [80]. The authors built up a HARDI database for neuroscientists, aiming to examine

the anatomo-functional connectivity of the human brain. It comprises 60 slices with a resolution of 128×128 and a voxel size of $1.875 \times 1.875 \times 2mm$, which is considered as isotropic. HARDI data was acquired with a uniform gradient direction scheme with 200 directions and a b-value of $3000s/mm^2$. In addition, a baseline image, a T_2-weighted MRI sequence, was provided.

Part II

Diffusion profile classification

4 HARDI-based diffusion characteristics

4.1 Overview

The previous chapter introduced the unique ability diffusion imaging provides for infering the neuronal network from local molecular diffusion. Fiber tracts can be reconstructed since diffusion is characteristic in regions with oriented structures. This chapter starts with scientific questions regarding diffusion classification in Section 4.2 and a literature review on diffusion classifiers in Section 4.3 before explaining the details of ODF evaluation in Section 4.4. Subsequently, two approaches developed to divide diffusion profiles are introduced and discussed. The first approach is a global method called morphological fiber classifier (*MFC*), published in [101] and discussed in Section 4.5. The second approach is named isotropic single multiple diffusion classification index (*ISMI*). *ISMI* is a local, ODF-based anisotropy measure which was published in [95] is introduced in Section 4.6. The chapter closes with a discussion on diffusion indices in Section 4.7.

4.2 Introduction

HARDI methods are more advantageous than the well-known DTI model because they are able to describe more than one fiber orientation within a voxel. Hence, the differentiation between challenging intra-voxel fiber configurations such as fiber crossings, kissings or fannings and single fiber configurations is feasible. However, HARDI approaches result in one spherical PDF for each voxel which is difficult to interpret, especially if one is not familiar with this kind of data. Questions arose regarding which benefits the detailed diffusion information provides and how it can be simplified.

The following questions are of interest regarding the diffusion PDF:

- What is the meaning of the function?

- How can a spherical function be simplified to provide a significant yet simple understandable contribution?

- How is the function used for tractography and visualizations?

- What is the contribution of the detailed diffusion information to neurosurgical questions and fundamental neuroscience?

Anisotropy indices aim to reduce the information of the diffusion probability function to a meaningful scalar representation. This scalar classifies the underlying diffusion and thereby the neuronal fiber configuration for a single voxel. The following three classes exist: isotropic diffusion profiles, characterizing gray matter regions, and anisotropic distributions which represent white matter regions. White matter voxels are further classified as containing single or multiple fiber distributions. Indices are used in tractography approaches to determine the probability of certain directions as well as to answer clinical questions such as the integrity of certain neuronal pathways.

In the case of multiple diffusion orientations within one voxel, more sophisticated propagation techniques are required in order to reconstruct the underlying fiber courses. ODF evaluation, with respect to local and global tract characteristics, is essential since integration errors lead to a false fiber representation. Information about the underlying fiber distribution assist in improving fiber propagation: Approaches benefit from a previously calculated voxel classification which divides diffusion profiles into single or multiple fiber populations: tracking directions are determined with consideration of the underlying fiber distribution.

In terms of neurosurgical procedures, knowledge about brain tissue is required in many cases. For example, the differentiation into gray and white matter is vital for neurosurgical planning: The surgeon has to define an access path for the intervention and both white and gray matter include structures at risk. In addition, the degree of white matter integrity within one voxel is crucial

in questions regarding tumor infiltration or stroke. The accurate classification of a diffusion profile is of great interest. However, the differentiation between multiple fiber orientations and isotropic diffusion is still a challenging task and object of current research.

The first approach, the *MFC*, consists of a dilation and erosion pipeline. Based on a white matter mask, the idea of *MFC* is to morphologically eliminate voxels where only clusters remain. These clusters represent an estimation of regions containing multiple fiber populations. On the other hand, *ISMI* is an index which successfully differentiates isotropic diffusion and single and multiple fiber populations. This classifier evaluates the spherical probability function resulting from QBI. Results of both classifiers are compared to the well-known general fractional anisotropy (GFA) index using a fiber phantom comprised of challenging diffusion profiles. Results are visualized directly on the fibers represented by streamtubes using a heat color map.

4.3 Related work

In the following, a short literature study is presented which aims to provide an overview of existing diffusion classifiers. In general, diffusion classification indices are categorized into DTI- or HARDI-based.

The fractional anisotropy (FA) [6] index is well-known in DTI. It describes the degree of linearity of a diffusion distribution and is defined as follows:

$$FA = \sqrt{\frac{3}{2}} \frac{\sqrt{(\lambda_1 - \hat{\lambda})^2 + (\lambda_2 - \hat{\lambda})^2 + (\lambda_3 - \hat{\lambda})^2}}{\sqrt{\lambda_1^2 + \lambda_2^2 + \lambda_3^2}}, \tag{4.1}$$

where λ are the tensor eigenvalues and $\hat{\lambda}$ is the trace of the diffusion tensor.

As HARDI emerged, research started to concentrate on indices which are able to evaluate the more complex diffusion probability function and distinguish

intra-voxel diffusion profiles. The GFA index, as introduced by Tuch [117], is the adaption of the FA index to HARDI,

$$GFA = \frac{std(\Psi)}{rms(\Psi)} = \sqrt{\frac{n \sum\limits_{i=1}^{n} \left(\Psi\left(\mathbf{u}_i\right) - \langle\Psi\rangle\right)^2}{(n-1) \sum\limits_{i=1}^{n} \Psi\left(\mathbf{u}_i\right)^2}}. \tag{4.2}$$

Here, $\Psi(\mathbf{u})$ is the ODF value for a diffusion direction of interest $\mathbf{u}$ with $\mathbf{u} = (\theta, \phi)$ and with $\theta \in [0, \pi]$, $\phi \in [0, 2\pi]$. The mean ODF value is indicated by $\langle\Psi\rangle$ and n is the number of samplings on a sphere used to evaluate the ODF. The GFA is computed using SH coefficients as well [84] which is computationally more efficient,

$$GFA = \sqrt{1 - \frac{c_0^{0^2}}{\sum\limits_{l=0}^{l_{max}} \sum\limits_{m=-l}^{l} c_l^{m2}}}, \tag{4.3}$$

for SH model order l and phase m. A well-defined and rotationally invariant version of the GFA was defined by Landgraf et al. [56]. Frank et al. [31] introduced the fractional multifiber index (FMI). The goal of FMI is to define the best describing model order, l, of a diffusion PDF. The authors applied SH basis functions to map the diffusion signal. In order to determine the degree of complexity they propose to analyze SH coefficients,

$$FMI = \frac{\sum\limits_{l=4}^{l_{max}} \sum\limits_{m=-l}^{l} |c_l^m|^2}{\sum\limits_{l=2}^{l} \sum\limits_{m=-l}^{l} |c_l^m|^2}. \tag{4.4}$$

Chen et al. [20] and Descoteaux et al. [21] both proposed a similar diffusion index which is also based on SH coefficients. The three HARDI indices are defined by

$$R_0 = \frac{|c_0|}{\sum\limits_{l=0}^{l_{max}} \sum\limits_{m=-l}^{l} |c_l^m|}, R_2 = \frac{\sum\limits_{l=2}^{l_{max}} \sum\limits_{m=-l}^{l} |c_l^m|}{\sum\limits_{l=0}^{l_{max}} \sum\limits_{m=-l}^{l} |c_l^m|}, \text{ and } R_{multi} = \frac{\sum\limits_{l=4}^{l_{max}} \sum\limits_{m=-l}^{l} |c_l^m|}{\sum\limits_{l=0}^{l_{max}} \sum\limits_{m=-l}^{l} |c_l^m|}. \quad (4.5)$$

In the following, the index will be referenced by R_0, R_2, R_{multi}. The authors aim to directly distinguish intra-voxel fiber distributions based on SH coefficients: The underlying diffusion profile is considered to be isotropic if R_0 is large. However, if R_2 is large, a single fiber distribution is present and a large R_{multi}-value indicates multiple diffusion directions.

4.4 ODF evaluation

In order to characterize voxels as containing isotropic, single or multiple fiber populations, the respective diffusion profile has first to be calculated. Q-ball reconstruction based on SHs is used in this thesis and was explained in detail in Section 3.6.2. The applied regularization parameter for the Laplace-Beltrami smoothing matrix is $\lambda = 0.006$ and the SH order for signal modeling is $l = 4$. In a first reconstruction step, SH coefficients for corresponding basis functions have to be determined in order to approximate the measured diffusion signal. Subsequently, ODF evaluation is performed by solving Equation 3.12 for arbitrary diffusion directions of interest. The applied tessellation order was 3 which results in 162 points which are uniformly distributed across a sphere.

4.5 *MFC*: A morphological fiber classification approach

In the following, the morphological approach for intra-voxel diffusion pattern classification is explained in detail.

4.5.1 Morphological computation pipeline

The *MFC* approach uses global heuristics to differentiate HARDI-based diffusion profiles. The main idea of *MFC* is to morphologically eliminate voxels from a white matter mask where only clusters remain. These clusters represent white matter nodes, which are considered as an estimation of multiple fiber populations. To accomplish this task, a white matter mask is generated in the first step. This mask separates isotropic voxels from voxels with single fiber population. As a result, a white matter, gray matter differentiation is obtained.

For our experiments, thresholded mask images were calculated based on FMI, R_0, R_2, R_{multi}, GFA, and the standard deviation (sDEV) of the diffusion ODF. The respective thresholds were chosen carefully to find a proper balance between gaps in the mask and false positives. The white matter mask features gaps due to the thresholding procedure. For this reason, the second step is to close these gaps by applying a morphological closing using different kernel sizes. Closing consists of a morphological dilation ($2 \times 2 \times 2$) followed by erosion ($4 \times 4 \times 4$). The erosion is performed with a larger kernel size since our goal is to eliminate voxels. The kernel reduces the previously added white matter voxels of the dilation step. As a result, white matter regions become thinner. In the third step, the white matter is further thinned out so that only clusters remain. These clusters represent tract junctions which are considered to comprise complex diffusion profiles. Therefore, a morphological opening with a kernel size of $3 \times 3 \times 3$ is applied. In the fourth step, a median filtered mask image is combined with the previously obtained cluster image to form the final result. Voxels marked in both images are characterized as containing multiple fiber populations whereas voxels marked only in the mask image contain single fiber distributions. This step is necessary due to the dilation in the third step: Some clusters may be enlarged beyond the white matter mask during dilation. For this reason, voxels marked only in the cluster image represent false positives and are ignored.

Summarizing, the presented single steps of the *MFC* pipeline are as follows:

1. Generation of a white matter mask image, separating white and gray matter voxels

2. Morphological closing of the white matter mask with a larger kernel size for erosion than for dilation

3. Morphological opening of the image, resulting from the previous step

4. Logic combination of the result with a median filtered mask image

The resulting image differentiates gray matter and white matter. Further fiber clusters represent complex intra-voxel diffusion profiles.

4.5.2 Results

In the following, *MFC* results are introduced and discussed. In subsequent figures, gray indicates single and white multiple intra-voxel fiber configurations. Black regions include no fiber population and are considered as gray matter.

Recently proposed diffusion indices for HARDI, as introduced in Section 4.3, were implemented in order to define an appropriate white matter mask, as well as evaluate the *MFC*. Results are displayed in Figure 4.1. In case of indices which already differentiate single and multiple fiber distributions, classification results are shown for comparison in the left column of Figure 4.1. Previously defined color encoding is used for mask image visualization as well. However, in order to define the white matter mask for *MFC* computation, voxels containing single as well as multiple diffusion distributions are used. Thresholds for white matter mask generation are determined with the aim of finding a proper balance between gaps in the mask and false positives. They are indicated in Table 4.1. A high diffusion anisotropy degree is indicated by a high GFA-value. For this reason, a single threshold was used to determine the white matter mask, which is shown in Figure 4.1a. GFA mask image results feature gaps in crossings at low angles as well as in fanning regions. As follows, these areas are missing in the *MFC* result as well, which is displayed in Figure 4.1b. FMI relates the weighting of higher order SH coefficients to those

Classifier	Threshold
GFA	0.245
FMI	lower: 0.0025, upper: 0.25
R_0, R_2, R_{multi}	$R_0 = 0.877$, $R_2 = 0.5$, $R_{multi} = 0.6$
sDEV	2.7

Table 4.1: Parameters for calculating the white matter mask for each classificator.

describing isotropic diffusion. To identify the white matter mask and simultaneously indicate the classification power of FMI, we apply two thresholds. The lower threshold identifies white matter in general, a high degree of anisotropy. The higher threshold distinguishes between single fiber population and more complex diffusion distributions. As one can see in Figure 4.1c FMI is not able to classify intra-voxel diffusion without postprocessing. A similar thresholding technique to FMI was applied to the R_0, R_2, R_{multi} white matter mask result. The individual values of R_0, R_2, and R_{multi} are scalars, describing the scaled influence of SH coefficients for the respective model order 0,2, and 4. Therefore, thresholds for each scalar were applied to define the diffusion profile compartment of each voxel. The result is similar to the FMI output and illustrated in Figure 4.1e. Summarizing both classifiers, FMI and R_0, R_2, R_{multi}, a separation of white and gray matter is noisy. In addition, both fail to detect multiple fiber populations per voxel without preprocessing. Their respective *MFC*'s output, as displayed in Figure 4.1d and Figure 4.1f, does not perform better than the GFA index.

The best separation of white and gray matter was obtained from the standard deviation approach, as shown in Figure 4.2a. Further, the corresponding *MFC* detects all multiple fiber areas with no false positives as indicated in Figure 4.2b. Proposed results of the *MFC* pipeline for the hardware phantom are illustrated in Figure 4.3 including the fiber ground truth in Figure 4.3a and the classification result in Figure 4.3b.

For further evaluation, *MFC* was applied in the region of the *centrum semiovale*, in which a known crossing of the CC, CST, and the SLF exist. Figure 4.4 displays *MFC* results, using the sDEV mask image for white, gray matter sep-

aration. Experiments lead to the result that proper thresholds for white matter mask definition are crucial for the success of the *MFC* algorithm. Further, a median filtering of the mask image before or instead of step two in order to close gaps and eliminate false positives seems to be reasonable if one examines the classification results using the GFA index for white matter identification. However, this pipeline leads to poorer classification results since the resulting white matter mask differs too greatly from the original.

(a) Mask GFA

(b) Result GFA

(c) Mask FMI

(d) Result FMI

(e) Mask R_0, R_2, R_{multi}

(f) Result R_0, R_2, R_{multi}
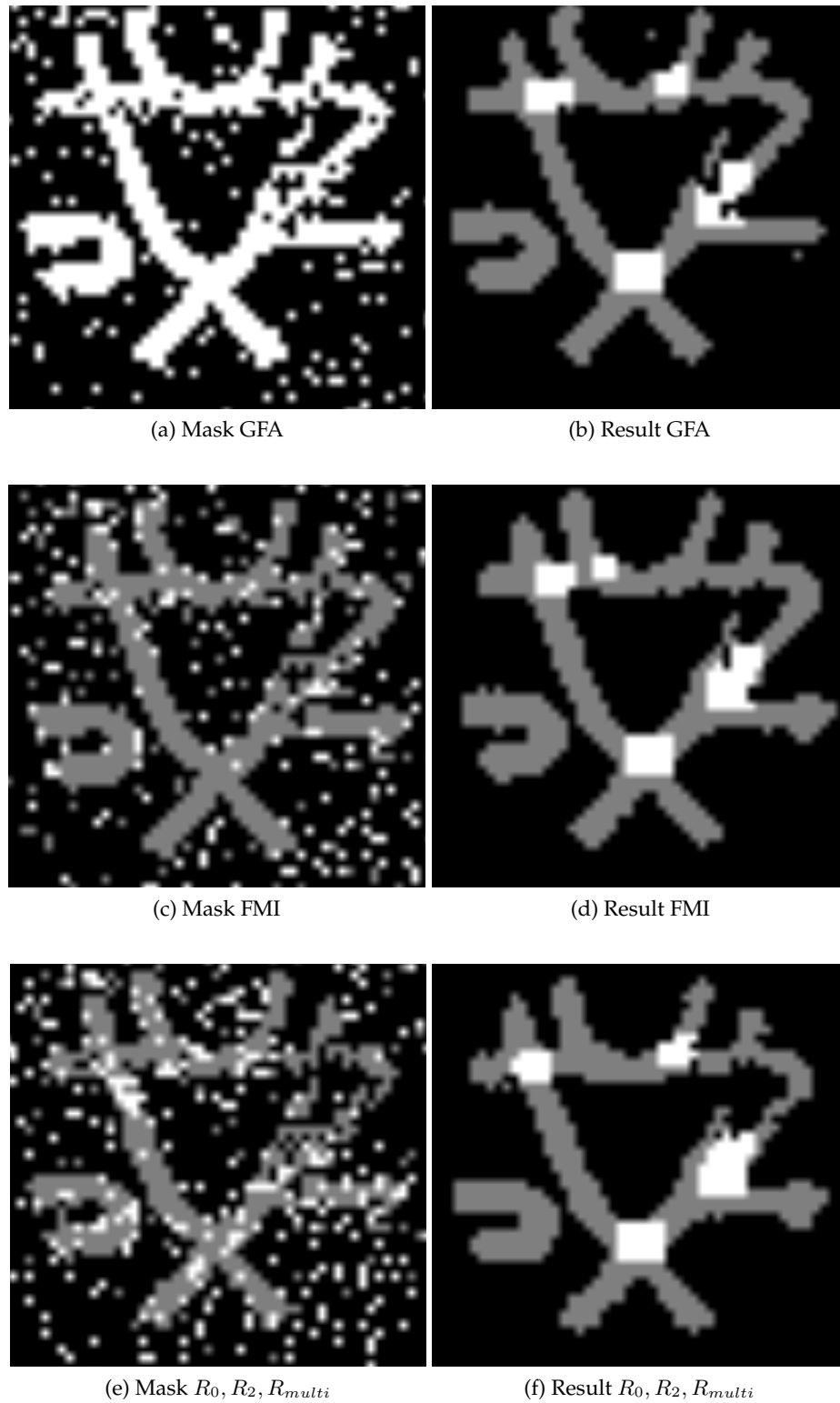
Figure 4.1: *MFC* results of state of the art anisotropy classifiers: Each column represents a diffusion classifier and the according *MFC* result: Black represents no fiber, gray single fiber, and white multiple fiber populations.

(a) Mask sDEV

(b) Result sDEV
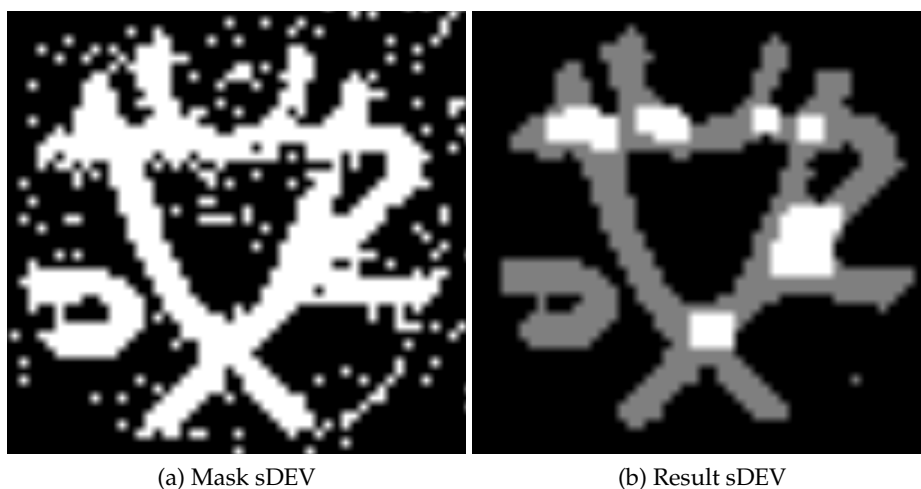
Figure 4.2: *MFC* result for the standard deviation approach: The white matter mask features a good differentiation between gray and white matter voxels (4.2a) and the *MFC* is able to identify all challenging fiber configurations (4.2b).

(a) Ground truth

(b) MFC from sDEV
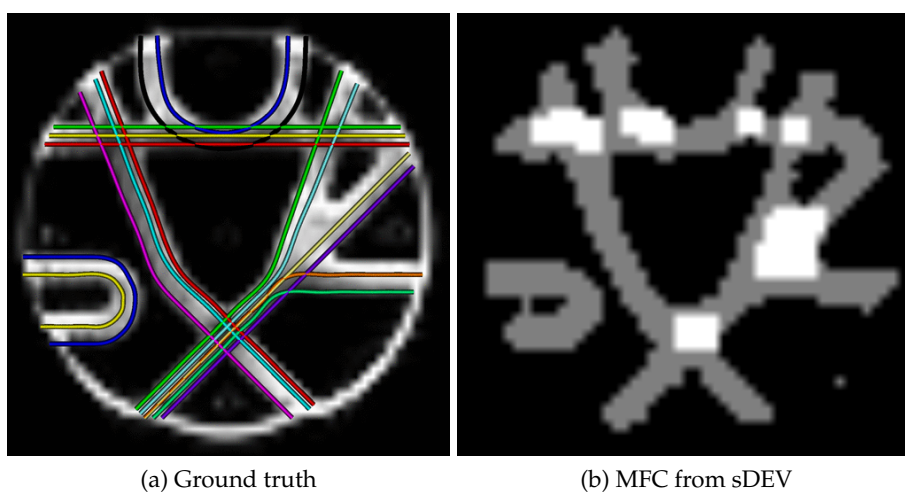
Figure 4.3: *MFC* classification result of the hardware phantom: The hardware phantom ground truth (4.3a) and the proposed *MFC* classification result (4.3b). Classification of single and multiple intra-voxel diffusion distributions: Multiple fiber populations are shown as white voxels, whereas gray voxels represent single fiber populations.
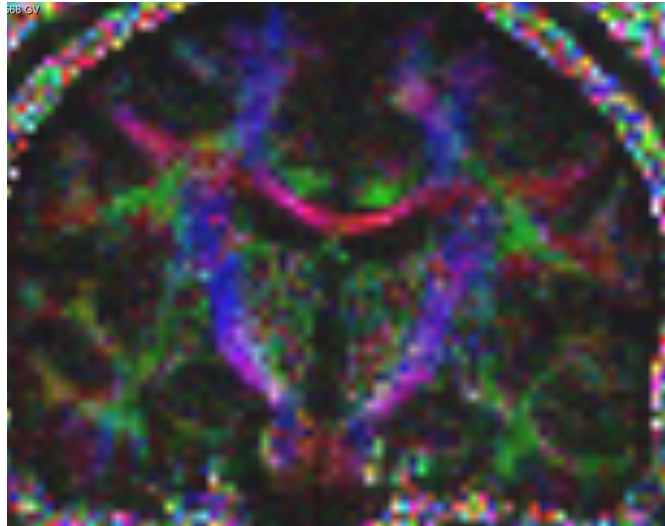
(a)

(b)

Figure 4.4: *MFC* classification result of the *centrum semiovale*: Directional color coding of a coronal diffusion imaging slice of the human brain (4.4a). *MFC* results show classification performance in determining crossings of callosal fibers with the SLF and the CST (4.4b).

4.6 *ISMI*: An ODF-based diffusion profile classifier

ISMI is a local diffusion index using HARDI and is introduced subsequently.

4.6.1 Diffusion classification

ISMI computation is illustrated schematically in Figure 4.5 and includes two
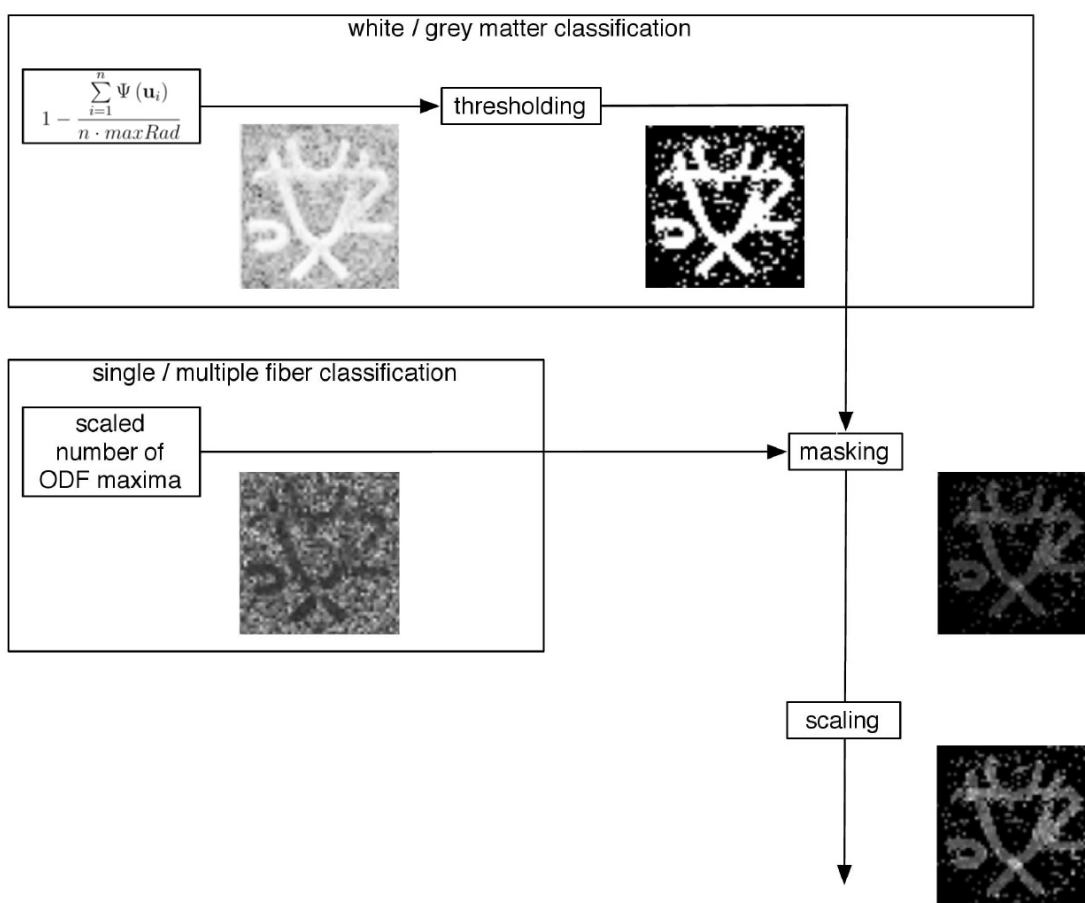
Figure 4.5: Computation pipeline for white matter classification using a phantom dataset: *ISMI* computations are divided into a white/gray matter classification (upper part) and a single/multiple classification (lower part). Both results are combined to form the final classification.

major steps: First, the classification of white and gray matter and second, the

classification into single or multiple fiber populations. For the first step, a fiber mask identifying all voxels including white matter is defined. Both single and multiple fiber distributions belong to the same classification group. To differentiate between white and gray matter, the scaled sum of the min-max normalized ODF is calculated: The ratio between the spherical function and a sphere, defined by the maximal radius of the local ODF, is computed.

The white matter mask is defined by

$$1 - \frac{\sum\limits_{i=1}^{n} \Psi\left(\mathbf{u}_i\right)}{n \cdot maxRad}, \tag{4.6}$$

where n is the number of samples on a sphere resulting from the icosahedron tessellation and $\Psi\left(u\right)$ is the local ODF with diffusion directions of interest $\mathbf{u} = \left(\theta, \phi\right)$ with $\theta \in \left[0, \pi\right], \phi \in \left[0, 2\pi\right]$. The maximum radius of the ODF is indicated by $maxRad$. The next step aims to differentiate between single and multiple intra-voxel fiber distributions and is only considered for voxels already classified as belonging to white matter. To identify multiple diffusion directions, the number of local maxima of the min-max normalized ODF above a certain threshold is determined. For the phantom dataset, a value of 0.5 was chosen and for the human brain 0.6. However, instantaneous visual feedback within the *ISMI* computation pipeline facilitates intuitive parameter tuning. In a last step, both classification outputs are combined to form the diffusion index *ISMI*. As a result, *ISMI* differentiates between isotropic, single, and multiple fiber configurations, as shown in Figure 4.5.

4.6.2 Visualization

Diffusion indices are commonly displayed using bar charts or by assigning values to specific tracts [43, 52]. However, a visualization with respect to certain pathways is advantageous. Therefore, fiber visualization approaches are applied using *ISMI* exemplarily.

Colormap

A heat colormap was used in order to indicate the three different compartments: isotropic, single, and multiple intra-voxel diffusion. For further visualization, isotropic diffusion profiles are displayed in white, single fiber distributions in yellow, and more complex fiber configurations in red.

Fiber tracts

Texture mapping was applied to GPU-generated streamtubes, as discussed in greater detail in Section 6, in order to visualize the index with an anatomical and clinical meaning. The presented streamtubes are computed using a shader-based pipeline: View vector oriented triangle strips are generated in the geometry shader and colored tube-like in the fragment shader. More precisely, the distance of a fragment from the tube's centerline is transferred from the geometry shader to the fragment shader and used to fade the fragment's color to black. Hence, a tube-like appearance is achieved without the computational complexity of real tubes. The *ISMI* classification volume is provided through a 3D texture and the fragment shader performs a texture lookup as well as a subsequent color mapping.

Fiber pathways resulting from the distance-based HARDI tractography algorithm, as discussed in detail in Section 5, were used for tract generation. The deterministic approach is based on the local ODF and includes an evaluation of diffusion distributions in the seed voxel as well as an evaluation of distances to white matter boundaries. In the proposed algorithm, curvature thresholds, local anisotropy information, and the position of the current tract within the bundle are used to determine the direction for the next step in each voxel using the ODF.

4.6.3 Results

Results of the *ISMI* were compared to the well-known GFA diffusion index. Fibers of the Fiber Cup phantom dataset were computed in order to identify challenging regions and evaluate the proposed method. Figure 4.6a shows the

result using the GFA anisotropy index. Yellow indicates a high GFA-value and
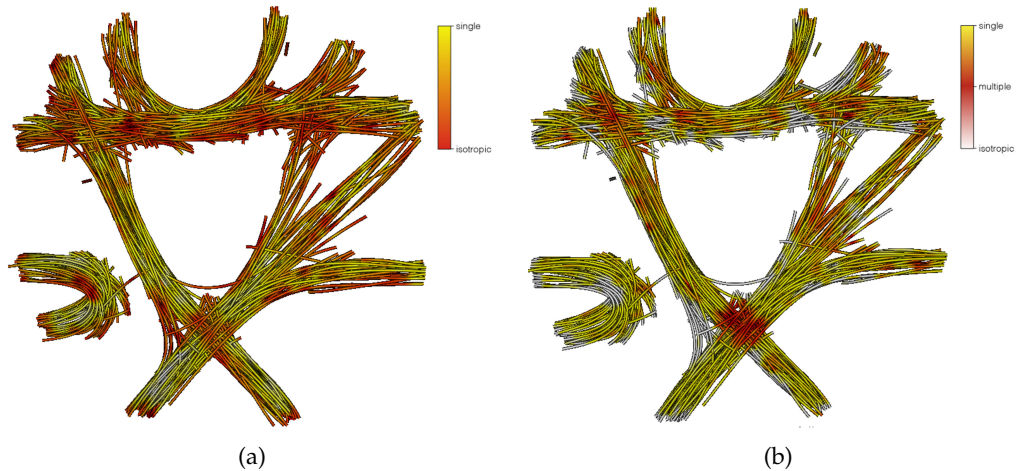
Figure 4.6: Visualization of anisotropy index results: GFA does not clearly differentiate between multiple fiber populations and isotropic regions (4.6a). Classification results of *ISMI*, however, lead to accurate discriminations (4.6b).

hence high anisotropy, whereas red reveals isotropic regions with a low GFA-value. Using this index, regions with complex intra-voxel diffusion profiles lead to a low anisotropy value. Considering regions where trajectories leak into gray matter, as one can see in Figure 4.6a in the left of the crossing at the bottom, leakings are not differentiated from crossings. As a consequence, GFA is unable to distinguish between regions with isotropic diffusion (gray matter) and multiple diffusion orientations (white matter). On the other hand, the *ISMI* classification results of the same fiber representation is shown in Figure 4.6. The presented index successfully classifies into the three intra-voxel configurations: isotropic diffusion (white), single fiber population (yellow), and multiple fiber population (red). In crossing and fanning areas *ISMI* has a high value, indicating multiple fiber configurations, whereas the leaking of the trajectory leads to a low value. Comparing both results, one can detect false-positives, identified by GFA in regions comprising gray matter or high curvature. Contrary, *ISMI* is able to differentiate between isotropic diffusion and multiple fiber populations.

A similar coloring was applied to provide a comparison between *ISMI* and MFC: Black indicates no fiber; gray, a single fiber; and white, a multiple fiber population. *ISMI* results in an output in the range of [0,1], as displayed in Figure 4.7a. This classification was thresholded in order to obtain a distinct separation. The applied thresholds were 0.024, to define white matter in general, and 0.432, to further separate the white matter into single an multiple fiber populations. Results are shown in Figure 4.7b. One can observe that the classification result is noisier than the MFC result. This is caused by the fact, that the MFC is a morphological approach, featuring global structures. Contrarily, *ISMI* considers the ODF of each voxel independently and is as a result, more susceptible to noise. However, *ISMI* performs better than the state of the art classifiers previously introduced. Both *ISMI* as well as MFC have their advantages which are discussed in the following.

(a)   (b)
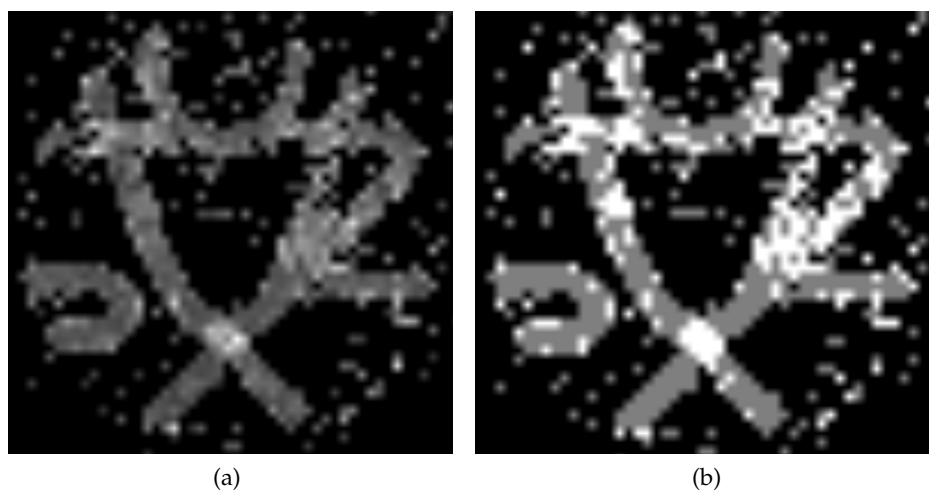
Figure 4.7: *ISMI* classification result for the hardware phantom: *ISMI* in the range from [0,1] (4.7a). Distinct voxel classification is achieved by thresholding (4.7b).

Figure 4.8 shows fibers belonging to the CC and running in the *centrum semio-vale*. The anatomical volume is visualized for spatial orientation. In Figure 4.8, red fiber parts indicate voxels with multiple ODF magnitudes and hence, voxels which are crossed by further pathways. In both, the right and the left of the illustrated fibers, these sections belong to the *centrum semiovale*. Whereas, the
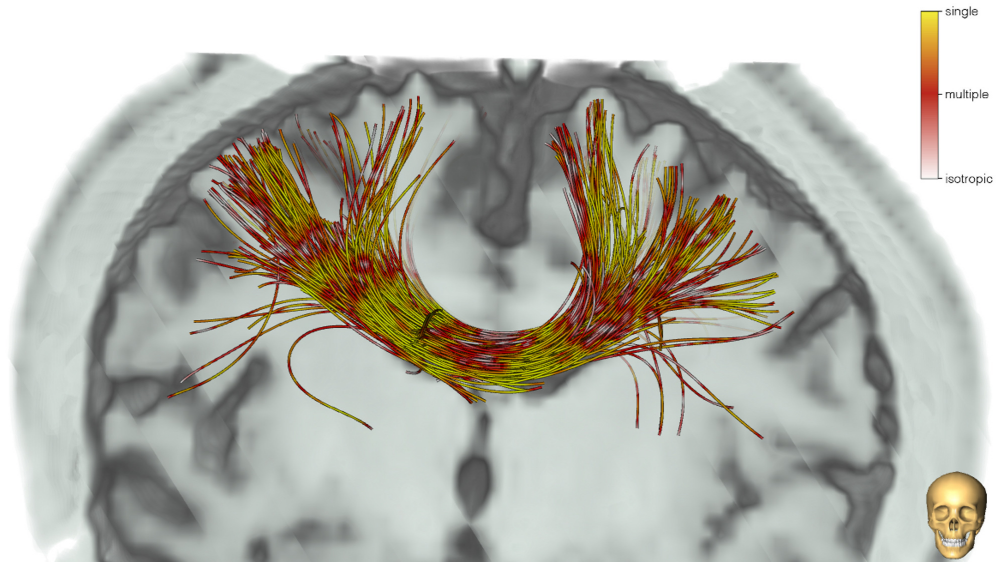
Figure 4.8: *ISMI* classification results for human brain pathways: *ISMI* successfully classifies callosal fibers running in the *centrum semiovale*.

red parts in the center of the CC reveal regions where the *cingulum* and the CC meet. The *cingulum* is a pathway that runs along the top of the CC and in the opposite direction.

In order to illustrate the classification power in terms of isotropic diffusion, Figure 4.9 shows parts of the CC that have been reconstructed with a tractography approach which only takes the maximum value of the ODF as a tracking direction. Several issues can be observed from the results. First, the simple algorithm is not able to reconstruct challenging fiber configurations properly: in this case the fanning of the CC. Second, a seed region within gray matter was placed to indicate false positives, as can be seen below the center of the CC. Fibers in this region are displayed white. One can estimate that fibers running inferiorly are also white which indicates isotropic diffusion. These parts of the reconstructed neuronal pathways run into gray matter areas or show a very low anisotropy. The results correspond with knowledge about diffusion imaging in fibers close to the head's surface.
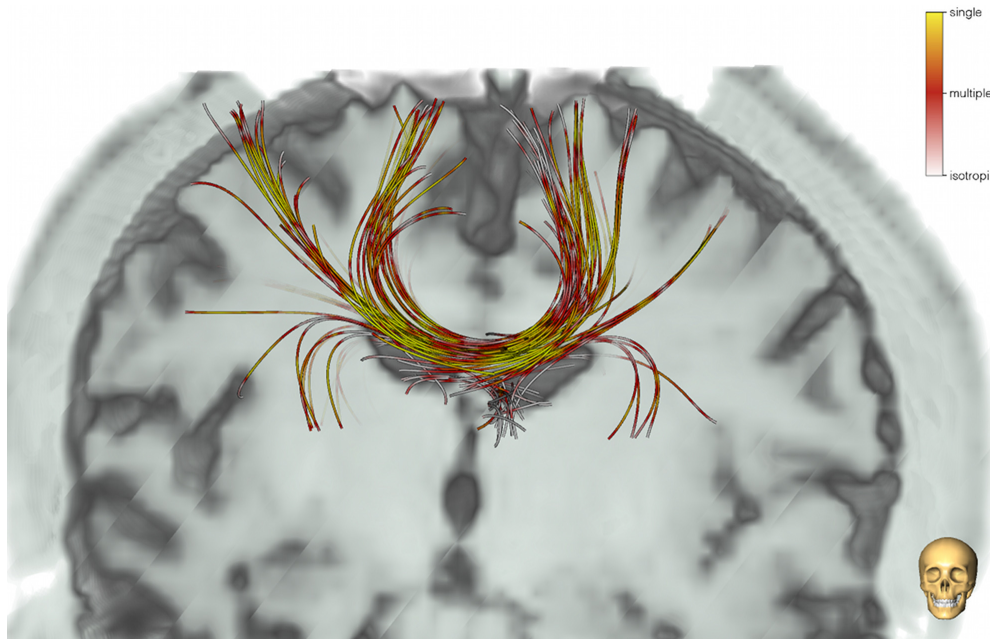
Figure 4.9: *ISMI* classification results for human brain pathways: *ISMI* successfully defines regions with isotropic diffusion.

4.7 Discussion

Two indices for diffusion profile classification using HARDI were proposed in this chapter. Results have shown that both, *MFC* and *ISMI*, successfully differentiate isotropic and anisotropic diffusion. Furthermore, they perform better in terms of discriminating diffusion in the two compartments single and multiple fiber orientation than known classifiers.

MFC is a global approach, using the morphology of white matter bundles to estimate regions of interest: regions where multiple maxima are most likely. The approach utilizes a previously defined white matter mask on which the classification power strongly depends. Phantom data led to promising results. In terms of human brain data, the kernel size of the morphological operations may have to be adjusted depending on the fiber thickness in question as well as the underlying voxel size.

On the other hand, *ISMI* is a local classifier which only takes the diffusion probability function, the ODF, of a single voxel into account. It uses a thresholding pipeline in order to classify each voxel into one of the stated compartments. Contrary to known classifiers, such as the GFA, *ISMI* additionally provides the ability to control the output in terms of the multiple fiber configurations in question. By adjusting the threshold for the number of ODF maxima within the *ISMI* pipeline, the user influences the result with direct visual feedback. In addition, a subsequent fiber integrity examination for single fiber distributions is feasible: using a colormap which only considers the index range of single diffusion profiles enables an estimation focused on the degree of integrity.

Evaluations with state of the art diffusion classifiers prove the classification power of *MFC* as well as *ISMI*. If one compares both classifiers, *ISMI* is related to the diffusion profile and is more detailed. However, it leads to more overall noise since the compartment is independently defined for each voxel without considering neighboring voxels. On the other hand, while the *MFC* is not sensitive to local noise, it is not as precise as the *ISMI* for an individual voxel. As a result, the most appropriate index depends on the question to be answered.

In future, it will be interesting to observe the diffusion constitutions of neighboring voxels in order to infer the current diffusion profile. For example, whether adjacent voxels support a local crossing or fanning configuration influences the probability of certain ODF directions.

Diffusion indices aim to reduce the probability diffusion function in order to obtain a meaningful representation. However, without an appropriate visualization their interpretation as well as exploration is time consuming and cumbersome. Both indices discussed in this chapter, form the basis for several subsequent visualizations which are introduced in the remaining parts of this thesis.

In addition, diffusion classifiers support fiber reconstructions in terms of propagation decisions. For example, if a single fiber distribution is present, a simple integration step in the direction of the maximum ODF radius is sufficient. However, if multiple diffusion directions are present and no trajectory splitting is allowed, more advanced heuristics are needed to define the direction for the next

step. Using knowledge of intra-voxel fiber constellations will be used in the following for decision making concerning propagation direction for tractography.

An interesting aspect is to examine the presented diffusion indices in order to answer the question of tumor infiltration location for neurosurgical planning. Using DTI, it is not possible to distinguish between voxels containing complex fiber distributions, such as crossings, and voxels containing no white matter at all. In addition, it is reported that tumor tissue interferes with local diffusion of water molecules or, put more precisely, causes isotropic diffusion. Therefore, the next challenge is to estimate whether the presented diffusion indices are able to differentiate complex fiber distributions, isotropic diffusion, and diffusion profiles resulting from tumor infiltration. Preoperative knowledge about tract integrity poses a real benefit for neurosurgical planning: The surgeon is able to determine the resection extent with respect to infiltrated white matter. However, the presented indices require HARDI acquisitions in order to assure reliable ODF evaluation. The recruiting of tumor patients for HARDI acquisitions is challenging due to the long acquisition time and not yet evaluated MRI parameters. For this reason, no evaluation could be performed with tumor patients.

Part III

Neuronal pathway reconstruction

5 Tractography

5.1 Overview

HARDI techniques enable a more precise approximation of the underlying diffusion process. However, advanced fiber reconstruction techniques are required in order to evaluate the contribution of HARDI to neuroscience. The knowledge of previously introduced diffusion indices is beneficial to reconstruct challenging neuronal pathways. To begin this chapter, issues of how HARDI affects neuronal pathway reconstructions are presented in Section 5.2, followed by a survey on tractography approaches in Section 5.3. The developed HARDI-based fiber reconstruction approach, published in [100], is presented in Section 5.4, the results in Section 5.5, and a discussion of the results in Section 5.6.

5.2 Introduction

Major commisural fiber pathways of human white matter include the CC and the anterior *commissures*. The latter connect both cerebral hemispheres, as explained in Section 2.4. It is not possible to reconstruct all white matter fibers using DTI-based tractography algorithms: only the most medial commisural projections, fibers running from the center near the middle line of the brain, are detectable. Connections fanning into the hemispheres, the anterior commissure fibers, can not be reconstructed using DTI [45]. Despite these limitations, DTI-based tractography is commonly used in clinical environments. This is due to its fast acquisition and reconstruction time. As a result, vital clinical examinations currently consider incomplete neuronal pathways and erroneous fiber courses. This is where advanced diffusion techniques make a contribution: HARDI acquisitions followed by a subsequent innovative tractography algorithm, pro-

vide more reliable visualizations. The following scientific questions guide the design of a HARDI tractography approach:

- How can HARDI-based indices contribute to tractography approaches?

- How can integration errors due to noise in the ODF be minimized?

- How can global information, such fiber constellations, be integrated in a tractography approach?

- Is it possible to detect challenging fiber pathways, such as the commissural fibers, with greater detail?

Due to the Gaussian model of DTI techniques it is not possible to resolve more than one diffusion direction properly. In voxels containing multiple fiber orientations this leads to low anisotropy values. In this case, conventional DTI tractography algorithms either stop or reconstruct false pathways. This is the reason why researchers as well as clinicians are skeptical about tractography results using DTI and the uncertainty of the principal diffusion direction became a big issue. Tractography techniques benefit from the detailed information provided by the ODF. However, multiple fiber populations in one voxel lead to more than one maximum and hence require more sophisticated approaches. Using algorithms designed for one diffusion direction, similar to DTI-based approaches, would waste the additional information. Several challenging regions in the human brain require the higher order reconstruction scheme. One of these complex human brain networks is the *centrum semiovale*, where three main neuronal pathways cross. Furthermore, the fanning of the CC constitutes a challenging configuration for tractography approaches.

The initial direction in the presented tractography approach is estimated with respect to white matter boundaries. Distance calculations aim to incorporate global knowledge about the fiber course. They are applied since streamline approaches easily suffer from integration errors. In addition, information of previously introduced classifiers, a differentiation between voxels containing single or multiple fiber orientations, is used to guide tractography in challenging pathway configurations. Contrary to other HARDI-based approaches, the presented fiber reconstruction does not split in regions with multiple ODF maxima.

Instead, the most appropriate propagation direction for the current tract is determined. This leads to fiber tracts which are directly assigned to the provided seeds without the reconstruction of unwanted tracts. The approach features a restoration of propagation paths to prevent the leaking from white matter. In addition, a propagation estimation with respect to initial white matter borders is integrated in order to ensure tractography within specific bundles. Therefore, trajectories are computed, taking the seed points' placement within white matter tracts into account.

5.3 Related work

One of the earliest visualization techniques of diffusion data was the three-dimensional reconstruction of white matter fibers using tractography algorithms. Deterministic tractography approaches use streamline algorithms and begin with DTI data [5, 68, 131]. Trajectories are reconstructed by following the principal diffusion direction (PDD) from a starting point through the volume. In DTI cases, the eigenvector with the highest eigenvalue is considered to be the PDD. Further methods were introduced using the entire diffusion tensor to deflect a fiber path. They are called tensorline tracking or tensor deflection (TEND) [57, 126].

Fiber tracking approaches using HARDI data are advantageous over DTI-based approaches in regions where multiple intra-voxel populations exist. The Fiber Cup [2], which was held within the scope of the MICCAI conference in 2009, targeted the field of tractography methods for diffusion imaging. The contest demonstrated that complex white matter configurations are still challenging for common tracking algorithms. A streamline method for DSI was presented by Wedeen et al. [124]. ODF directions which point to a local maximum and form the least curvature with the incoming direction were applied for fiber tracking in this simple approach. A method using CSD and local diffusion maxima was introduced by Jeurissen et al. [42] and placed 2nd at the Fiber Cup 2009. The sharp ODFs which result from the CSD approach, lead to successfully reconstructed fibers. However, a voxel determining the decon-

volution kernel representing the diffusion of a single fiber population had to be manually selected. The fiber assignment by continuous tracking (FACT) algorithm [68] was adapted to HARDI data by Chao et al. [18] to become the multiple FACT (MFACT) method. Originally, FACT used DTI data and a continuous tracking along the vector field, formed by the eigenvectors of each voxel. The entry to the next voxel is defined by the local eigenvector. In the case of HARDI data, every direction indicated by a local diffusion maximum above a user defined threshold and below a curvature threshold is followed through the volume. Apparently, tractography results strongly depend on the accurateness of the input, in this case the reconstructed ODF. The mentioned approaches are very simple and lead to sufficient results caused by a sharpened diffusion signal. However, reconstruction issues, as discussed in Section 3.6.2, argue against these methods. A flow-based algorithm using QBI was introduced by Campbell et al. [17]. The authors proposed a speed function for DTI, HARDI or a hybrid approach. Flow-based approaches are considered as global tracking approaches in which DTI eigenvectors or ODF maxima form a vector field for surface evolution. A speed function is used to further control the propagation. Despite the fact that global approaches usually perform well, their application to everyday examinations is challenging since they enlarge the computation time to an extent which is not clinically feasible. A further global tract reconstruction approach, proposed by Reisert et al. [89, 90], won first place in the Fiber Cup. The presented local energy minimization algorithm achieved good results by positioning particles comprising a position, orientation, and an internal energy. Furthermore the method applied external energies to match the overall fiber courses. Despite the low computation time mentioned by the authors, the timings of global approaches are much higher compared to deterministic approaches. Descoteaux et al. [23] implemented a simple approach for QBI based on their previously introduced HARDI reconstruction. The authors suggested a streamline splitting in regions with multiple ODF maxima. Despite the fact that generating new streamlines is intuitive yet simple to implement, the meaning of the additional streamlines is not clear: If a single seed point is provided by a clinician, a specific fiber course is in question. Further streamlines are misleading and cause additional visual clutter. More recently, Goh [34] introduced a

variation of deterministic methods and won the 4th place at the 2009 Fiber Cup. Instead of sharpening the ODF with SD, the reconstruction was performed with consideration of the solid angle [3]. The solid angle method takes the quadric growth of the volume element for each ODF sampling direction and its distance to the origin into account. The ODF is sharpened since tracking directions are altered with respect to local ODF maxima and the incoming direction. This approach makes a first step towards ODF evaluation. Savadjiev et al. [104] applied a voxel labeling to tractography. The authors were able to distinguish between single fiber distributions as well as fanning and crossing configurations using a 3D curve inference method. Tractography approaches using this information lead to great success.

5.4 Distance-based deterministic tractography

In the following, a novel tract reconstruction algorithm based on distance calculations between the borders of fiber bundles is proposed. The algorithm requires a list of seed voxels as input; as output, it provides a continuous list of coordinates resulting from bidirectional fiber tracking starting at each individual seed point. The basic idea of this algorithm is to follow pathways while maintaining the distance ratio to white matter borders which is present at the seed point. Ideally, this method results in reconstructed pathways which are parallel to fiber borders. In complex fiber structures which are voxels with multiple fiber populations, the result obtained is the trajectory which best matches the current course of the fiber bundle. This tract is determined by additionally taking into account the average curvature angle between the PDD in the last processed voxels. The tracking procedure is stopped when the fiber trajectory proceeds through an area of isotropic diffusion. Furthermore, propagation is aborted when the reconstruction procedure returns a state which indicates an invalid position. This occurs when the tracking leaves the dataset or the fiber curvature angle is above the specified threshold. Figure 5.1 provides a general overview of the algorithm. The individual steps of the developed fiber tractography algorithm are described in the following sections.
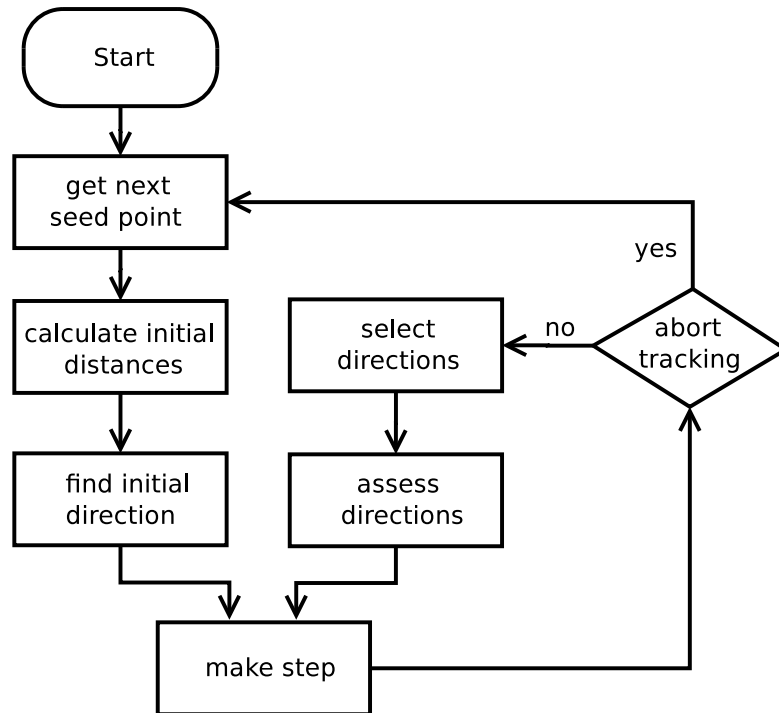
Figure 5.1: Tractography algorithm overview: Individual steps of the proposed distance based fiber tracking approach are illustrated.

5.4.1 Voxel classification

Voxel classification provides vital information about intra-voxel diffusion profiles. Index information is used in the proposed tractography method in order to identify white and gray matter as well as apply a more advanced propagation estimation in cases of complex diffusion distributions. In this case, the *MFC* approach, explained in Section 4.5, was utilized since it provides a good global approximation of white and gray matter as well as single and multiple intra-voxel fiber configurations. Furthermore, it does not incorporate as much noise as the *ISMI*, proposed in Section 4.6.

5.4.2 Determining initial configurations

The first step in propagation is the definition of an initial tracking direction and initial distances to fiber borders. Ideally, tracking starts parallel to fiber borders. As this is rarely the case when using the PDD as the starting direction, another strategy is applied to find the initial tracking direction in the seed voxels: First, only directions which belong to a local ODF maximum are considered as candidate directions for tract propagation. In the next step, distances to fiber borders are calculated for the obtained directions along with their averages: Orthogonal vectors with equal angular separation to one another are computed for each candidate direction, as illustrated in Figure 5.2. Along each of these orthogonal
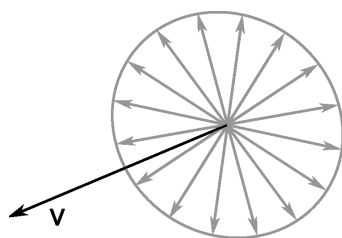
Figure 5.2: Distance vector setup: The black arrow represents the tracking direction **v**. At each step, the distance to the fiber borders is measured along the coplanar vectors which are orthogonal to **v**.

vectors, the distance to the fiber border is calculated. The fiber border is reached when:

1. A gray matter voxel is entered or

2. the angle between **v** and the PDD of a voxel crossed by one of the distance vectors is greater than a specified maximum curvature for single fiber population.

The second condition accounts for areas comprising several fiber bundles and allows for almost constant fiber widths, also in regions with complicated white matter structures. Figure 5.3 illustrates examples for distance calculations in different voxels. The direction with the smallest maximum value, as displayed in Figure 5.4, is considered as most parallel to the fiber borders and is thus
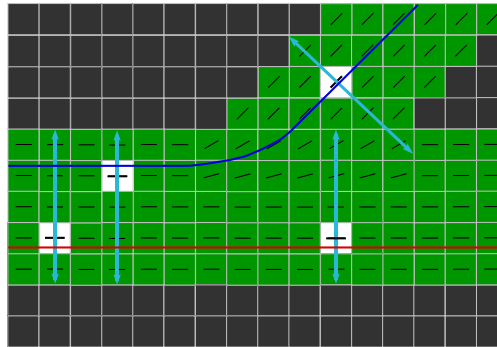
Figure 5.3: Conceptual illustration of the distance calculation: White matter voxels are shown in green with their individual PDDs. Exemplary distance calculations are shown for voxels marked white. The distance calculation for both white voxels on the left stops at the fiber borders when reaching gray matter voxels. The calculation for the two right voxels also stops when reaching a voxel with a PDD above a specified angle to the current direction. The resulting distances are indicated by the cyan arrows. Example fiber trajectories are shown in blue and red.

used as the initial direction for fiber tract reconstruction. The fiber trajectory is advanced one step along this direction using Euler integration.

5.4.3 Selecting directions

In the following step, possible directions to continue the reconstruction need to be found at the new position. At this point, two different strategies are applied depending on the type of diffusion present in the current voxel. The current direction and all ODF directions assigned to a local ODF maximum are considered in white matter voxels. Each of these directions is tested and added to a list of candidate directions if the two following conditions are met:

1. One step in this direction leads to a position still inside the dataset and

2. the angle between the current direction and the tested direction is below a threshold.

Different angular thresholds are used for single and multiple fiber populations, respectively. The fiber trajectory can enter voxels with isotropic diffusion at po-
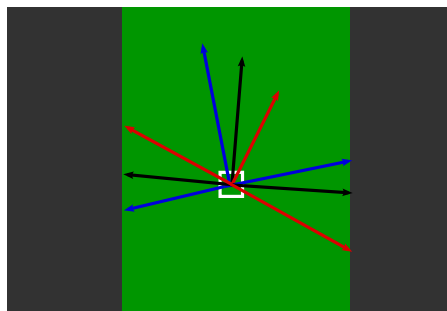
Figure 5.4: Calculation of the initial tracking direction for the voxel indicated by the white box: Green illustrates white matter. The three vectors pointing to the top identify candidate directions for tract reconstruction; their lengths represent the respective ODF value. Instead of choosing the vector with the highest ODF value (blue) the black vector is used as an initial tracking direction. This is due to the fact that it leads to the smallest maximum distance value which is computed from the length of its corresponding orthogonal vectors.

sitions close to the border or in white matter mask gaps. In these cases the aim is to return the trajectory to white matter voxels. For this purpose, direction vectors are generated which form an angle of 45 degrees with the current direction. Subsequently, it is tested whether one step in the current direction or along one of the 45 degree vectors leads to white matter. Every direction vector reaching white matter after one step is added to the list of candidate directions. The test is performed again with double then quadruple step sizes in the case no sufficient vector is determined. Finally, tract reconstruction is aborted if no propagation direction is found.

5.4.4 Assessing directions

Of all the candidate directions, one needs to be selected to continue the fiber trajectory. To accomplish this task, distances for every direction are calculated, as described in Section 5.4.2. Subsequently, the resulting distances are grouped into pairs of opposite distance vectors and sorted according to the sum of the pairs. One needs to know which two distance vectors correspond to each other in order to compare the distances at the new position to the initial distances.

Unfortunately, there is no way to do so as it would imply assigning descriptors like up, down, left, and right to arbitrary vectors in 3D space. However, assuming that the fiber width does not change much along the fiber, the pairs of the initial and current distances are sorted. In the sorted list, two adjacent values, d_i and d_{i+1} with $d_i \leq d_{i+1}$ and even i, indicate distance values for two opposite vectors. It is assumed that the distance pairs at the same position in both lists correspond to each other. The deviation, D, from the initial distances is calculated for each candidate fiber direction $\mathbf{w}$, as

$$D(\mathbf{w}) = \sqrt{\sum_{j=0}^{k} \left(\left(\frac{\delta_{2j}}{\delta_{2j} + \delta_{2j+1}} \right) - \left(\frac{d_{2j}}{d_{2j} + d_{2j+1}} \right) \right)^2}, \qquad (5.1)$$

where δ is the initial distance determined in the seed voxel and d is the distance found in the current voxel. The sum is calculated over distance pairs j, where $k = numDistVec/2 - 1$. The direction vector $\mathbf{w}$, with the smallest value D is considered to best match the initial distances.

In voxels with multiple fiber populations, the direction vector best resembling the initial distances might not be the optimal choice to continue fiber reconstruction, as illustrated in Figure 5.5. This is the case when the seed point was located significantly closer to one fiber border than the other. Such a trajectory follows the closer fiber border and, consequently, is not able to propagate through a fiber crossing region. In order to handle this case correctly, the distance to the
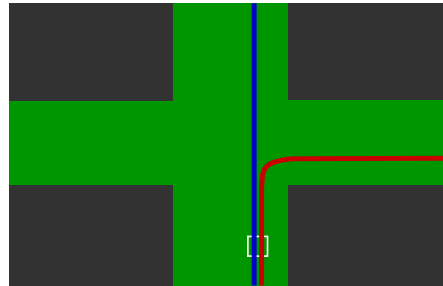
Figure 5.5: Propagation through crossing areas: The red streamline is not able to propagate through the crossing area as it follows the direction with optimal distance values. In contrast to this, the blue streamline follows the most plausible fiber tract, ignoring the optimal distance direction.

next gray matter voxel from the current position along each of the candidate directions is calculated. The direction is maintained if this distance is at least twice the step size otherwise removed.

In the next step, the angle between the current direction and each remaining direction is calculated and compared to the *curvature hint angle*. The *curvature hint angle* is computed as the average angle between two consecutive PDDs of the respective tract. The direction which best matches the curvature hint angle is chosen. Finally, the obtained direction is interpolated with the current direction using a weighting factor and the result is used for streamline propagation.

5.4.5 Visualization

Streamlines start from either the center of a seed voxel or nine uniformly distributed coordinates in a voxel. The resulting trajectory of each bidirectionally tracked fiber is interpolated using a b-spline approach to obtain a smooth curve. Fiber pathways are visualized using either illuminated streamlines or streamtubes. Streamtubes are composed of view-dependent and color coded quads and are presented in greater detail in Section 6.

5.5 Results

In the following, the results of the distance-based tractography approach are presented using the previously introduced phantom and human brain diffusion dataset.

5.5.1 Phantom data

The first evaluation of the proposed algorithm was performed on a phantom dataset which comprises most challenging fiber configurations such as crossing, kissing, and fanning. Streamlines were reconstructed using one seed point in the voxel's center. The results are shown in Figure 5.6b. Parameters were carefully evaluated, performing the best overall reconstruction results. Most of the reconstructed fiber trajectories matched the provided ground truth, as
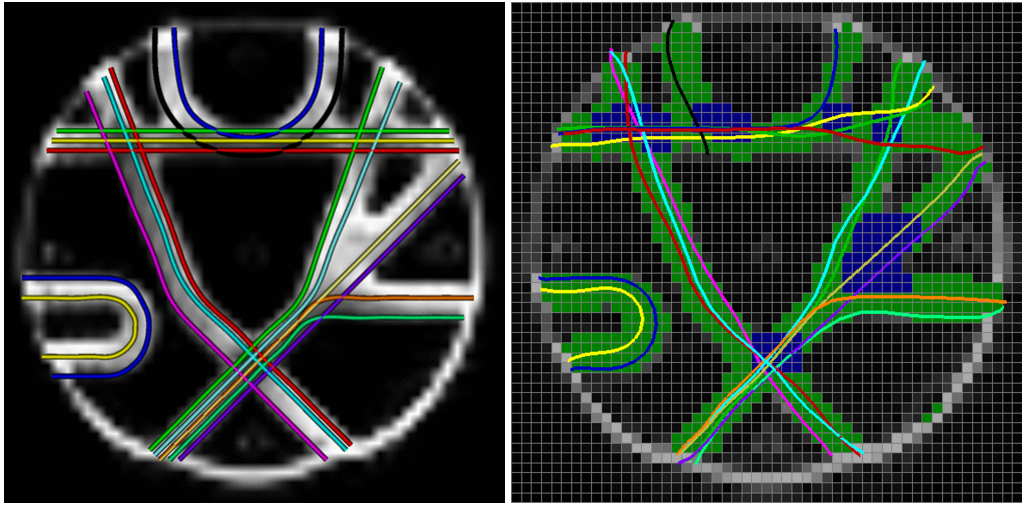
Figure 5.6: Tractography phantom results: Ground truth of the phantom dataset (5.6a) and tractography results with the proposed algorithm (5.6b). Green regions indicate single fiber and blue regions multiple fiber configurations.

illustrated in Figure 5.6a. Crossings at different angles were reconstructed correctly as well as the fiber branching area and fiber courses with high curvature. However, the fiber kissing configuration in the upper part of the phantom could not be reconstructed correctly. This type of white matter structure is similar to fiber crossings at a low angle. Unlike within crossing areas, it is not possible to limit the range of possible directions to a small angular value and propagate the trajectory in one of the remaining directions: The fiber has to bend constantly inside multiple fiber areas in regions with kissing configurations. On the other hand, the required parameter setting would not be able to resolve fiber crossings properly, instead it would follow a wrong fiber bundle. The conflict of bending and straight propagation makes fiber kissing regions most challenging.

The scores for the reconstructed fiber pathways were calculated using the evaluation application provided at the Fiber Cup website. This application computes the $L2$ metric in order to compare a reconstructed fiber with the ground truth fiber pathway. It was used to evaluate submissions for the Fiber Cup, as well as enable future tractography evaluation using the same phantom

data. Our presented approach would have achieved the third place in the total ranking at the Fiber Cup contest in 2009.

5.5.2 Human brain data

Figure 5.7c shows the tracking results of the CC and the *MFC* output with superimposed ODF glyph representation. An anatomical reference is displayed in Figure 5.7a and the color coded PDD in Figure 5.7b. Seed points were placed at the center of the CC. Observations prove that the fanning of the CC and the commissural fibers are successfully reconstructed. The applied standard devia-

(a)   (b)   (c)
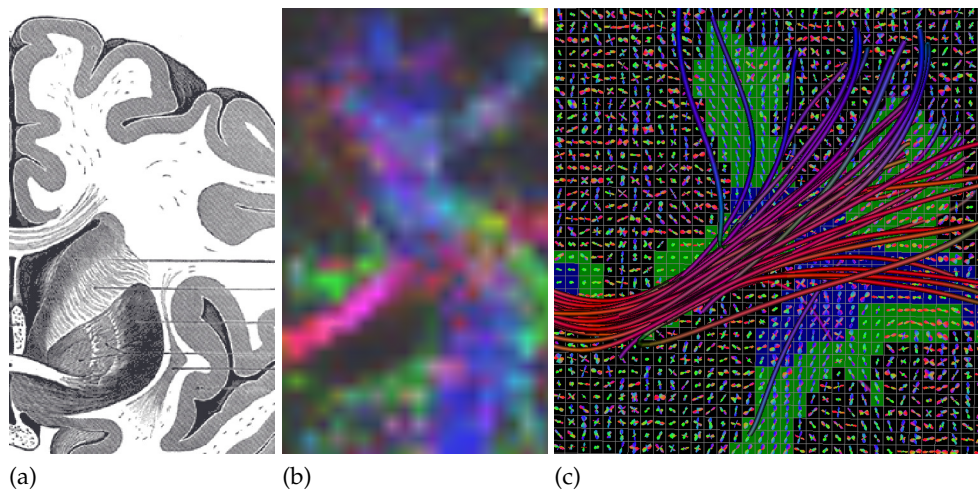
Figure 5.7: Results of the distance-based tractography approach for the *centrum semio-vale*: Illustration of the region under consideration in a coronal slice (5.7a), image adapted from Grey's Anatomy [36], and a directional color coding of the same region (5.7b). Tractography results of callosal fibers are shown in combination with white matter labeling (single fiber distributions are represented in green and multiple distributions in blue) and superimposed ODF glyphs (5.7c).

tion threshold for the *MFC* approach was 115.

An algorithm using the maximum diffusion direction per voxel and Euler integration was implemented for comparison, results are shown in Figure 5.8. One can observe that this approach is unable to properly reconstruct the com-

misural projections of the CC. This inability results from the competing diffusion directions of the ODF.
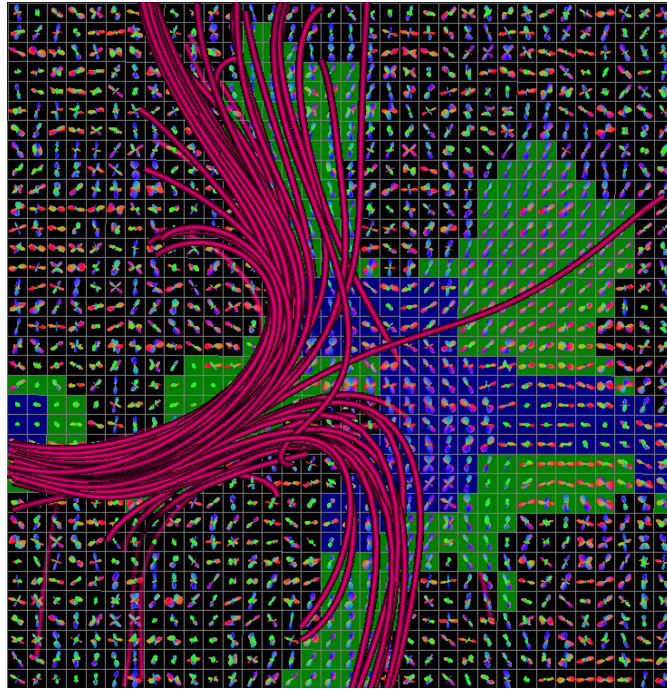
Figure 5.8: Results of the simple tractography approach for the *centrum semiovale*: Commissural fibers of the CC are not sufficiently reconstructed.

In addition, the proposed method was evaluated in the region of the *centrum semiovale*, where known crossings of the CC, the CST, and the SLF exist, as illustrated in Figure 5.9. In Figure 5.10 the tractography of the CST is highlighted in blue, the CC in red, and the SLF in green. The crossing of commissural fibers of the CC through the CST is observed. Results were discussed informally with our clinical partners who judged them as consistent with anatomical knowledge. The known callosal fannings were reconstructed successfully with the proposed algorithm. Performance evaluation was accomplished on a Core2 Duo, 3.16 GHz with 4 GB RAM and a NVIDIA GeForce GTX 285 graphics card. A region of interest covering the *centrum semiovale* in both hemispheres in the human brain dataset was chosen with a size of $48 \times 44 \times 38$ voxels. ODF
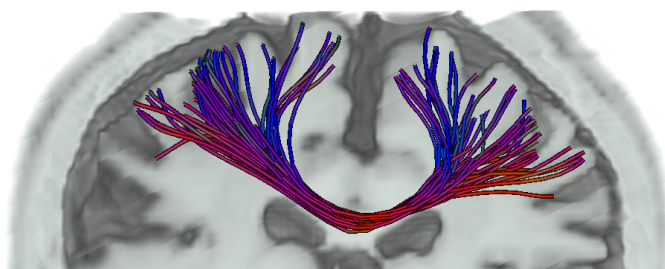
Figure 5.9: Tracking results of fibers belonging to the CC in the *centrum semiovale*: An anatomical volume is indluded for spatial background information. The fanning of callosal fibers into both hemispheres is successfully resolved.

computation took four minutes, anisotropy criteria calculation one minute, and tractography an average of one second for each streamline.

5.6 Discussion

In this chapter, a novel deterministic tractography method for HARDI data was proposed. The presented approach considers multiple intra-voxel diffusion maxima for propagation. Furthermore, an evaluation of the initial tracking direction, and information about white matter boundaries as well as a recovery approach which guides tracking back to white matter are incorporated. Contrary to initial methods, using HARDI data and multiple diffusion directions, the trajectory does not split in voxels with more than one ODF maximum. Instead, the spherical probability function is evaluated and the most appropriate direction for the next step is determined based on local and global features. An evaluation of ODF maxima based on global tract characteristics such as curvature is reasonable since ODFs are often blurred. Furthermore, depending on the angular sampling, interpolation errors result in false tract reconstruction. Propagation vector evaluation is advantageous over propagation splitting since specific fiber tracts directly assigned to provided seed points are desired in clinical questions.

The presented approach aims to keep trajectories in certain white matter pathways by maintaining the ratio within fiber bundles and return to white matter
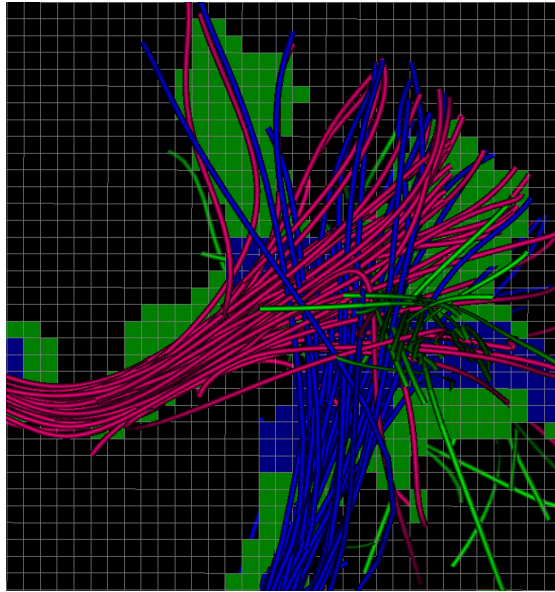
Figure 5.10: Crossing results of the CC, the SLF, and the CST in the *centrum semiovale*: The CC is shown in red, the CST in blue, and the SLF in green. The crossing of commissural fibers is successfully reconstructed.

in isotropic regions. This does not always reflect the intra-voxel fiber population but instead approximates global tract progression. However, based on the fact that the ODF reflects an approximation of intra-voxel fiber orientations, tractography results only provide an estimation of certain neuronal pathways and have to be considered as bundles. Therefore, a supplementary fiber clustering is reasonable and justifies our method.

The approach was evaluated using a phantom and a human brain dataset in order to prove its reconstruction power in challenging regions. The results showed that information about intra-voxel diffusion distributions support tract reconstruction when multiple intra-voxel diffusion profiles are present. First, knowledge about white matter regions is vital. The presented approach keeps the trajectory within the white matter mask by adjusting propagation directions in a way that the directions which most probably lead to white matter voxels are chosen. Second, propagation is successfully guided through fiber crossings using *MFC* results: the identification of a underlying complex fiber distribution.

In this case, propagation considers the global properties of the current tract, the curvature.

In addition, the approach performs an evaluation of ODF maxima according to certain trajectory characteristics such as average tract direction. This is beneficial since the propagation is more robust to local noise or weak ODF angular resolution. Furthermore, integration errors are minimized. Thereby, assumptions about the tract course are incorporated however affirmed by the results.

Summarizing, this chapter showed that adjusting tract reconstruction methods to consider HARDI data as well as preprocessing data using HARDI classifiers has great potential. The results of advanced tract reconstructions are beneficial for fundamental neuroscience to identify small tracts or more intricate white matter networks. In the case of neurosurgical planning, HARDI tractography provides a real benefit since more complex diffusion profiles are obtained and the tractography results are more precise. Additionally, white matter infiltrations could be distinguished from simple displacements. However, HARDI acquisitions with tumor patients require further investigation in terms of MRI parameter settings as well as reconstruction algorithms.

Since the morphological approach for voxel classification only differentiates single from multiple fiber populations, it is interesting to include more advanced methods to estimate the true intra-voxel fiber configuration and thereby distinguish fiber crossings, kissings, and fannings. Global fiber configurations can contribute to identify local fiber distributions. For instance, using a local fiber geometry for voxel classification [104]. Probabilistic tractography methods incorporate the uncertainty of the diffusion orientation. Example algorithms using HARDI include the application of the residual bootstrap [9] and a Bayesian approach [8]. Additionally, tractography is recently performed using a particle-based approach [23, 76]. An evaluation of heuristics using a probabilistic or stochastic approach has potential to resolve the missing fiber constellations.

Part IV

Diffusion data visualization

6 Advanced fiber rendering

6.1 Overview

As introduced in the previous chapter, diffusion imaging enables the examination of the brain's white matter network in vivo and thereby poses a huge contribution to neuroscience. Diffusion indices are able to characterize information about the intrinsic fiber integrity as well as intra-voxel fiber constellations. Furthermore, fiber reconstruction techniques provide the unique possibility of identifying the course and spatial position of neuronal pathways. Thus, the next issue for diffusion imaging is the combination of this information within one visual representation. In the following, guiding scientific questions for line visualization are presented in Section 6.2, literature related to line visualization in Section 6.3, and enhanced line rendering approaches for diffusion data based on the publication in [93] in Section 6.4. Section 6.5 presents the results and Section 6.6 the discussion of the approaches.

6.2 Introduction

In both cases, DTI as well as HARDI, tractography approaches result in a large amount of lines approximating the white matter network. Conventional tract visualizations often appear visually cluttered and are neither intuitive nor easy to interpret. Considering HARDI-based tractography results, visualizations are even more complex than DTI-based results since several neuronal pathways can run within one voxel. Therefore, the challenge is to generate intuitive, task-oriented line visualizations facilitating a spatial as well as functional interpretation of the data.

The scientific questions guiding diffusion line visualizations are:

- What are interesting features for lines representing neuronal pathways?

- How can HARDI-based diffusion information be visualized?

- How can the visual clutter be reduced?

- How can the spatial understanding of line sets be enhanced?

The presented approaches are considered as a constitutive step to techniques presented in previous chapters: Subsequent to the definition of HARDI-specific characteristics and tract reconstruction, line visualizations are the first and most common visualization of diffusion MRI data. However, due to the overwhelming amount of lines present in a large seeding region or a major fiber tract, line representations suffer from visual cluttering and low spatial understanding.

The introduced visualization approaches combine existing renderings and focus on enhancing spatial depth perception of HARDI-based fiber reconstructions. Illustrative rendering methods, such as depth-dependent halos and ambient occlusion, were combined with the visualization of crucial tract information such as the direction and integrity of fiber representations. For more details concerning renderings, the reader is referred to the original publications.

6.3 Related work

Line rendering techniques, such as streamlines and streamtubes, originate from flow visualization [32, 78, 127]. A huge amount of lines is observed in most of the cases for both flow as well as fiber visualization. For this reason, representations are cluttered and understanding the spatial arrangement of lines is difficult. Several approaches arose aiming at providing more intuitive representations. For example, the perception of tubes is advantageous over simple line representations due to their 3D geometry. However, conventional tube geometry rendering is computationally expensive. Merhof et al. [64] proposed a method using triangle strips and point sprites for white matter tract visualization. The approach facilitates a fast rendering while keeping the advantages

of the 3D geometry. Later, a GPU-based hyperstreamline approach was intro-duced by Reina et al. [88]. The authors proposed a technique in which they generate the tube geometry directly on the GPU and in addition, minimize the data transfer between the CPU and the GPU. However, the method is only ad-vantageous for large datasets. Petrovic et al. [77] presented GPU-based tuboid rendering including a level-of-detail (LoD) management. The method addition-ally includes a text labeling approach which assigns the name of the specific tract to each streamtube.

Illustrative rendering techniques aim to emphasize important features while de-emphasizing less important ones. This leads to images that are more com-prehensible and more recognizable. In medical visualizations, illustrative ren-dering approaches are motivated by anatomical drawings and often include silhouettes, hatching, and shading [83]. Recently, illustrative rendering ap-proaches for fibers were proposed to enhance the structural features of the data. An illustrative rendering approach for line data was proposed by Ev-erts et al. [29]. The authors introduced a technique which focuses on tight line bundles and abstracting less organized line configurations by using depth-dependent halos. The approach features a visual clustering of fiber pathways comprising similar orientations and therefore, visually emphasizes fiber bun-dles. A further illustrative rendering method for diffusion data was presented by Otten et al. [74]. The proposed method visually generates fiber bundles. Hint lines, silhouettes, and contours are used to simultaneously reduce visual cluttering and focus on dominant morphological properties. These approaches emphasize fiber bundles and are advantageous over common fiber visualiza-tions, however, do not include any information about local diffusion profiles.

Diffusion indices, such as the previously presented *MFC* or *ISMI*, provide essential information about local degree of integrity or intra-voxel fiber config-urations. Initially, these indices are presented as bar plots, related to the cross section of a fiber bundle, as proposed by Klein et al. [52]. Jianu et al. [43] pre-sented an interactive tract visualization approach comprising linked 2D rep-resentation: A lower dimensional, color coded visualization was proposed in order to facilitate fiber exploration. Visualizing tract information in separate 2D representation is precise, however not intuitively linked to 3D representations:

Mentally assigning these values to the tract geometry is challenging. For this reason, a direct coloring of lines representing neuronal pathways is advantageous. Brecheisen et al. [14] introduced a parameter sensitive visualization for fiber tracts. The authors applied colormaps to the 3D fiber representations to indicate the influence of FA and curvature thresholds in tractography approaches.

The approach presented in the following discusses and includes recent line rendering approaches and adds vital color information in terms of tract course and integrity directly to the fiber geometry. Additionally, an ambient occlusion approach is integrated to further enhance depth perception.

6.4 Enhanced HARDI-based line visualization

Effective line rendering forms the basis for the advanced fiber visualization approach, presented in the following. In order to enhance spatial depth perception, a color mapping scheme is used for index visualization as well as halo rendering and ambient occlusion. The individual steps are introduced subsequently.

6.4.1 Line rendering

Fiber reconstruction was performed using the distance-based tractography approach for HARDI introduced in Chapter 5. A similar rendering method for generating GPU-based view oriented triangle strips since the one presented by Otten et al. [74] is applied to form the fiber representing geometry. Lines are rendered using the `GL_LINE_STRIP_ADJACENCY_EXT` primitive after pathway reconstruction. Subsequently, a shader pipeline is designed to form and texture the view vector oriented triangle strip.

Access to neighboring primitives is provided within the geometry shader by using the above mentioned adjacency primitive. Information about the neighbors of each vertex is used in combination with the view vector to generate oriented triangle strips, as shown in Figure 6.1. In Code Example 6.1, pseudocode for tube generation in the geometry shader is illustrated.

Code Example 6.1: Pseudocode for streamtube generation: View-vector oriented tri-
angle strips are computed from a line primitive in the geometry
shader.

```
tangent = primitivePos[2] - primitivePos[1]
tangent = normalize(ModelViewMatrix * tangent)
viewVec = viewPosition - primitivePos[1]
shiftingVec = normalize(cross(viewVec, tangent))

color = WHITE
newPosition = primitivePos[1] + width * shiftingVec
newPosition = ModelViewProjectionMatrix * newPosition
EmitVertex

color = BLACK
newPosition = primitivePos[1] - width * shiftingVec
newPosition = ModelViewProjectionMatrix * newPosition
EmitVertex

tangent = primitivePos[3] - primitivePos[2]
tangent = normalize(ModelViewMatrix * tangent)
viewVec =  viewPosition - primitivePos[2]
shiftingVec = normalize(cross(viewVec, tangent))

color = WHITE
newPosition = primitivePos[2] + width * shiftingVec
newPosition = ModelViewProjectionMatrix * newPosition
EmitVertex

color = BLACK
newPosition = primitivePos[2] - width * shiftingVec
newPosition = ModelViewProjectionMatrix * newPosition
EmitVertex
```

Once the triangle strips are generated, the fragment shader is responsible for
imitating tubes by color adjustment: Fragments with a certain distance from
the centerline of the triangle strip fade to black. This is realized by assigning
black and white to the generated vertices in the geometry shader as illustrated
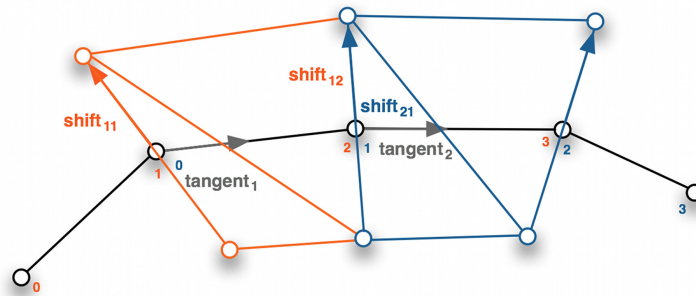
Figure 6.1: Tube-like triangle strip setup utilizing adjacency information in the geometry shader: Individual shader passes are indicated by orange and blue respectively. The shifting vector, used to compute vertices for triangle construction, results from the cross product of the view-vector and the tangent at vertex 1 and 2.

in Code Example 6.1. Therefore, white indicates an upper vertex and black a bottom vertex. Together with the width of a tube, this distance information is used in the fragment shader in order to determine the fragment color: whether the current fragment should be displayed in black or according to a colormap. A closeup of resulting line visualization with applied illumination is displayed in Figure 6.2.

Figure 6.2: Tube-like rendering: Result of view-vector oriented triangle strips with applied directional color coding and lighting for a single fiber.

6.4.2 Colormapping

Directional color codings assign the tangent of a point on the line to a certain color space, such as RBG. This color coding provides spatial information about the fiber course and is well known amongst clinicians. However, fiber integrity indices are of great interest in neuroscientific examinations as well. For this reason, the ODF-based voxel classification index *ISMI*, which was introduced pre-

viously in Chapter 4.6, was utilized for coloring as well. Using *ISMI*, the ODF of each voxel is analyzed and categorized into the following three compartments: isotropic diffusion profiles as well as multiple and singular fiber populations. The following visualizations use a heat map in which black indicates isotropic diffusion, red multiple fiber and yellow single fiber populations.

6.4.3 Halo rendering

The generated geometry can additionally be used to illustrate line surrounding halos. The following presents visual enhancements based on the work by Everts et al. [29].

Similar to the streamtube imitation, the color of the line representing geometry is modified in order to generate line surrounding halos: Fragments with a certain distance to the fiber centerline are colored white and the remaining parts are displayed according the the enabled colormap. Figure 6.5 displays the result for halo rendering and directional coloring.

On the one hand, halos hide visual clutter; however, on the other hand, the understanding of areas with a high fiber-density degree becomes more difficult because the halos of fibers located more in the foreground hide those very close or almost parallel to them. Therefore, Everts et al. suggested a halo depth shift. In the approach presented here, a linear function which displaces halo fragments along the view vector, was used. As a result, halo fragments comprise different depth values according to the distance to the fiber centerline. As follows, adjacent fiber occlusion is minimized and fiber-dense areas are displayed more recognizable due to reduced halo visibility.

Additionally, the authors propose to draw more distant fibers with a smaller line width to support depth perception. This depth cueing approach conveys the idea in which fibers closer to the viewport are thicker than those far away. A summary of the introduced fiber rendering results in following steps:

1. Halo generation based on view-vector oriented triangle strips

2. Halo depth shift along the view-vector

3. Halo depth cueing

6.4.4 Ambient occlusion

In addition to previously mentioned visual enhancements, shadows are an important aspect in depicting depth. One way of incorporating shadowing in renderings that is independent from the geometry's complexity is through the use of *Screen-Space Ambient Occlusion* (SSAO), first introduced by Mittring [67]. By sampling the depth buffer in the fragment shader with a kernel in the neighborhood of any given fragment, the number of neighboring fragments which are closer to the viewpoint than the currently examined fragment is determined. This number is used in turn to darken the current fragment's color, based on the assumption that fragments with a higher number of potentially occluding fragments are darker.

6.5 Results

An illustration of lines showing fibers of the CC is displayed in Figure 6.3. The tube rendering approach is used in combination with a directional color coding. Figure 6.4 displays the same tube visualization method but with applied
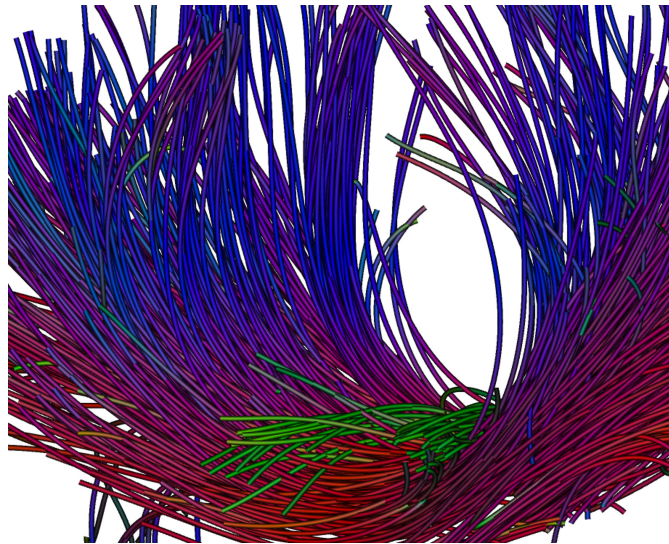
Figure 6.3: Directional color coded streamtubes: Fibers belonging to the CC and the *cingulum* are illustrated.

tract integrity color encoding. Yellow highlighted regions comprise single fiber populations, red multiple fiber populations, and black isotropic diffusion. Considering the region of the *centrum semiovale*, the crossing regions of the CST and the CC is estimated, as indicated in red.
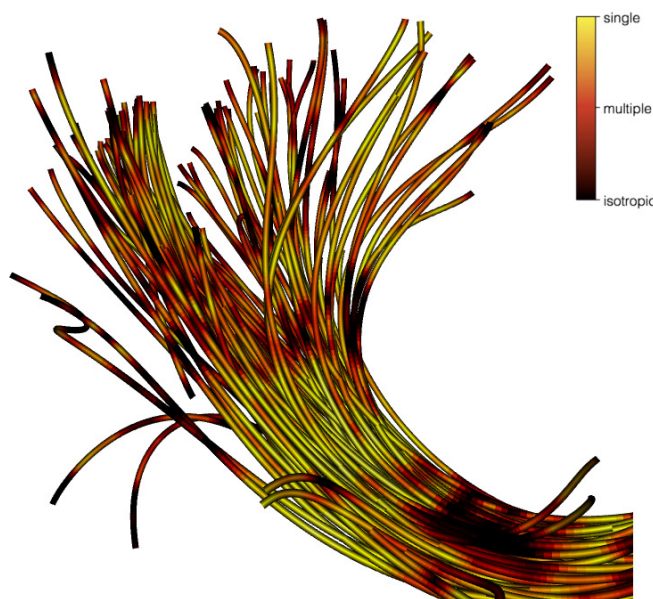
Figure 6.4: *ISMI* color encoding: Streamtube rendering of callosal line representations with applied tract integrity color coding.

An illustration of the introduced halo visualization with directional color coding is shown in Figure 6.5. Depth cueing provides hints about the spatial depth of fibers, in this case blue fibers are further away than red fibers. A halo depth shift is performed in the right image in order to emphasize fiber-dense areas.

Figure 6.6 displays the streamtubes in combination with enabled SSAO. Occluded lines appear darker in the bottom illustration.

6.6 Discussion

Advanced rendering approaches combining effective tube visualization, halo generation, colormapping, and SSAO was introduced in this section. The pre-
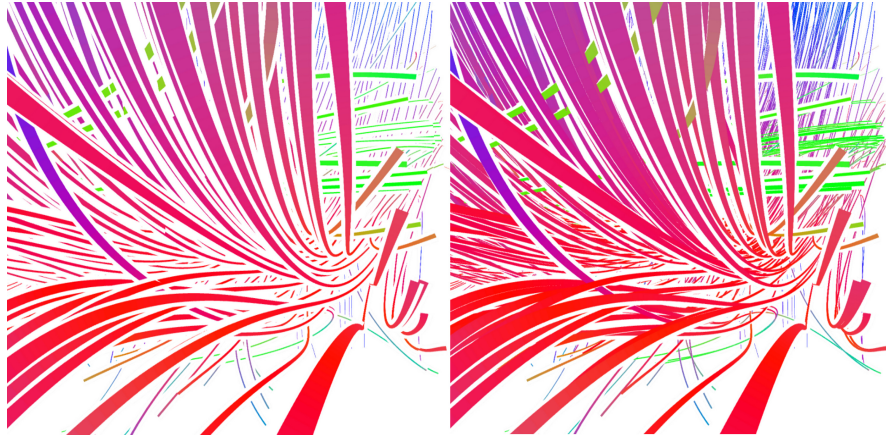
Figure 6.5: Halo rendering and depth shifting: Halos surrounding line renderings (left) and halos being displaced according to their distance from the line center (right).

sented visualization approaches for tractography results feature both: enhanced line rendering and the visualization of diffusion characteristics. Fiber visualization, realized by view-vector oriented triangle strips, is computationally of low cost compared to conventional tube rendering. However, the benefit of streamtubes is retained: a better spatial understanding of the geometry. The presented illustrative methods provide improved spatial depth perception as well as dense line identification. Furthermore, redundant information is obscured by means of halos and depth shift.

The encoding of vital tract information, such as direction and integrity, allows for fast feature examination. Furthermore, it results in a more comprehensible and significant visualization for neuroscientific examinations. In addition, diffusion indices, such as the *ISMI*, is considered as an uncertainty visualization for tractography: Challenging tract configurations, such as fiber crossings, are identified. Thereby, an evaluation of the tractography power, similar to the approach presented in [14], is achieved in an intuitive manner: For example, if line coloring proposes a crossing region but the estimated fibers do not cross, reconstruction results comprise higher uncertainty. Further challenging configurations include fannings, leakings into gray matter or fiber courses with high curvature. The phantom tractography results presented in Section 4.6, Fig-
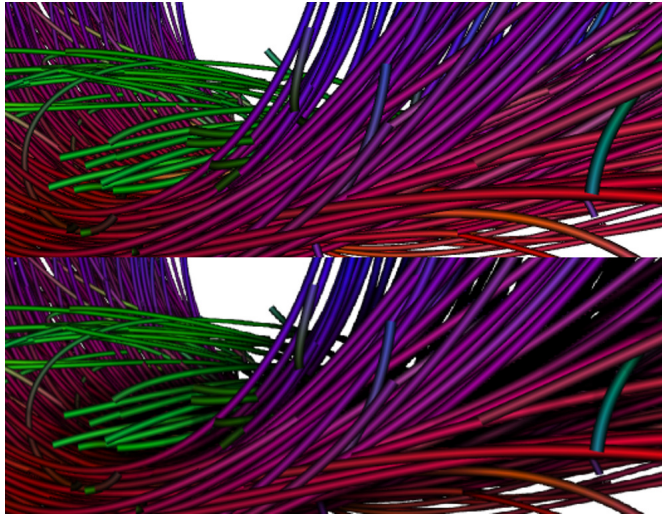
Figure 6.6: Ambient occlusion applied to streamtube rendering: Tube rendering without SSAO (top) and with applied SSAO (bottom).

ure 4.7a, applied the here introduced fiber coloring and revealed a false fiber reconstruction: a leaking into gray matter in the vicinity of the crossing.

The application of enhanced illumination algorithms, such as Phong or ambient occlusion, is challenging for medical visualization. Shading results in a change of color, which leads to difficulties if a colormap is applied: In the case presented, *ISMI* coloring includes white and black in the colormap. However when Phong illumination is applied, highlights also appear in white. This can be easily confused with diffusion characteristic encodings. The same accounts for ambient occlusion in which parts of the background are darkened. Therefore, shading approaches have to consider these aspects when used in combination with colormaps. In the following sections, these issues will be discussed as well as evaluated in greater detail for bundle illustrations.

The proposed enhanced visualization of tracts is beneficial in many neuroscientific as well as neurosurgical questions: In cases of multimodal visualizations for neurosurgical planning, the spatial understanding of fiber bundles is vital for risk-structure evaluation and access path definition. In addition, the proposed visualizations provide significant visual feedback about tract configurations, which is advantageous in all neuro-examinations to detect small or weak

neuronal pathways. As a conclusion, an adequate index visualization, which is related to the local fiber course, is beneficial for both tract examination and evaluation.

Despite the here introduced fiber visualization enhancements, the spatial understanding of single lines can be still challenging. This is especially the case if intricate pathways are under consideration. In the following, bundle visualizations are proposed as a further method for diffusion visualization: In fiber bundle approaches, a neuronal pathway approximating geometry is computed on the basis of single fiber streamlines. Thus, the visualization is directly assigned to a certain anatomical pathway by a clinician.

7 Intra-bundle visualization

7.1 Overview

In the previous section, a visualization of lines resulting from HARDI tractography approaches was introduced. This visualization is based on tractography techniques which use the local ODF to estimate trajectories and are best known representations of diffusion data. However, clinicians are often interested in the spatial position and shape of whole bundles as well as the border of certain neuronal pathways. This Section starts with a discussion of scientific questions regarding bundle visualization in Section 7.2 and a literature review on diffusion visualization in Section 7.3. In the following, the developed intra-bundle raycasting and slicing approaches for diffusion visualization are presented in Section 7.4, the results in Section 7.5, and a discussion in Section 7.6. Parts of the presented approach were published in [94] and a user study evaluating the understanding of visual enhancements in [96].

7.2 Introduction

The generation of hulls approximating reconstructed fibers is beneficial in neurosurgical planning, for example, to determine the risk of an intervention [62, 72, 120]. Hulls are motivated by the fact that the computed streamlines only approximate the diffusion process within a voxel; the hulls in turn approximate the reconstructed fibers. Conventionally, these hulls are monochromatic and do not include information about the underlying diffusion profile. However, this information is essential in neurological examinations and preoperative planning and is in the following combined with hull visualization to improve tract-related examinations.

The following clinical and scientific questions are interesting in terms of bundle visualization:

- How can bundles be computed using diffusion MRI data?

- How can integrity information and intrinsic fiber configurations be visualized on bundle surfaces?

- Can visual enhancements increase spatial perception?

- What are the potential clinical applications of bundle visualizations?

In order to answer these questions, visual exploration approaches based on HARDI reconstructions, combining both bundle morphology and intra-voxel fiber characteristics are proposed and discussed in this section.

The fiber encompassing geometry is defined using a hull generation approach. Subsequently, the centerline for this geometry is computed by means of a 3D skeletonization approach. A raycasting-based visualization of intra-bundle diffusion properties is developed using an evaluation of bundle characteristics on a ray from a vertex to the closest bundle centerline point. The information within a bundle is visualized on the geometry's surface using colormaps. Furthermore, *Centerline Slicing* is introduced as a visual exploration method for diffusion characteristics using a plane which is orthogonal to the centerline. The slicing reveals the bundle shape as well as diffusion characteristics for the current cross-section of the bundle. In addition, visual enhancements including Phong illumination, ambient occlusion, and silhouettes are integrated and can be activated by the user to facilitate depth perception. A user study was performed in the course of a research study at the Neuroscience Unit, Institute of Biomedicine/Physiology, University of Helsinki to evaluate the visualizations in terms of general understanding, spatial perception, and neuroscientific applications.

With the proposed techniques, the view does not suffer from cluttering and information about the global bundle's orientation, shape, integrity, and intra-voxel orientations is provided for the user.

7.3 Related work

Several visualization techniques for diffusion data emerged in the last decade. Approaches include tractography methods which reconstruct and visualize neuronal pathways along with anatomical data as well as methods that aim to display local diffusion profiles and thereby revealing information about tract integrity and local fiber distribution. Additionally, methods that aim to combine both types of information, such as the approach presented here, were introduced.

Tractography techniques provide essential information about the location and orientation of neuronal pathways; however they do not conventionally include any indication about local tract properties such as integrity or fiber configuration. For this reason, a further visualization strategy for diffusion data exists, directly displaying the intra-voxel diffusion pattern using a geometry representation known as glyphs. A glyph-based visualization of the local diffusion tensor was presented by Kindlmann [49]. He used ellipsoids, cuboids and superquadrics to represent the local shape of the diffusion tensor. In terms of HARDI, an enhanced ODF glyph rendering was proposed by Peeters et al. [75]. These approaches are beneficial in terms of analyzing local diffusion profiles precisely. However, the understanding of the global tract configuration is lost. Therefore, a constitutive approach called *Glyph Packing* was introduced by Kindlmann and Westin [50]. This approach arranges the superquadric glyphs in a way that local diffusion profiles are visualized but the continuous structures, the fiber courses, simultaneously become apparent. Chen et al. [125] introduced the *Merging Ellipsoids*. A glyph-based method, dealing with problem of combining local and global diffusion information. In the presented approach, the authors interactively blend neighboring glyph representations into each other. These approaches were introduced in order to combine local diffusion profiles with continuous structures. Resulting visualizations combine local tensor shapes with connectivity information. Although glyphs provide a direct representation of the tensor data, their interpretation is challenging. For this reason, an integration into a clinical environment is unreasonable. As a result, visualizations based on line rendering and include additionally informa-

tion on the local diffusion pattern arose. Zhang et al. [130] used streamtubes
and streamsurfaces to visualize the local diffusion profiles of DTI. The authors
visualized linear diffusion tensor profiles using a tubular geometry whose ori-
entation corresponds with the direction of the principal eigenvector of the diffu-
sion tensor. In addition, the cross-section of a streamtube represents the ellipsis
formed by the two remaining eigenvectors of the tensor at the position in the
volume dataset. Planar diffusion profiles are represented using surfaces de-
fined by the two eigenvectors with highest eigenvalues. Both representations
are combined within one 3D visualization. A similar approach was introduced
by Vilanova et al. [119]. These approaches suffer the following two problems:
visual cluttering and unclear streamsurface meaning due to the lack of planar
diffusion profiles in the brain.

A further approach, which is more suitable for clinical application, is the vi-
sualization of fiber encompassing hulls. A fiber cluster visualization technique
was introduced by Chen et al. [19]: Following a hierarchical clustering step, the
fiber hull is generated and visualized in combination with either the individual
fibers or a principal fiber that approximates the bundle course. Similar to the
approach presented by Wenger et al. [128], this visualization includes volume
data and aims to combine spatial information about the fiber course and volu-
metric anisotropy information. However, no anisotropy information is directly
assigned to single tracts using the proposed methods, which makes a detailed
tract examination difficult. A method for the statistical mapping of white mat-
ter tracts was presented by Yushkevich et al. [129]. The authors use a paramet-
ric geometric model to represent the course of major neuronal pathways and
compute statistics such as the ADC using the geometric representation. This
method is only applicable in terms of simple, thin structures; however, the true
fiber course of the CC comprises a more complex shape due to the fanning into
the whole hemisphere. Klein et al. [52] presented an approach for DTI charac-
teristic quantification of fiber bundles. The proposed method uses a resampled
fiber bundle and computes an average principal fiber from the bundle. After-
wards, orthogonal planes are generated and used to compute FA values on the
cross-section of the bundle. This approach is beneficial since the quantification
of DTI characteristics is possible for arbitrarily oriented fiber bundles and en-

ables a tract-specific examination of diffusion properties. However, the simple approach presented for centerline reconstruction is not sufficient for complex bundle configurations.

A first step towards visualizing integrity information on bundle surfaces and slicing planes was made by Goldau et al. [35]. In their approach, the FA value is either visualized along fiber bundles using a color-coded slice or directly on the bundle boundary. For bundle colormapping, the authors compute a single FA value from samples on a slice orthogonal to an average fiber's tangent. Subsequently they interpolate the obtained mean values of two neighboring planes to assign a characteristic to a specific vertex. This comprises many averaging steps and hence, the resulting index value is less representative in case of more complex fiber bundles. The approach developed in the course of this thesis, computes a ray for each individual vertex, resulting in a more precise representation of diffusion characteristics. In addition, the focus is on examining HARDI fiber bundles and characteristics and the introduced methods feature a more accurate centerline and apply advanced visualizations. A user study was performed to evaluate the understanding of the visualizations and the benefit for neuroscientists.

7.4 Intra-bundle HARDI raycasting

The HARDI raycasting approach presented in the following utilizes trajectories that were computed using the distance-based tractography approach presented in Part 5 as well as the ISMI diffusion classifier introduced in Chapter 4.6.

7.4.1 Hull generation

The applied hull generation algorithm extends the approach proposed by Merhof et al. [62]. The method is divided into the following four consecutive steps: volume rasterization, volume filtering, surface extraction, and surface filtering. The first step, volume rasterization, computes a binary fiber volume out of the reconstructed fiber set. It contains unwanted edges and is subsequently smoothed with a 3D Gauss filter. This volume serves as the basis for the com-

puting of the isosurface. Surface extraction is commonly performed using a *Marching Cubes* algorithm [59]. As in the proposed approach, a scale-dependent Laplace filter is applied for surface smoothing. The method includes a weighting term that defines the translation vector for point displacement according to the geometric center of neighboring edges. The filter multiplies the computed displacement vector by the sum of the length of all neighboring edges E and is defined as follows:

$$p' = p + \frac{\lambda}{E} \sum_{i=0}^{n-1} \frac{(q_i - p)}{\|q_i - p\|}, \; with \; E = \sum_{i=0}^{n-1} \|q_i - p\|, \tag{7.1}$$

where p is the original mesh point, p' is the displaced point, n is the number of considered neighbors, and λ is a weighting factor. The amount of iterations and the weighting factor are adjustable; therefore, the degree of smoothing is observed by the user.

The proposed algorithm was extended in terms of surface filtering by including a reference volume which controls the adjustment of the geometric hull via the underlying fiber volume. In particular, the reference volume acts as a border for adjusting the mesh points and should not be infiltrated during point displacement. If the applied scale-dependent Laplace filter for surface smoothing leads to a position infiltrating the reference volume, the weight factor is reduced. This is done for a certain number of steps, until either a position outside the reference volume is obtained or the maximal number of iterations is reached. In the latter case, the original point is returned. In this approach a rasterized fiber volume was used as a reference image, however, others, such as FA volumes, are feasible as well.

7.4.2 Centerline extraction

Several approaches for centerline reconstruction of fiber bundles exist in the literature [19, 52]. These approaches are based on a principal fiber computation representing one centerline for a whole bundle. However, they require similarly oriented and distributed fibers within the bundle to lead to sufficient results. In cases of complex fiber configurations, resulting from HARDI tractography, a

principle fiber does not appropriately characterize a bundle. Figure 7.1 illustrates the problem in terms of fanning fiber tracts.

<div align="center">(a)   (b)</div>
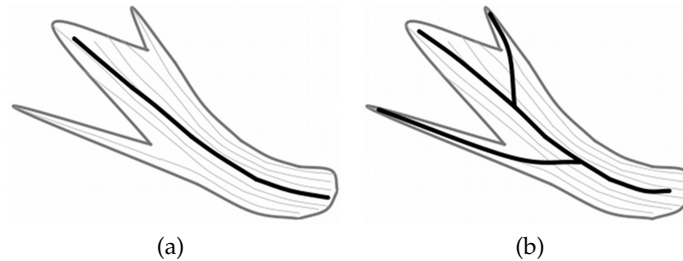
Figure 7.1: Centerline computation: Schematic illustration of a principle fiber (7.1a) and a skeleton (7.1b) representation for a fanning fiber bundle.

For this reason, a skeletonization approach is applied using the fiber bundle morphology. In this approach, a distance transform is applied to control the successive erosion of border voxels. The user influences the output by adjusting the threshold defining the binary bundle hull. Thus, shape properties are either enhanced or reduced which affects the course and complexity of the centerline.

7.4.3 Visualization approaches

The following section develops intra-bundle raycasting-based visualizations and a centerline slicing approach using the aforementioned precomputation results, the fiber tract encompassing hull, the centerline, and the diffusion characteristics. Figure 7.2 both shows the processing pipeline and provides an overview of the methods developed. For an enhanced three-dimensional understanding of the bundle shape, a silhouette rendering approach is applied, as well as Phong shading and ambient occlusion. Silhouette rendering is performed by analyzing variances of neighboring normals in a deferred shading approach as introduced by Saito et al. [102]. Additionally, a *Screen-Space Ambient Occlusion* (SSAO) approach was implemented, first introduced by Mittring [67]. SSAO samples the depth buffer in the neighborhood of each fragment. The number of fragments closer to the viewport than the current one is used to darken the current fragment's color. However, combining colormaps with enhanced rendering tech-
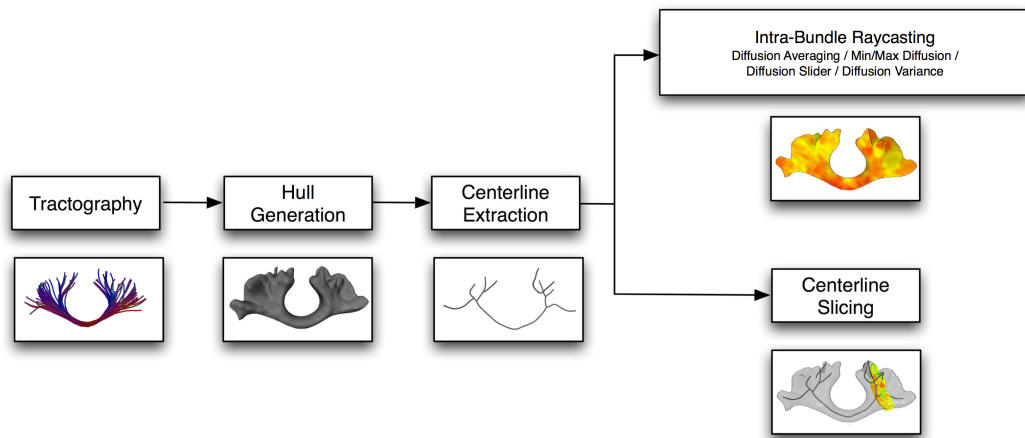
Figure 7.2: Computation pipeline for HARDI-characteristic visualization: Preprocessing steps are shown in the left and the developed intra-bundle visualizations in the right part of the image.

niques to facilitate depth perception alters color appearance and can lead to false interpretations. Therefore, the user can interactively switch the rendering techniques on and off and thereby combine various illustration techniques or explore the bundle without any visual enhancements. In addition, an evaluation of the introduced rendering techniques was performed in the course of a user study and are discussed in Section 7.5.2. In the following intra-bundle visualization, two different colormaps are used to emphasize the different meaning of each index. The first one characterizes the intra-bundle fiber configuration, where red indicates single, yellow multiple fiber configurations and green isotropic diffusion. The second colormap, encoding the variance, highlights regions with high variance in cyan and regions with low variance in blue.

Intra-bundle raycasting

The first method uses a novel intra-bundle raycasting approach with the hull geometry as input and realized though a GPU shader pipeline. The centerline of the fiber tract is encoded in a 2D texture and transferred to the GPU as well

as a 3D texture comprising the diffusion characteristics in this case the voxel classification volume. The vertex shader computes the texture coordinates for characteristic evaluation as well as the nearest point of the centerline. Further, a ray is traced from the current hull's vertex to the obtained centerline point, as illustrated in Figure 7.3, this ray is used for diffusion characteristic evalu-
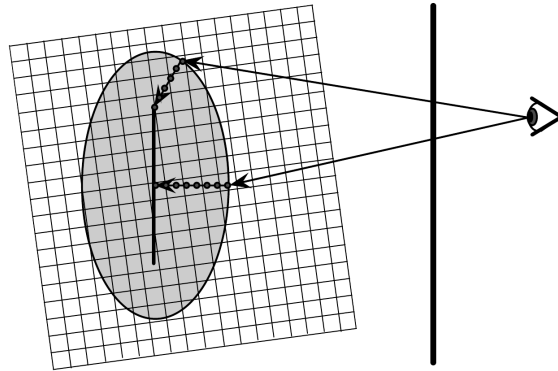
Figure 7.3: Ray computation: The vertex shader computes the ray from the current vertex to the nearest centerline point.

ation. Several visualization strategies for intra-bundle raycasting were developed, motivated by volume rendering, and designed to aid clinicians in analyzing diffusion characteristics of neuronal bundles. In the following, these strategies are explained.

Diffusion Averaging. For *Diffusion Averaging*, samples along the ray from the vertex to the nearest centerline point are computed using a certain step length and resulting in n distinct positions. These samples are used to evaluate the diffusion characteristics and compute the mean value of all the obtained values. The final fragment color is determined through colormapping and thereby reflects the mean diffusion value from a vertex to the centerline.

Min/Max Diffusion. The *Min/Max Diffusion* mode is motivated by the *Maximum Intensity Projection* (MIP) method, a transfer function, projecting the maximum value along a ray to the image plane. Transferring the idea to the ap-

proach presented results in computing the minimum and maximum characteristic value along the ray and the use of this value for colormapping. Within this visualization, a single characteristic value is displayed.

Diffusion Slider.   With the *Diffusion Slider*, the user interactively examines diffusion characteristics along the ray. In this case, no averaging of diffusion values takes place. Instead, the ray is defined by the vertex position, and the centerline point is normalized and sampled at discrete points. The resulting single diffusion values are visualized directly on the bundle's surface. As a result, visualizations of diffusion characteristics from the hull to the bundle's centerline are feasible.

Diffusion Variance.   Using the *Diffusion Variance* mode, both the homogeneities and the inhomogeneities of the bundle are highlighted. The variance of ISMI values is computed along the traced ray and a colormapping is applied to display the results on the bundle's surface.

Centerline slicing

In addition to the approaches presented in the previous section, a second visualization method of intra-bundle diffusion characteristics was implemented, the *Centerline Slicing*. This approach uses the same precomputations: the geometric hull, the centerline, and the diffusion characteristic volume. A plane orthogonal to the tangent of a user specified point on the centerline is generated and utilized for visualizing the color-coded index through texture mapping. To define the coordinate, the user first selects a point by clicking the mouse on a rendering of the centerline, as illustrated in Figure 7.4. Next, a shader pipeline uses the precomputed centerline rendered by using the `GL_LINES` primitive as an input and generating the plane as the output. The coordinates of the user-defined point are transferred to the shaders via uniforms. The geometry shader is designed to generate a plane if the first coordinates of the current primitive are within an interval around the selected centerline point. The tangent of this centerline segment acts as the normal for the plane and is computed by subtract-
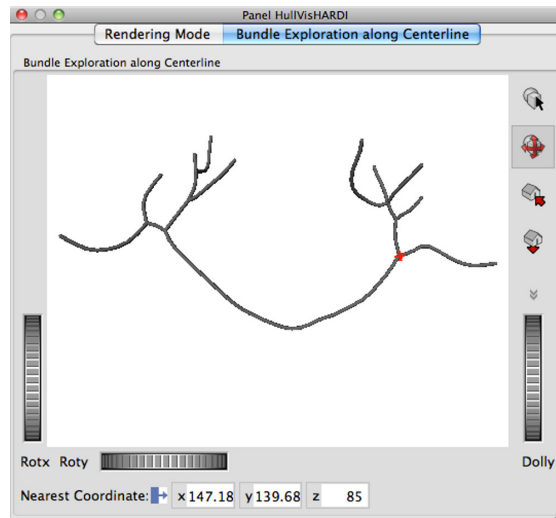
Figure 7.4: User interaction for plane generation: In order to define the point on the centerline, the user has to click the mouse on the centerline.

ing both of the primitive's coordinates. No distinct centerline tangent, which is used to generate the plane, exist in bifurcations. In this case, the view-vector is used as the plane normal. Thus, the user interactively examine the diffusion pattern while moving the camera, and the plane origin remains unchanged. To enhance the spatial understanding of the bundle, parts of the plane not lying within the bundle are rendered transparent. As a result, the plane not only exhibits information about the diffusivity, but also reveals the shape of the cross-section of the bundle for arbitrarily oriented centerlines.

7.4.4 Clinical study design

Expert evaluation of the presented approach was performed at the Neuroscience Unit, Institute of Biomedicine/Physiology, University of Helsinki and at the BioMag Laboratory at the Helsinki University Central Hospital. Seven students, researchers, and medical doctors in the field of neuroscience participated and rated the approaches with respect to usability in neuroscience and visual understanding. The evaluation was designed to answer the following major questions:

- Whether the approaches provide a better understanding and insight into the data,

- if the introduced perception enhancements facilitate depth impression, and how they affect the understanding of the visualizations as well as

- in which neuroscientific and neurosurgical questions the approaches can be beneficial.

The approaches were presented and evaluated in two stages. At first, all intra-bundle visualizations, as proposed in Section 7.4.3, were introduced to the audience in the form of a presentation. The second part was performed using two different questionnaires. Experts discussed and rated the presented approaches in terms of understanding and usefulness and suggested a field of application. In the following part, experts evaluated the bundle shape perception: Perception enhancements are accompanied by changes in color and for this reason potentially affect bundle diffusion interpretation. Thus, a trade-off between depth perception and adequate colormap illustration exists, and the decision for the best visualization is challenging. For this reason, illustrations featuring single and combined Phong illumination as well as silhouettes and ambient occlusion were presented. Experts rated the clarity and improvements of the visualizations considering spatial depth perception as well as the interpretation of bundle colors. Figure 7.5 presents individual stages of the user study.

7.5 Results

In this section, results of the visualization method as well as the user study are presented and discussed.

7.5.1 Visualization methods

The aim of the presented approach is to enhance visualizations in terms of challenging fiber configurations, reconstructed using HARDI techniques. The focus is on fibers belonging to the CC and running in the *centrum semiovale*. In the

---

1. Presentation of the developed intra-bundle visualizations

2. Questionnaire I: understanding and potential applications
  - personal data (position and field of research)
  - identification of the most significant approach
  - understanding and usefulness
  - potential clinical applications

3. Informal discussion of potential findings revealed by the visualizations

4. Questionnaire II: rating of individual visual enhancements
  - understanding
  - depth impression
  - differences in color interpretation

Figure 7.5: Individual stages of the user study.

following, tracts are displayed without anatomical volume rendering in order to focus on hull visualization. Figure 7.6 displays the *Diffusion Averaging*, *Max Diffusion*, *Min Diffusion*, and *Diffusion Variance* visualization on the hull.

The result of the *Diffusion Slider* is shown in Figure 7.7 for the hull and centerline together with results of the *Centerline Slicing* approach in the center of the CC and in a region with more complex fiber distributions. The hull is visualized as slightly transparent in combination with the bundle centerline and silhouette as well as the plane orthogonal to a chosen centerline point. Figure 7.8 displays a combination of the implemented depth enhancements, silhouettes, Phong illumination, and ambient occlusion.

All presented visualizations achieve interactive frame rates. Performance evaluation was accomplished on a Core2 Duo, 3.16 GHz with 4 GB RAM and a NVIDIA GeForce GTX 285 graphics card. The following average frames per second (fps) were achieved for the reconstructed fibers of the CC. The raycasting-based approach features 11fps when performing a 360° rotation of the bundle. Ambient occlusion and silhouette visualization reduce the average fps to 6. The *Centerline Slicing* mode achieved 22fps on average.

Using the presented visualization approaches arbitrary neuronal pathway morphologies are displayed with significant diffusion encoding color values. However, the method is highly dependent on the bundle's centerline approximating the course of the current tract. For complex morphologies, a detailed
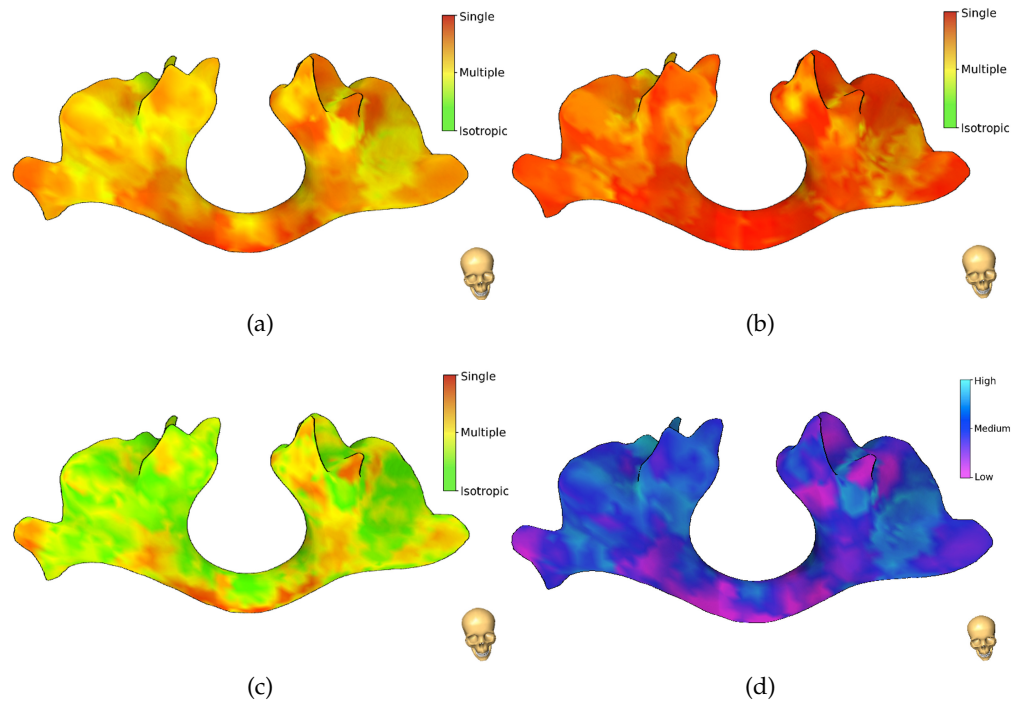
Figure 7.6: Colormapping of values along the ray: In the results for the *Diffusion Averaging* visualization, the CC appears yellow (multiple fiber distributions) where the SLF and the CST cross (7.6a). Using the *Max Diffusion* mode, yellow parts also reveal multiple diffusion directions (7.6b). On the other hand, when using the *Min Diffusion* visualization, regions with highest integrity appear red (7.6c). The *Diffusion Variance* color encoding highlights regions with high variance in cyan and regions with low variance in blue (7.6d).
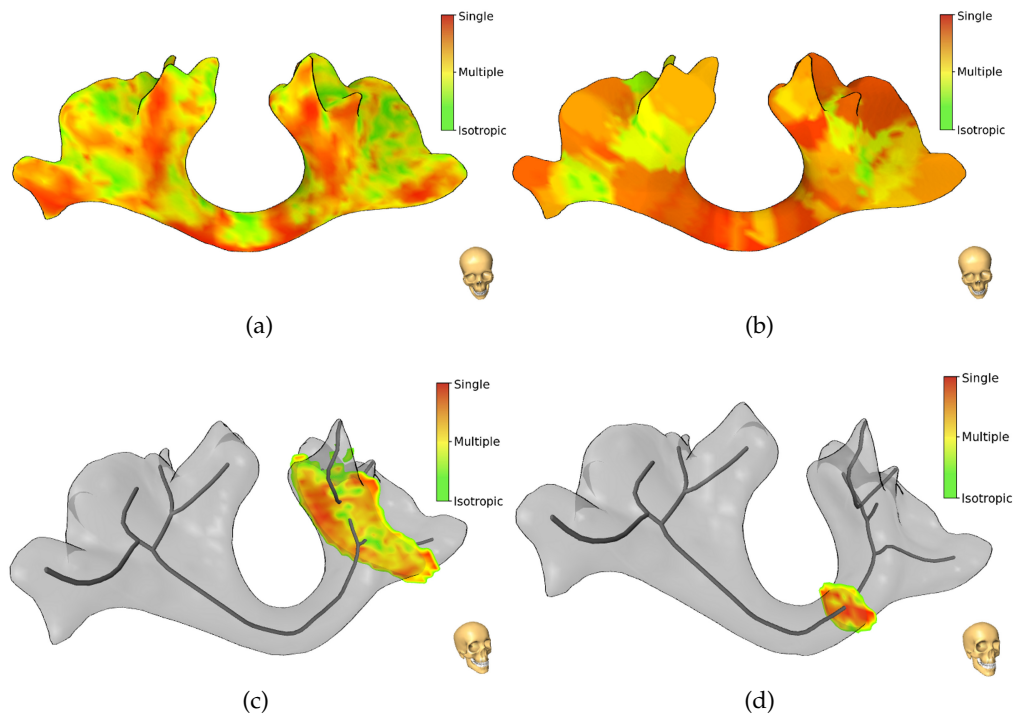
Figure 7.7: Colormapping of values along the ray: Values on the hull (7.7a) and the centerline (7.7b) using the *Diffusion Slider*; parts of the hull leaking into gray matter appear in green (isotropic diffusion); high single fiber configuration is obtained in the center of the CC; and *Centerline Slicing* within regions of complex diffusion profiles in the CC (7.7c, 7.7d).

skeleton is crucial to reliable diffusion information since the ray is determined by the closest centerline point; however, a detailed centerline reduces performance since more points have to be considered for raycasting. In the current approach, the reference centerline point is computed for each ray for each frame. However, this can be precomputed on the CPU and the reference centerline point can be stored as an attribute variable for each vertex. In addition, the amount of diffusion information which is mapped through the ray to a bundle vertex, depends on the centerline's curvature and is not uniformly distributed. Furthermore, in terms of large bundles or a less representative centerline, the *Diffusion Averaging* visualization might not be representative since all values on
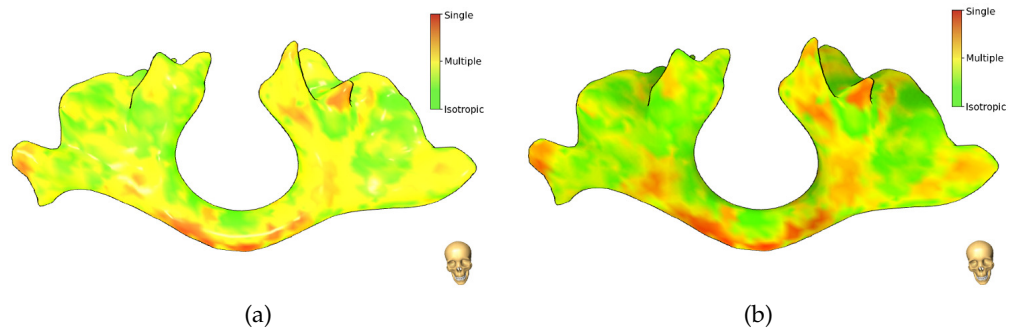
Figure 7.8: Visualizations for spatial depth enhancements. Both images feature the *Min Diffusion* mode and include silhouette rendering and either Phong illumination (7.8a) or ambient occlusion (7.8b).

the ray are taken into consideration. This accounts for inhomogeneous bundles as well since if the variance of diffusion values along the ray is too high a mean value can lead to false interpretation. In these cases a preliminary examination of the bundle using the *Diffusion Variance* mode and a subsequent adjustment of the centerline enhances the visualization. Also, an examination using the *Diffusion Slider* is more adequate.

7.5.2 User study

In the following, a discussion of the approaches is presented along with an introduction of the user study results in terms of general understanding, visualization enhancements, and applications to neuroscience.

Visualization methods. The *Diffusion Averaging* approach was one of the favorite visualizations with experts. They stated that it provides a good first impression about the underlying diffusion and that it is a straightforward visualization.

The *Min/Max Diffusion* modes are helpful in terms of identifying regions of multiple fiber populations and linear diffusion profiles. In the presented diffusion characteristic scheme an applied minimum diffusion raycasting mode reveals areas with the highest single fiber population. Reconsidering Figure 7.6

and the *Minimum Diffusion* visualization: Regions appearing red (the center of the CC) include no isotropic diffusion since the isotropic diffusion has a lower index value than the single fiber distribution. Hence, red areas in this visualization mode are considered as the most directional fiber pathways. On the other hand, regarding the *Max Diffusion* visualization, yellow marked regions comprise no single fiber distributions since the maximum value is visualized and single fiber distributions comprise a higher index value than multiple fiber distributions.

The evaluation of diffusion values at the centerline of a bundle using the *Diffusion Slider* mode is of special interest since the centerline is considered as the skeleton, representing a whole tract. Therefore, diffusion values of the centerline are especially helpful in tract-based examinations.

Visualizations of diffusion characteristics on the hull are considered as an uncertainty visualization since green parts indicate isotropic diffusion; hence, these parts of the reconstructed bundle do not belong to a neuronal pathway – the bundle leaks into gray matter. Additionally, the hull representation in Figure 7.7 exhibits a very interesting fact: The hull grows into the cingulum bundles, two white matter tracts running above the CC, indicated by the two red parts on top of the center.

Results of the *Diffusion Variance* visualization correspond with the findings of the *Min/Max Diffusion* mode: Similar values in both of the *Min/Max Diffusion* visualizations are identified in the center of the CC as well as in the right upper part of the bundle. These regions appear in purple and indicate low variance. Considering the fanning regions of the CC, deviating values are observed in the min/max visualizations in terms of multiple and isotropic diffusion, these regions are highlighted in blue and cyan in the variance diffusion mode. Regions where the bundle leaks into gray matter comprise the largest variance values within the voxel classification values and are marked in cyan.

In the *Centerline Slicing* mode, a more detailed examination of the diffusion profiles is provided. This is beneficial for regions with high variance and forms a subsequent step. Additionally, this visualization can be integrated in the operation microscope during surgery in terms of an overlay to indicate preoperatively computed diffusion characteristics directly on the brain.

The findings within the visualizations correspond with the medical knowledge of the CC: The center of the CC is the area with the highest integrity and the highest directionality. However, the region of the *centrum semiovale* comprises more difficult fiber distribution profiles, such as crossings of the CST and the CC. These configurations are revealed through the presented visualizations.

Visual enhancements.   When choosing between single Phong illumination, ambient occlusion, silhouettes, and visualization with no depth enhancement, ambient occlusion was considered to feature the best depth impression. Moreover, when adding silhouettes to the visualizations, all participants agreed that the combination of ambient occlusion and silhouettes as displayed in Figure 7.8 is the best depth encoding visualization. Single silhouette enhancement was rated second. Participants recognized the changes in terms of color appearance caused by ambient occlusion and Phong illumination and; however rated the influence for Phong as having a greater impact on color interpretation than ambient occlusion. In addition, they judged depth encoding as a crucial feature for bundle visualization. However, it could not be significantly determined whether spatial depth perception or accurate colormap visualization is more important to experts. For this reason, it was decided to enable or disable single visualization enhancements manually. In general, Phong illumination was reported to be very confusing and led to severe changes in terms of color appearance, and resulting misinterpretations considering tract integrity and diffusion distributions were observed. Summarizing, the most favorite visualization is ambient occlusion in combination with silhouettes. However, it should be switched off for color interpretation.

Applications to neuroscience.   Experts think that the provided visualizations are of great interest in their field of research and are beneficial to answering specific neuroscientific questions. The *Diffusion Averaging*, *Min/Max Diffusion*, and *Diffusion Variance* modes are of specific interest. The *Diffusion Averaging* mode provides a good first overview while the *Min/Max Diffusion* and the *Diffusion Variance* visualizations highlight regions of interest, such as areas with multiple maxima or potential abnormalities which influence the local diffusivity. In

terms of applications to neuroscience, they mentioned amongst others: Neurosurgical planning, such as lesion detection and analysis, as well as disorder monitoring, for example in stroke patients. Furthermore, an integration of the approach into a TMS system is feasible: Visualizing diffusion characteristics of neuronal pathways originating from certain regions activated by TMS, can provide information about brain connectivity and integrity. This is of major interest in fundamental neuroscience. In addition, using this information, further TMS regions can be defined and evaluated for activation or blocking.

7.6 Discussion

Contrary to the previous section which concentrated on advanced line rendering, this section discussed enhanced fiber bundle visualizations. Fiber bundles are advantageous over single line representations since the visualization focuses on the boundary as well as the shape of a tract, which is more significant for clinical purposes than single streamlines. Furthermore, if the visualization is based on HARDI tractography, more complex configurations, such as callosal fibers to lateral areas of the hemisphere, can be detected. This causes a more cluttered 3D representation and hinders interpretation. Today, it is possible to describe intra-voxel diffusion patterns using HARDI classifiers. However, an effective, user-friendly and problem-specific visualization had been missing. An intuitive visual exploration of diffusion characteristics in combination with tract morphology is of great interest in fundamental neuroscience and in many clinical applications. The presented intra-bundle visualization approaches take a step towards such a combination. Experts deemed the approaches useful and as providing a better understanding as well as interpretation of diffusion data as well as suggested potential applications. The illustration of intra-bundle HARDI characteristics was considered as an important contribution to diffusion visualization and providing vital insight. However, the user study showed, that visual enhancements, such as Phong shading or ambient occlusion do not benefit all clinical questions. In addition, clinicians and neuroscientists are not yet used to 3D visualizations and can easily misinterpret illustrations. For example,

if the neurosurgical aim is data exploration in terms of either white matter pathway location, the identification of fiber dense areas or their relation to further anatomical structures, then visual enhancements can provide a vital benefit in terms of spatial understanding. However, in terms of detailed fiber integrity examination and if colormaps are involved, highlights can easily lead to misinterpretations and are disadvantageous. As a result, visual enhancement integration has to be considered carefully and only applied if appropriate to the task.

The remaining issue in white matter fiber visualization is to solve the problem of visual cluttering caused by the intricate nature of the white matter network. If only single fiber tracts or major neuronal pathways are being examined, 3D visualization is easy to understand. However, if more complex fiber configurations are under consideration and more fiber tracts are interwoven, visualizations are no longer intuitive and evaluation becomes challenging. Representing pathways as bundles is a first step to reducing this visual clutter. However, more advanced exploration techniques are required to enable a detailed examination. The following section is built on the discussion of enhanced fiber rendering and bundle visualization and addresses the issue of intricate fiber pathway visualizations using focus and context visualizations.

8 Focus and context visualizations

8.1 Overview

The previous sections introduced two visualization approaches for diffusion data based on streamline fiber reconstructions. The first is designed to enhance line representations by applying depth encodings and illustrative rendering techniques. The second method aims to visualize fiber hulls computed from streamlines in combination with intra-bundle diffusion characteristics. It is motivated by the conclusion that hull visualizations are more intuitive as well as of more clinical use than single fiber representations. However, due to the complex nature of HARDI-based fiber bundles, exploration becomes challenging if more than one bundle is under consideration. In the beginning of this section, the guiding questions in terms of bundle visualization regarding single as well as interacting fibersets are presented in Section 8.2 followed by a review on focus and context visualizations in Section 8.3. The developed visualizations are presented in Section 8.4 followed by results in Section 8.6 and a discussion in Section 8.6. The presented approach was published in [99].

8.2 Introduction

HARDI-based tractography approaches result in more complex line representations than DTI-based due to the detailed diffusion profile, the ODF. Individual line interpretation is cumbersome and benefit from advanced visualization techniques: A combined approach including lines as well as hulls, is beneficial in order to estimate bundle shape determining fibers and reveal bundle characteristics on demand. Resulting visualizations feature both knowledge about intrinsic fiber configurations as well as the global bundle shape. However, de-

signing an approach including inner fibers as well as encompassing hulls is a challenging task. Focus and context rendering approaches target this issue by applying various rendering styles to different objects. Thereby, a combined visualization is feasible. Scientific questions, guiding focus and context visualizations for single fiber bundles are:

- How can line renderings and bundle visualizations be intuitively and meaningfully combined?

- Which are the important features of fibers within a bundle?

- How can fiber features be visualized?

Furthermore, due to HARDI's ability to model complex subvoxel diffusion profiles, fiber pathways may be seen to overlap or interweave. If such configurations are visualized using bundle techniques single fiber pathways cannot be easily differentiated. In fact, this issue does not occur when using DTI-based reconstructions since streamlines do not interfere with each other as they do in HARDI. The following questions must be posed in order to visualize multiple potentially intersecting bundles:

- How can multiple fiber bundles be visualized intuitively?

- How can pathways be distinguished?

- How can complex areas be highlighted?

Focus and context rendering approaches usually apply different rendering styles for each object group. According to Preim et al. [82] objects are categorized into the following classes: focus objects, which are objects of interest; near focus objects, which are objects facilitating functional interrelations; context objects, which are all remaining objects; and container objects, where one object contains all of the others. In the case demonstrated, focus objects are fiber pathway representing lines. The context object is the hull, representing a neuronal bundle, and the container object is the brain surface.

In the following, the *BundleExplorer* is introduced as a focus and context approach for complex diffusion configurations with minimal user interaction. It

is build on previously introduced diffusion reconstructions and visualizations: The tractography approach was proposed in Section 5, fiber visualization in Section 6, and bundle computation in Section 7. Inner-bundle fiber visualizations are integrated to reveal trajectories within their global context. Intersecting-bundle visualizations are proposed in order to extract spatial features and enable an intuitive exploration of crossing fiber pathways. Spatial and functional bundle features are encoded in illustrative fiber renderings to enhance diffusion data exploration. A GPU-based framework for cutaway rendering is proposed to facilitate a fast focus and context rendering of white matter pathways and their encompassing hulls. Resulting visualizations feature both knowledge about intrinsic fiber configurations as well as the global bundle shape.

8.3 Related work

Related work on the presented visualization issue targets focus and context visualizations to provide an embedded presentation. In addition, illustrative rendering methods are important to enable a discrimination of focus and context objects. Scientific work related to our approaches is reviewed in the following.

A focus and context rendering approach for preoperative neurosurgical planning was proposed by Beyer et al. [10]. The authors introduced a multimodal, high-quality volume visualization approach including cut-out techniques to visualize deep-seated brain structures. A skull peeling approach is applied by generating a view-dependent depth mask. Therefore, visualizations of the surgical approach and especially inner brain structures of interest are feasible. Bruckner et al. [15] introduced a context-preserving volume rendering approach in which a transfer function is used to evaluate parameters such as shading intensity, gradient magnitude, and distance to the eye point as well as previously accumulated opacity, in order to determine less important regions and adjust their opacity. Wang et al. [122] introduced the *Magic Volume Lens* as a GPU-based focus and context framework for volume data visualization. The proposed approach is based on direct volume rendering and incorporates several lens shapes as well as transition regions between focus and context ob-

jects. The here presented methods are strongly influenced by an approach called *ClearView*, as presented by Krüger et al. [54, 55]. *ClearView* comprises a GPU visualization framework for texture-based raycasting. The goal is to focus on particular areas, while providing vital context information. The authors propose several approaches to automatically define focus areas and cut-outs based on local volume information. Features, such as the curvature or the distance to the viewpoint or a marker, are extracted and define the importance of objects or regions. The introduced approaches were initially designed for volume data but have been adjusted for geometry data. A level of sparseness approach, called importance driven volume rendering, was proposed by Viola et al. [121]. The introduced method aims at emphasizing important structures covered by less important regions by defining a level of sparseness to each structure. By means of compositing, more important structures are visible through less important ones.

Illustrative rendering and emphasis techniques as well as focus and context visualizations have been further investigated for medical datasets for example by Tietjen et al. [111]. The authors presented an illustrative hybrid rendering approach for medical datasets including a combination of volume, surface, and silhouette rendering. Tietjen et al. showed that the implementation of silhouettes to indicate the context object is appropriate for surgical planning and facilitates spacial perception. Ropinski et al. [92] used volumetric lenses to define cut-out regions within volumetric datasets in order to achieve efficient data exploration for medical diagnosis. The introduced lenses define regions in which rendering styles change, such as from volume rendering to silhouettes. A GPU-based multimodal visualization framework for neurosurgical planning was proposed by Diepenbrock et al. [25]. The authors integrated fiber rendering in a multi-volume raycaster and encoded uncertainty through less saturated line renderings. Gasteiger et al. [33] introduced a focus and context approach, the *FlowLens*, for hemodynamic attribute visualization in cerebral aneurysms where illustrative streamlines provide insight into the blood flow within the aneurysm.

8.4 The *BundleExplorer*

In the following section, the *BundleExplorer* is introduced as a focus and context rendering technique for fibers in combination with their encompassing hulls. The applied color codings for fiber rendering are proposed in the beginning of this section. In addition two interesting fiber-bundle conditions have to be distinguished: inner-bundle aspects and intersecting-bundle aspects. Inner-bundle visualizations consider fibers within their encompassing hull whereas intersecting-bundle visualizations are designed to highlight the relation of two crossing neuronal pathways.

8.4.1 Fiber color codings

Besides the conventional directional color encoding and the previously introduced functional colormapping using the ISMI, a further colormapping is included in the *BundleExplorer*: Spatial information of fibers within their encompassing hull is revealed due to distance information. The idea is to color the streamtubes according to their distance to the fiber hull. Distances are computed either to the encompassing hull or a certain geometry, such as a second fiber bundle. The fragment shader is used to visually encode the interpolated fiber distance information. The colormap indicates fiber parts in the vicinity of the hull in red and far away regions in white. Figure 8.1 shows the introduced color codings for inner bundle visualization in combination with a view-dependent bundle cutaway.

8.4.2 Inner-bundle visualizations

Inner-bundle visualizations facilitate fiber exploration while providing an understanding of the global bundle shape. Cutaway techniques aim to facilitate insight into an object by clipping parts of the context object or adjusting its transparency. Here, this results in clipping parts of the hull geometry in order to reveal underlying fiber structures. Three different cutaway approaches were developed, including an either automatic or user-based definition of clipping
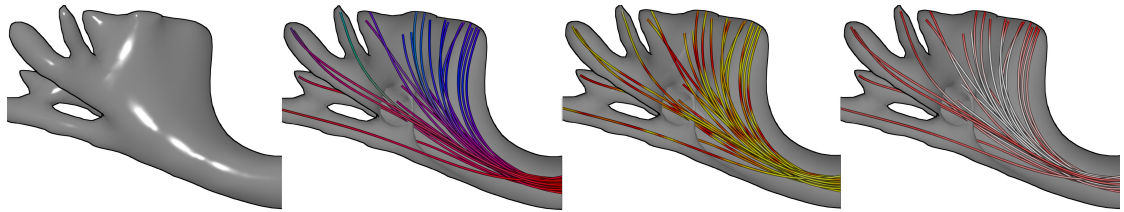
Figure 8.1: Visualization of fiber color codings: The fiber encompassing hull and view-
        dependent cutaway renderings reveal inner-bundle fibers. Applied fiber
        colormappings from left to right: Directional color coding, anisotropy color
        coding (yellow represents high and red low anisotropy) and distance to hull
        color coding (red indicates fibers in the vicinity of the hull).

regions. The marker-dependent technique applies a user-defined point of in-
terest and is view-independent. Contrarily, view-dependent approaches adapt
due to camera movement. Important spatial as well as functional fiber features
are visualized using the proposed color encodings.

Marker-dependent cutaway

A 3D coordinate determines the center for marker-dependent circular clipping.
The user defines a point on the hull's surface through a mouse click on the bun-
dle representation as indicated in Figure 8.2 in the bottom left part. This point
defines the origin of the circular hull clipping and the radius of the clipping
is adjustable through a slider. This information is transferred by uniform vari-
ables to the deferred shading pipeline stage in order to compute the binary 3D
masking texture. Figure 8.2 shows a visualization of the resulting marker-based
cutaway.

View-dependent cutaway

A further approach computes the cutaway based on the current view. In partic-
ular, the circular clipping origin is defined by the viewport center. The user can
adjust the radius and radial smoothness of the cutout with immediate feedback.
Results of the approach are illustrated in Figure 8.3.
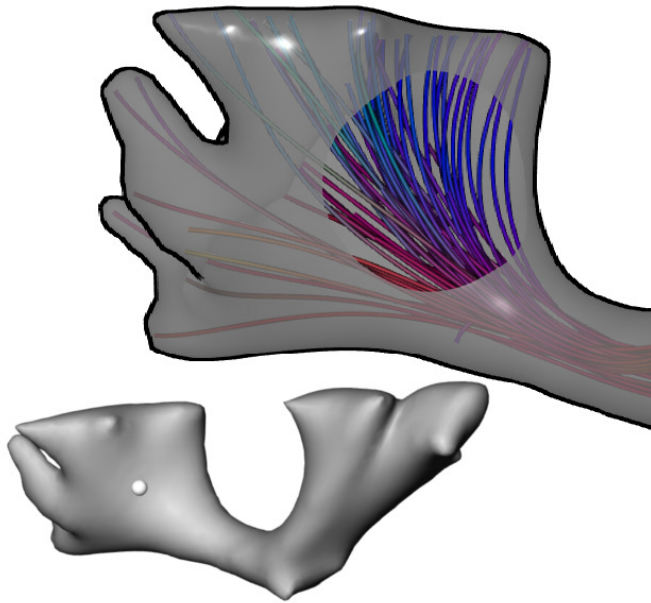
Figure 8.2: Marker-dependent cutaway visualization: The user places the marker coordinate (bottom left) and adjusts its radius which results in a circular cutout (top right).

The second view-dependent cutaway technique computes hull transparency with respect to the surface orientation. The idea is to enable a see-through for viewer-facing surfaces while providing context information. The dot product by the vertex normal and the view vector is used to estimate surface orientation. A user-defined threshold, implemented as a slider, is used to adjust hull transparency with respect to face orientation. Therefore, hull clipping results in a smooth opacity increase from regions facing the viewer to regions turning away from the viewer. Figure 8.4 displays a result of the approach for two different thresholds.

8.4.3 Intersecting-bundle visualizations

HARDI provides detailed information about the spatial relation of neuronal bundles. Two visualization strategies revealing bundle crossing characteristics were implemented. The basis for intersecting-bundle visualization approaches
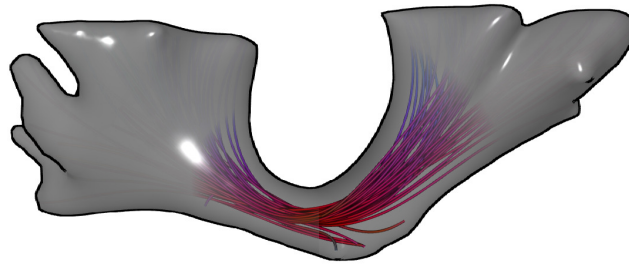
Figure 8.3: View-dependent cutaway visualization with respect to the viewport center: Hull cutout with applied radial smoothness with a small (left) and a large (right) radius.
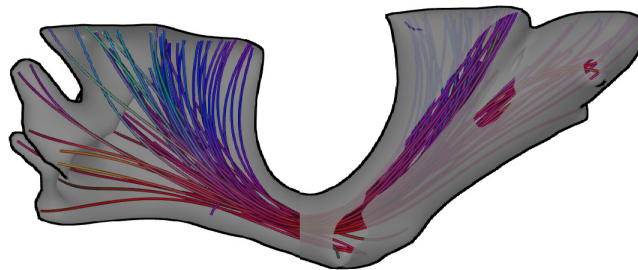
Figure 8.4: View-dependent cutaway visualization with respect to the view vector: Different thresholds are applied to facilitate a view of either the underlying fibers (left) or the hull (right).

is formed by two fibersets: The first bundle is represented using streamtubes and the second using a fiber encompassing hull.

Intersection marking

Color encodings and transparency adjustments to the hull's surface are used in order to highlight bundle overlapping areas. To accomplish this task, the fiber encompassing hull as well as the fiber geometry is rasterized in a first step to define overlapping regions. Afterwards, their intersections are transfered to the GPU via a 3D texture. Fragment colors as well as the transparency are adjusted using the fragment shader. Bundle overlapping regions are displayed as transparent in combination with an outline of the crossing area. Figure 8.5

shows results of the proposed intersecting markings for fibers running in the *centrum semiovale*.
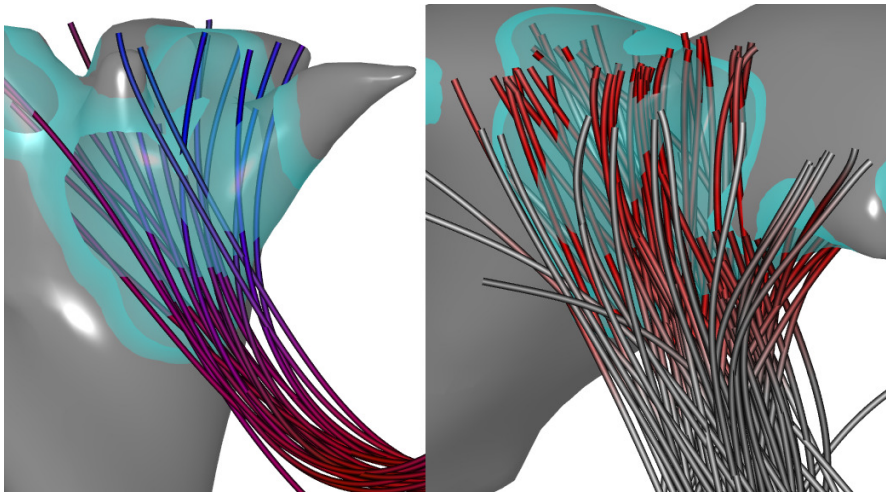
Figure 8.5: Intersection marking visualization: Individual bundles are displayed as streamtubes or fiber encompassing hulls. Intersections are transparent and overlapping boundaries displayed in light blue. Applied directional color coding for callosal fibers (left) and distance encoding of fibers of the pyramidal tract (right) are displayed.

Plane exploration

The plane exploration mode applies a 3D cutting plane for hull clipping. Arbitrarily cross-sectional cutouts can be defined by the user. A simple 3D interaction mode is provided in which the mouse is used to define plane rotation and translation. Bundle parts are divided by the clipping plane as either exterior or interior. According to this they are displayed as either transparent or opaque. The silhouette of the cross-section is displayed in yellow to provide additional spatial information. Figure 8.6 shows the focus and context visualization using the introduced cutting plane.

8.4.4 Workflow and implementation

Figure 8.7 shows an overview of the computation and interaction pipeline. First,
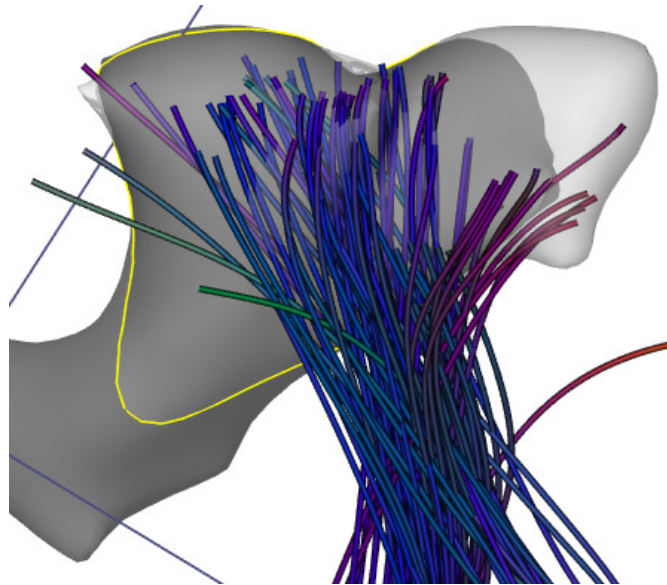
Figure 8.6: Plane exploration visualization: Bundle clipping is defined by an adjustable plane. The outline of the cross-section is displayed in yellow.

fibers are reconstructed based on a user defined seeding region. Afterwards respective hulls are computed. Fibers are first rendered using a line strip primitive. The subsequent shader pipeline is responsible for generating view-oriented triangle strips. The distance of fiber points to a geometry is computed in the next step for subsequent colormapping. The required geometry is either the corresponding hull of the first or the second bundle or any other geometry. Distances are computed on the CPU before fiber rendering using the winged edges meshes (WEM) representation for hulls. The distance to each WEM node is determined for each fiber point. Attribute variables are used to assign the shortest distance to the respective vertex of the line primitive. This information is accessible in subsequent pipeline stages.

The proposed visualizations are realized using a deferred shading approach. Two 2D parameter textures are computed: The first stores the geometry normals and the second combines necessary scalar information for further visualizations. The fragment depth is stored in the red channel, the marker-defined visibility of the hull is encoded in the green channel, and a flag for hull iden-
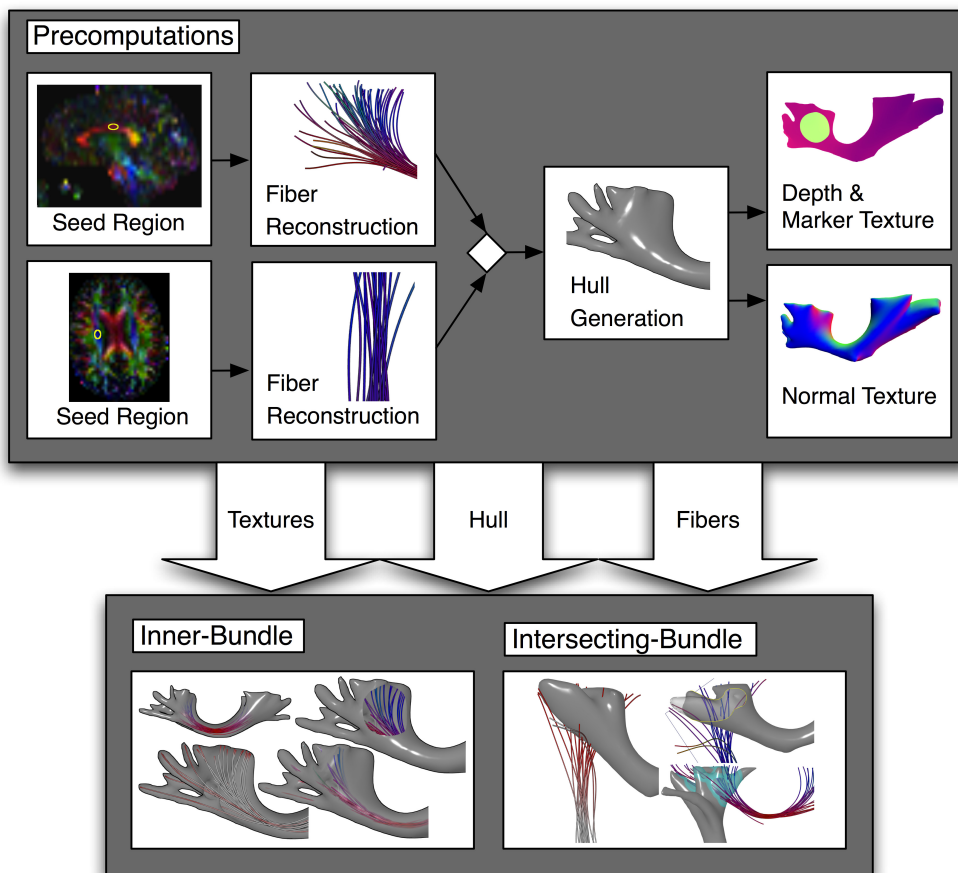
Figure 8.7: The *BundleExplorer* pipeline: Preprocessing steps are shown in the upper part and visualization approaches in the lower part of the illustration.

tification is stored in the blue channel. Additional texture inputs for subsequent compositing are offscreen renderings of the fibers and the hull. Predefined shader pipelines built upon these textures and compute the final cutaway views in an upcoming rendering pass.

Since visualizations are implemented as screen-space approaches, special care has to be taken for cutaway techniques. Here, cutaway renderings aim to reveal fibers as well as hull backfaces. The fragment shader has no information about the scene behind the cutouts. To deal with this correctly, hull backfaces are rendered in the course of the deferred shading approach and make use of

the according depth buffer in the compositing stage. In combination with fiber depth information depth values are compared in order to determine whether the current fragment belongs to the hull or a fiber. The left part of Figure 8.4 shows correct hull backface and fiber rendering.

8.5 Results

In the following, results of the proposed algorithms are presented and discussed. Performance evaluation was accomplished on a Core2 Duo, 3.16 GHz with 4 GB RAM and a NVIDIA GeForce GTX 285 graphics card.

Inner-bundle visualizations provide information about underlying fiber features such as directionality, tightness, anisotropy or distance to the encompassing hull. Applying color encodings to inner-bundle fibers reveals this spatial and functional information. Figure 8.1 shows inner-bundle visualizations in combination with a view-dependent cutaway. In the rightmost part, one can clearly identify fiber compartments close to the hull (red). This information is not obtained by simple directional color coding but is important for determining bundle forming fibers. If parts of the hull are subject to clipping the vicinity of fibers to the hull is estimated through distance color coding. The uncertainty of fiber tracts is a well-known issue in diffusion visualization. The presented inner-bundle characteristics visualizations provide essential information about the reconstruction reliability such as the degree of anisotropy in a certain bundle part. Examination of challenging regions, such as fiber crossings, is feasible through cutaway renderings. In the case of falsely detected fibers, regardless of whether they are of less certainty or belong to a different bundle, they can be removed from the bundle and hulls be recomputed. For a 1024×1024 screen resolution, intra-bundle visualizations are carried out at approximately 80fps.

Intersecting-bundle visualizations are beneficial for bundle crossing examination. The proposed intersection marking approach highlights bundle overlappings which facilitates spatial understanding. Bundle subsets are displayed as transparent within the plane exploration mode. Thereby, insight into regions of interest, such as interwoven bundles, is provided. Distance encodings are

also interesting in intersecting-bundle visualizations. Here, they are applied to reveal the spatial relation between two reconstructed neuronal pathways. Figure 8.8 shows two different views for two intersecting bundles with applied distance fiber coloring: The distance between the fiber and the hull in the right part is observed. However, in the left image the distance is only accessible through color coding. Since the distance assigned to each fiber vertex can be computed
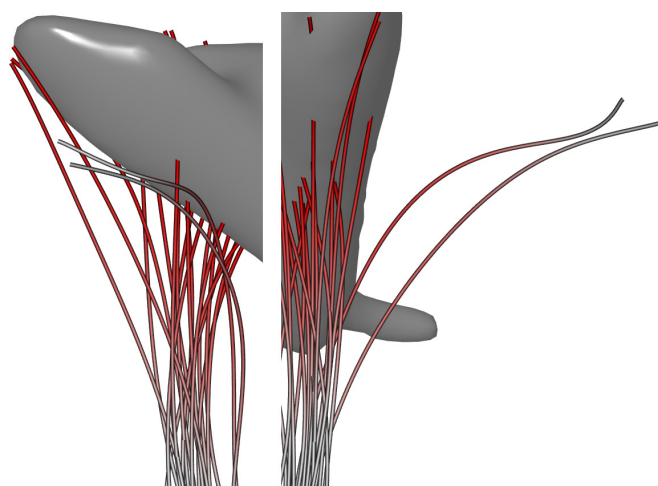
Figure 8.8: Distance visualization of two intersecting fiber bundles: Distance encoding reveals fiber parts far away from the bundle (left), which is proved by scene rotation (right).

from any provided geometry, further scenarios are feasible. For example tumor boundaries are very interesting since spatial relations of neuronal pathways to a lesion are crucial in preoperative planning. Intersecting-bundle visualizations run at approximately 110fps.

8.6 Discussion

Advanced focus and context rendering approaches for complex fiber distributions were presented in this section. They are applicable to diffusion data visualization in general, but specifically focus on problems related to HARDI. The main challenge for HARDI-based fiber visualizations is to consider the visual clutter caused by the intricate nature of neuronal pathways. Conflicting inter-

ests in terms of diffusion visualizations exist. Hulls are beneficial in order to hide unnecessary line complexity. However, lines are preferred in some cases since they reveal areas of dense fibers as well as local fiber features. Furthermore, crossing fiber areas can be identified through line representations. In the presented approach both techniques are combined in a user-friendly and intuitive visualization framework and as a result, advance towards complex diffusion data examination.

The introduced *BundleExplorer* framework include different cutaway techniques. Further approaches are feasible, such as a feature-based technique: Considering anisotropy classifiers, cutout regions of the hull can be identified through interesting intra-bundle regions such as low anisotropy or crossing fiber pathways. The proposed GPU framework facilitates an easy integration of focus and context rendering approaches. Additional visual enhancements can be integrated in order to further facilitate spatial understanding of line configurations. For example, an illustrative rendering technique for dense fibers was introduced by Everts et al. [29]. The authors applied depth-dependent halos to emphasize dense line data. The integration of this approach enhances line interpretation in terms of large fiber bundles. The presented method can further benefit from bundle feature visualization through texture mapping. Eichelbaum et al. [26] proposed a line integral convolution (LIC) motivated texture visualization for neuronal bundle surfaces which provides tensor analysis. Chapter 7 presented an intra-bundle raycasting approach which colors the tract surface according to inner diffusion characteristics.

Part V

Clinical application

9 Multimodal visualization for neurosurgical planning

9.1 Overview

Previous chapters proposed methods in order to classify, reconstruct, and visualize diffusion data. In fact, diffusion data visualization has gained strong interest in preoperative neurosurgical planning because the location and course of neuronal pathways is crucial to avoiding postoperative damages. However, it is still not considered as an examination routine in all clinical environments. For this reason, the following part is dedicated not only to discussing diffusion imaging's contributions to neurosurgical planning but also considering the contributions of visualization techniques in general. A motivation as well as scientific questions are provided in Section 9.2 followed by a literature study in Section 9.3 and an introduction to the multimodal data in Section 9.4. The developed multimodal visualization approaches are presented in Section 9.5 and methods for access path definition, visualization and evaluation in Section 9.6. A workflow is introduced in Section 9.7 and the results in Section 9.7.4. This part closes with a discussion of the developed methods in Section 9.8.

9.2 Introduction

In the living brain, vital structures include functional areas as well as the fiber bundles connecting these areas. If pathologies, for example a tumor, are present and derogate essential functions, neurosurgical treatment is needed. Neurosurgery is tailored to patient specific anatomy and pathology. Hence, the most adequate access path to a lesion is defined within an individual preoperative

planning phase. This is mandatory with respect to deep-seated structures or lesions close to essential white matter tracts, such as in the CST or related functional activation zones; it is crucial to minimize the damage of these structures at risk.

The visualization of patient-specific anatomical, functional, and pathological structures enhances the treatment planning of surgical interventions. As a result, multiple modalities have to be acquired. In neurosurgery, major acquisitions include fMRI, to define activation areas; DTI, to reconstruct neuronal pathways; and T_1-weighted and T_2-weighted MRI sequences, for anatomical information. Multimodal approaches combine these datasets into one visual representation. The embedding of brain properties in their anatomical context offers vital insights into preoperative imaging. Computer graphics techniques such as visual enhancements, annotations, and access path visualizations support the surgeon in identifying risk structures and therefore improve the planning phase. In surgical planning applications, interaction, in terms of visualization adjustments, is beneficial. However, one has to keep in mind that it forms an additional task for the surgeon.

A visualization approach, combining several modalities with an intuitive planning unit is a challenging task. The main questions in terms of neurosurgical planning are:

- How can the multimodal data be visualized in order to facilitate both an exploration and three-dimensional perception?

- How can risk structures as well as their spatial and functional relations be revealed?

- How can an effective interaction for neurosurgical intervention planning be realized, including access path definition, visualization, and evaluation?

The developed volume clipping approach called *Cavity Slicing* provides an intuitive exploration method for multimodal data. Potential adjustments to slicing include changes in either the cutting geometry or the position, which are

either view-dependent or view-independent. As a result, structures are visualized within the surrounding tissue. Considering the slicing geometry as the access path and adjusting the cutting depth towards the tumor enables an intuitive examination of the structures along the path. Fiber filtering is used to define meaningful fiber subsets: Neuronal pathways associated with specific activation areas or the tumor, or fibers crossing the access path, are extracted. The visualization and evaluation of access paths is enhanced in order to provide a better understanding of attributes such as length and spatial arrangement. Computer graphics techniques are applied to encode the structure's distance to the path. The evaluation of different access paths against each other is simplified since an iteration through defined paths is possible with adaptive distance encodings. In the last part, a workflow for intervention planning using the introduced methods, is provided.

The IEEE Visualization Contest 2010 [1] targeted multimodal visualization for preoperative neurosurgical planning and was the inspiration for the presented work. The presented planning tool and multimodal visualization approaches were published in [97] and [98].

9.3 Related work

Preoperative planning in neurosurgery is an active field of research [12, 91, 107, 108]. In multimodal visualizations, one powerful way to highlight inner structures are cutting techniques. Beyer et al. [10] introduce a planning application including a multi-volume raycasting approach which applies a view-dependent skull peeling that removes parts of the volume obscuring structures of interest. Clipping tools define a cut-out geometry and represent a common technique to extract inner structures [47, 60]. The identification of fiber pathways connecting functional areas is crucial in neurosurgical planning. Talos et al. [110] examined the combination of DTI and fMRI data and thereby correlated fiber tracts to cortical areas. Several approaches for a combined visualization exist [41, 53]. Fiber selection methods [11, 12, 61] result in a fiber subset that cross a specific region. The winning entry of the visualization contest [24] introduced a surgery

planning tool including an exploration and an in-detail inspection step similar to the steps presented in this work. In the exploration section, the surgeon examines the multimodal data in a 3D, contextualized view and define an initial access path. The authors introduced a so called tumor map, which reveals the distances of risk structures to the tumor. In the second part the chosen access path and the related structures is examined in greater detail. Another honorable mention submission of the IEEE Visualization Contest 2010 [13] presented a planning approach including distance measurements between the tumor and structures at risk as well as focus and context rendering approaches to facilitate orientation.

9.4 Neurosurgical datasets

Different acquisition schemes represent different structures of interest in neurosurgical planning. Neuro-visualizations have to combine these datasets to provide meaningful representations. In this approach, datasets provided by the IEEE Visualization Contest 2010 [1] were used. The first case contains MRI data of a patient with an intra-cerebral metastasis and case 2 a glioma, which is much more challenging with respect to the neurosurgical situation.

Conventionally, the first step in multimodal visualization is the registration of the various datasets to achieve a spatial alignment. However, image registration was not the focus of this research. All of the data sets had previously been linearly co-registered to the T_1 reference dataset by the contest initiators. Thus, the presented approaches assume preregistered data. All of the data were acquired on a Siemens 3T Verio MR scanner and are courtesy of Prof. B. Terwey, Klinikum Mitte, Bremen, Germany. The available sequences contain anatomical images as well as functional and structural images which are discussed in the following.

9.4.1 Anatomical data

T_1- and T_2-weighted as well as fluid attenuated inversion recovery (FLAIR) volumes are considered as anatomical volume data since they display the anatomic

properties of the brain in great detail. The resolution of the T_1 volume is $1mm^3$. In addition to the T_1-weighted data, a contrast enhanced sequence was available. Both, enhanced and non-enhanced data, have been corrected for MR intensity inhomogeneities and are of the size $512 \times 512 \times 176$. Furthermore, a brain- and tumor mask is provided on the T_1-images as a segmentation result. FLAIR is popular in brain imaging to suppress *cerebrospinal fluid* (CSF) effects in images. FLAIR sequences supplement conventional MRI images in terms of diagnosing intracranial tumors [115]. It usually provides better definition between the perifocal edema and the tumor than T_2-weighted sequences. FLAIR volume, as provided by the IEEE contest, was utilized comprising a resolution of $0.45mm^2 \times 6.0mm$ and size $432 \times 512 \times 42$.

9.4.2 Functional data

Functional data was acquired by fMRI, which is able to identify cortical areas associated with a given task, such as finger-movement, verb-generation or language processing. It plays a major role in identifying patient-specific vital functional areas. In this case, finger tapping was the performed task. The sequence starts with ten volumes associated with activation followed by ten at rest. Five cycles were performed to obtain all in all 100 volumes. The fMRI data with a resolution of $3.0mm^2 \times 3.3mm$ were motion-corrected and analyzed using a general linear model. An additional statistical parametric map (t-map) of $64 \times 64 \times 64$ was provided in the data containing the evaluation of the fMRI data.

9.4.3 Diffusion data

DTI volumes are $128 \times 128 \times 72 \times 62$ in size and consist of one b_0 image followed by 30 diffusion gradient images were used and the number of excitations (NEX) counts two. The b-value was 1000.

9.5 Multimodal visualization

In order to implement a neurosurgical planning tool, the first step is to answer the question of how the multivalued data can be combined efficiently. Computer graphic techniques such as focus and context renderings or cut-out techniques are a good possibility and are introduced subsequently.

9.5.1 Data preprocessing and arrangement

In the following, each of the individual data is presented and the preprocessing and rendering explained.

Vessel and edema

The following section explains the consecutive steps for vessel extraction. The basis forms the T_1-weighted dataset, where the vascular structures are enhanced by a contrast agent. This dataset is subtracted from the T_1 image without contrast enhancement, similar to digital subtraction angiography (DSA). As a result, the vascular structures are highlighted. To exclude neck vessels and focus on larger vessels located at the cortex, the subtracted image is masked with the enlarged brainmask. For further improvement the vesselness filter proposed by Sato et al. [103] is applied. The filter calculates a multi-scale vesselness measure as a function of the Hessian matrix. Each voxel in the output volume indicates how similar the local structure is to a tube. The actual segmentation is performed by a region growing algorithm. Table 9.1 gives an overview of the steps for vessel segmentation and the computation time.

Preprocessing step	Timings in seconds
T_1 contrast enhanced subtraction	2
Brainmask dilation	103
Vesselness filter	22
Region growing	1

Table 9.1: Data preprocessing: Steps and timings for vessel segmentation.

The perifocal edema has been extracted from the FLAIR volume using a region growing algorithm.

Neuronal pathways

Diffusion imaging is able to extract white matter pathways using tractography techniques, as discussed in Part III. HARDI is considered to be more precise than DTI; however, at this time not clinically feasible due to its long acquisition and reconstruction time. In the presented case, only DTI sequences were available. For the reconstruction of neuronal pathways a tractography implementation of the algorithm, proposed by Lazar et al. [57] was used. A whole brain fiber reconstruction was performed in which all voxels above a specified FA value are considered as seed regions.

Cortex and tumor

A segmentation of the cortex and tumor boundary is provided in the contest data. The segmented cortex information was used to mask out the brain from the T_1-weighted image. The respective transfer function was adjusted to highlight the gyri and sulci of the cortex.

Data arrangement

The acquired and segmented data was arranged in two groups: volumes (T_1- and T_2-weighted MRI, activation areas, and cortex) and surfaces (fibers, tumor, core activation areas, vessels, and edema). The volume data (T_1- and T_2-weighted MRI, and cortex) is considered as anatomical information and the surfaces (fibers, activation areas, and vessel) as potential risk structures. The anatomical data is clipped using a slicing volume, whereas enabled surfaces are never cut away.

9.5.2 Visualization of anatomical and functional structures

Volume visualizations are performed using a direct volume rendering MeVis-Lab module, called *Giga Voxel Renderer* (GVR) [58]. All isosurfaces are gener-

ated with a *Marching Cubes* [59] based approach and internally represented as winged edge meshes. Vessels are red, the tumor purple, and the edema displayed in pale lilac.

Activation areas

A visualization of activation areas is possible through volume as well as isosurface rendering. Isosurfaces, which reflect motor activity, are generated by applying a threshold to the given t-map. This threshold defines the core activation areas (yellow) and is adjustable by the expert. Volume rendering of the t-map shows the extended activation zones. For this reason, color appearance and extent depend on the selected transfer function and are defined in the color range from yellow, which indicate core activation areas, to red. This is considered as an uncertainty visualization for fMRI since the differentiation between core activation (isosurface) and less intensive activation (volume rendering) is provided. Furthermore, it is possible to mark the most relevant activation zones (isosurfaces) for intervention planning. The following measurements and filtering methods are only performed on the selected parts.

Harming regions, represented by activation zones or neuronal pathways connecting these areas, might cause damage in the respective functionality. Therefore, experts define a safety margin surrounding core activation areas in order to indicate a region that must not be interfered with during surgery. This margin is also seen as a visual aid when setting relevant access paths to the tumor.

Neuronal pathways

Fiber filtering defines meaningful subsets out of a complete brain fiber reconstruction. Subsets are extracted by either the application, depending on the inquiry or manually by the user. Automatic fibersets include either fibers crossing activation areas, selected subsets, the tumor, the critical region surrounding the tumor or the access path. Figure 9.1 shows two results of the fiber filtering approach.

A fiber filtering with respect to the selected path is displayed in Figure 9.5b. In addition, structures, not defined by MRI, are filtered by a user-defined volume

<div align="center">(a)   (b)</div>
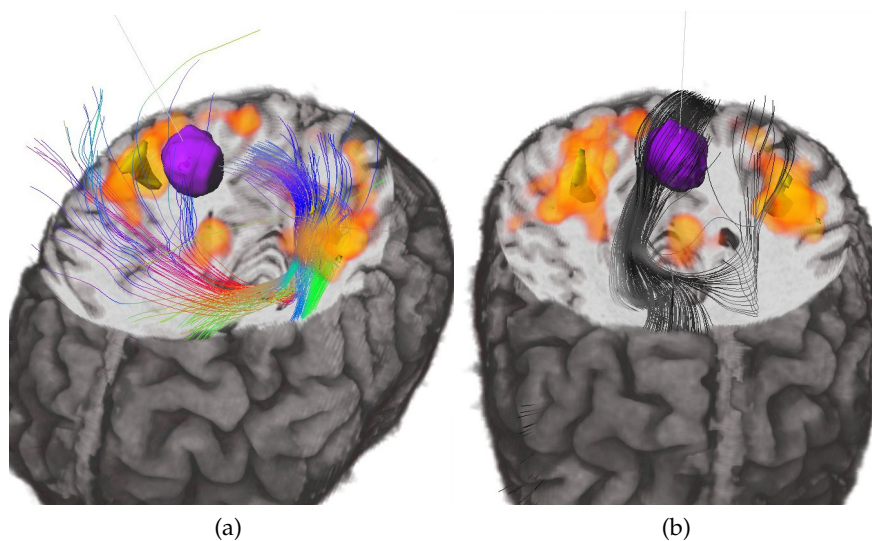
Figure 9.1: Risk structure examination: View-independent *Cavity Slicing* with a large radius and no smoothness. Tumor, t-map volume and core activation are rendered. Fiber filtering with fMRI core activation (9.1a) as well as tumor crossing FA-value color coded fibers (9.1b) are depicted.

of interest (VOI). All selected fiber subsets are displayed at the same time or the user enables a specific selection. Each of these are adjustable in their respective color in order to distinguish between different subsets.

Visual clutter is a well-known problem in terms of fiber rendering: Streamline interpretation quickly become difficult due to missing depth information and the often overwhelming amount of lines. In addition, individual streamlines are sometimes of minor interest in neurosurgical planning [73]. It was therefore decided to hide this complexity using a fiber encompassing hull, illustrated in Figure 9.4. The hull generation forms a three-dimensional hull around related fibers and provides a more intuitive spatial perception.

9.5.3 Multimodal visualization

Multimodality is crucial for neurosurgical planning since vital structures of the brain are represented within different datasets. This data has to be combined in a single visual representation to provide efficient neuro-visualizations. It is nec-

essary to fade out regions of less importance in order to enable an insight into deep-seated structures. This is achieved by either clipping parts of the covering volume or adjusting its transparency to enable a see-through. Variations of both are possible within the here presented approach.

Rieder et al. [91] cut out a cavity as a clipping geometry between the point of interest (POI), the tumor center, and the incision point. This concept was modified in terms of view vector alignment and the shape of the cut-out geometry and is hereafter referred to as *Cavity Slicing*. The clipping is only applied to the anatomical volume. As a result, enabled risk structures between the POI and the skull remain visible. To minimize necessary definitions made by the user, the slicing volume has the following initial settings: The orientation of the clipping geometry is aligned with the view vector which enables an exploration of structures from each point of view while panning around the head. The user can freeze the orientation if an appropriate angle revealing structures of interest is found. By moving the camera slightly, an improved depth perception is achieved: The camera is independent from the clipping orientation and the shape of the slicing geometry becomes comprehensible. In addition, the surgeon is able to define the clipping volume in terms of radius, depth, and radial smoothness, as displayed in Figure 9.2. Figure 9.3 shows different settings of *Cavity Slicing*. The initial depth is defined by the tumor center since deeper structures are of less importance. The depth of the geometry is adjustable by the expert for further exploration. A large radius results in a plane-like clipping of the anatomical volume and is beneficial within the exploration stage; whereas a small radius cuts out a tube shape and restricts the visualization to structures lying between the tumor center and its projection to the skull. Similar to the approach presented by Rieder et al., this is considered as an access path visualization. The smoothness parameter defines the radial gradient of the clipping geometry. It results in a transparency adjustment of the cut-out region of the anatomical volume. The defined clipping geometry results in a masking volume, which is applied to the anatomical volume through GVR options.

The opacity modulation is an implementation of the level of sparseness approach, which was introduced by Viola et al. [121]. The proposed method aims to emphasize important structures covered by less important regions by defin-
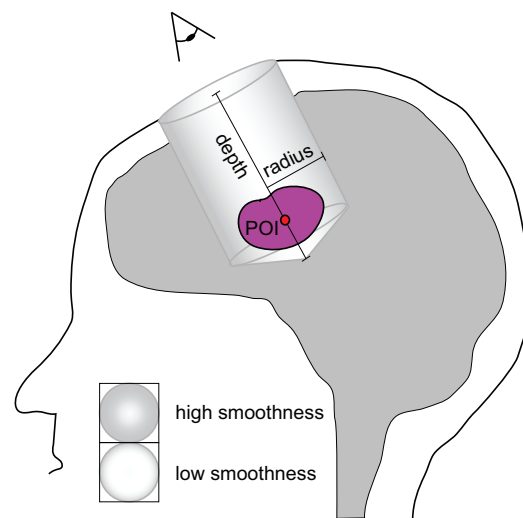
Figure 9.2: Setup of *Cavity Slicing*: The geometry is adjustable in radius, depth, and smoothness.

ing a level of sparseness to each structure. By means of compositing, more important structures become visible through less important ones. Hence, tuning the transparency of regions is one way to visualize the level of sparseness. Adjustments to the clipping geometry are considered as modifications concerning the importance of the relevant structure. It is possible to examine structures of interest in their anatomical context using this technique.

9.5.4 Risk structure evaluation

It is essential to identify structures at risk for the subsequent neurosurgical intervention during a preoperative planning phase. Functional information and the spatial relation of these structures is vital. It is advantageous to gain more information about these structures and their relation which are presented in the following.

<div align="center">(a)   (b)   (c)</div>
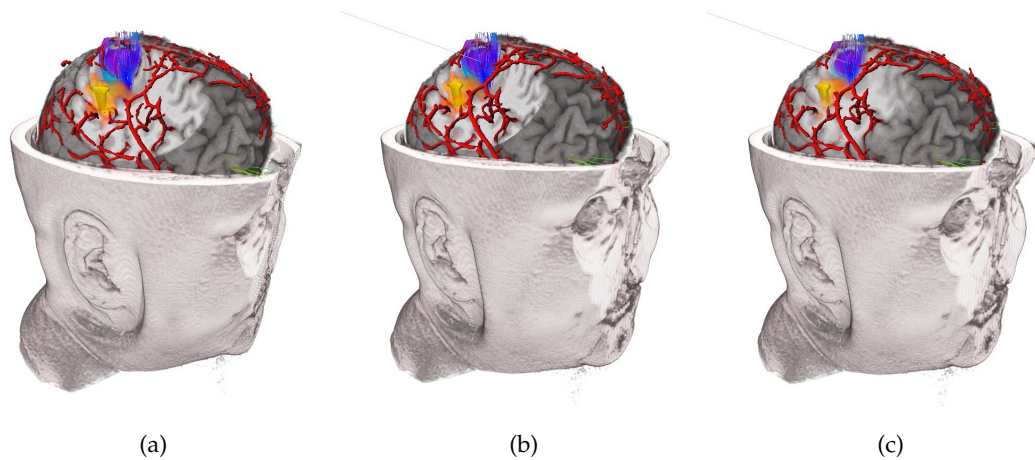
Figure 9.3: Examples of *Cavity Slicing*: The Tumor, vessels, tumor crossing fibers, the t-map volume, and core activations are displayed. View-dependent clipping without smoothness (9.3a) and view-independent geometry position (9.3b) are feasible. The gray line in the view-independent clippings represents the view vector of the frozen clipping.

Distance measurements

The shortest distance from the tumor boundary to a chosen structure at risk, such as vessels, neuronal pathways or activation areas is vital for neurosurgical planning. Furthermore, all minimal distances from the access path to risk structures are calculated. An arrow is displayed in the respective view as a visual aid. The exact length is displayed below the main window. Moreover, it is possible to compute the shortest distance to a whole structure or just a subselection. The selection is defined by the user by marking a region on the structure with a lasso tool.

Distance enhancements

Two enhanced color codings are provided besides the introduced distance measurements: Color enhancements are mapped on the vessels' or wrapped white matter tracts' surfaces using a shader program. In the first approach, the color of the structure fades to black, depending on the distance to the chosen access

path. Parts located close to the access path are fully saturated in the respective color, hence the attention is focused on essential components. The length of the color gradient is adjustable by the user. The second approach uses colors to indicate distance steps in millimeters, from red to yellow, as displayed in Figure 9.4.
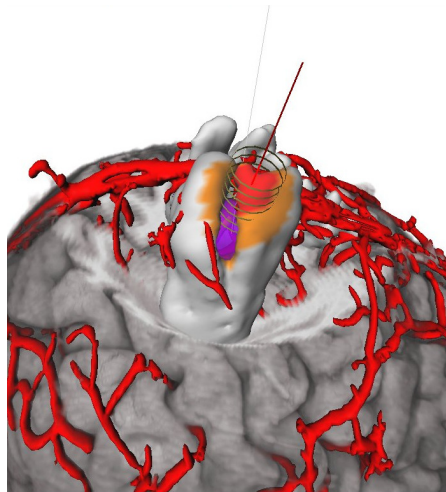
Figure 9.4: Visual distance enhancements: Tumor, vessels, and *Cavity Slicing* of the anatomical volume in combination with hull rendering of path crossing fibers with distance to path color coding.

An analog color coding technique has been employed for individual fibers. They are displayed in colors which encode the distance to the center of the tumor. The color varies from white, close to the lesion, to black, far away.

Fiber tract information

Several fiber tract statistics are displayed in order to provide a detailed fiber examination. The number, minimum/average/maximum length as well as the FA-value is shown for a current fiber set. The coloring of fiber sets is adjustable to represent the FA value, which is encoded in grayscale in order to highlight the integrity of neuronal pathways. An example is shown in Figure 9.1b. A FA-value of zero represents low directional information and is encoded in black, whereas a high FA-value is encoded in white.

9.6 Intervention planning

The next step in a neurosurgical planning procedure after multimodal visualization is the definition of the actual access path. Here, three steps are essential: access path definition, visualization, and evaluation. Contributions to each stage are introduced in the following.

9.6.1 Access path definition

An access path to the lesion is defined by an incision point on the skull and the center of the tumor. The brainmask is displayed as slightly transparent in order to define the access path. As a result, the user has an idea of the brain's surface in combination with previously defined risk-structures. The incision point for the intervention is defined on the brainmask by clicking the mouse.

9.6.2 Access path visualization

In conventional planning tools, the path between the lesion and the incision point is represented by a simple line. Disadvantages of this visualization are weak depth perception and information loss if the path is hidden by various structures. However, access path visualization is enhanced in several ways. Structures lying within an access path present an essential condition for planning a neurosurgical intervention. Nevertheless, the length is a crucial attribute of a potential path as well. Besides displaying the length of the chosen path in millimeters, the line representing the path is mirrored on the head's surface: The line is elongated by the distance from the center of the tumor to the incision point. Both parts are colored in red but differ in saturation to indicate the incision point. As a result, the user has always an idea of the length and orientation of the possibly hidden access path. Tubes surrounding the part lying inside the head are added since the spatial orientation of a line in 3D is ambiguous. The tube is divided into a number of rings with a custom separation and radius in order to provide a visual idea of the path length. Figure 9.5 illustrates the path specific visual enhancements. Additionally, adjustments to the rings are beneficial in terms of identifying and positioning risk-structures. Enlarging the rings
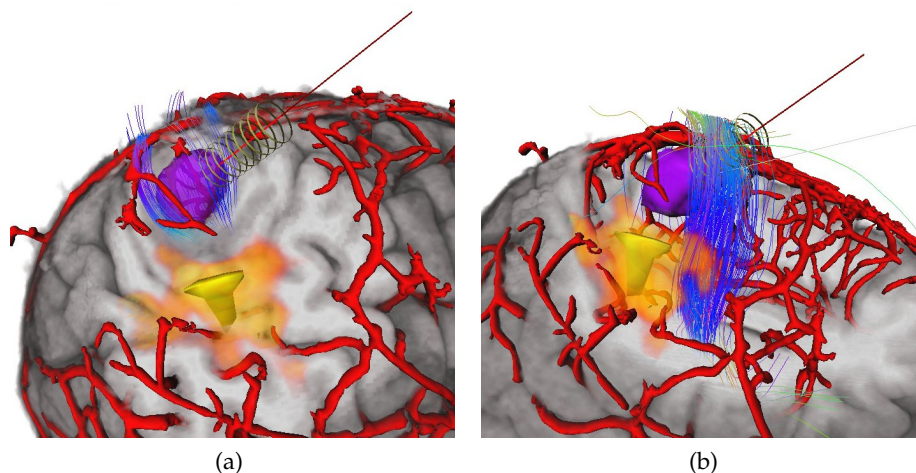
Figure 9.5: Path visualization: Tumor and vessel with t-map volume and core activation rendering. *Cavity Slicing* applied to the anatomical volume with low smoothness. Visual enhancements facilitate the understanding of the spatial position of the path (9.5a) and fiber filtering provides path crossing fibers (9.5b).

reveals adjacent structures that may not be touched during the intervention, such as functional areas.

9.6.3 Access path evaluation

The surgeon is able to place markers, which indicate potential access path entry points. All path-related visualizations and evaluations, such as distance colorings, measurements or fiber filterings, are automatically adjusted to the currently selected path. As follows, the user can easily switch between the defined paths and compare them with each other. *Cavity Slicing* enables to focus on structures directly surrounding an access path.

9.7 Workflow for surgery planning

In the following, an analysis workflow for neurosurgical planning using the presented methods is proposed.

9.7.1 Exploration stage

The individual patient status is provided in the exploration stage using the 3D visualization of anatomical and functional structures. In particular, the location of the lesion is of major importance and anatomic and functional structures have to be examined with respect to their spatial relation. *Cavity Slicing* (view-dependent and view-independent) is especially helpful at this stage since it reveals structures in their anatomical context. Fiber filtering is beneficial to reveal important fiber subsets: For example, those passing fMRI activation areas or the lesion. The exact location of core activation areas through fMRI is accompanied with uncertainty. Therefore, functional areas are extracted through volume renderings of the t-map with a user-defined transfer function. DTI representations incorporate uncertainties regarding the integrity of fibers. Enabling the FA-based color coding provides insight into fiber integrity; and as a result, anatomical and functional properties are explored regarding specific clinical questions.

9.7.2 Surgery planning stage

After an initial exploration of the data, the actual surgery planning takes place: the definition of possible incision points and thereby access paths. Distance measurements are applied to further enhance the spatial understanding of the data, for example the position of risk-structures with respect to the tumor. Potential infiltrations of vital fiber tracts by the lesion are detected through fiber filtering and color encodings. Labels for the entry point are defined in order to indicate different access paths.

9.7.3 Evaluation stage

The defined paths are examined in the evaluation stage by switching between the markers. Adjustments to the path encompassing rings are a visual aid in evaluating distances of adjacent risk-structures. Distance color encodings on fiber hulls provide information regarding critical regions during surgery. Information about deep-seated structures along the access path is crucial in neu-

rosurgery. Therefore, the approach includes adjustments to the radius and the smoothness of *Cavity Slicing* for path evaluation. If the user constantly increases the depth of the clipping geometry while passing risk-structures along the way to the lesion, an understanding about the actual opening is provided. A new patient dataset requires individual settings such as transfer function or tractography adjustments. For this reason, the program includes the option to define and save presets: An assistant defines appropriate parameters for further investigation and treatment planning to be performed by the surgeon. Furthermore, presets are a very convenient way of dealing with complicated cases where further expert reports are needed. As a last step in neurosurgical planning, a preoperative *Surgical View* is presented which provides an impression of the actual intervention. This is a meaningful contribution in order to finally relate the planning to the actual intervention. To accomplish this task, the camera view vector is defined as identical with the final access path. The view is frozen along this direction and the head is rotated as in the surgery. An example for the *Surgical View* is displayed in Figure 9.6.
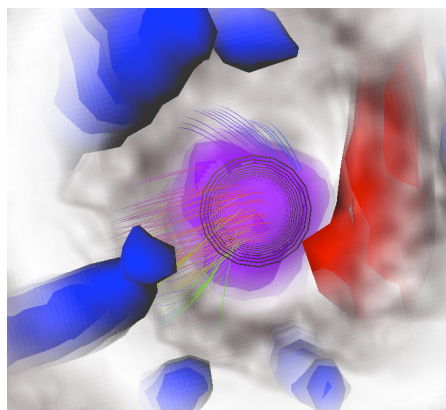
Figure 9.6: *Surgical View*: Hulls of activation area crossing fibers, access path crossing fibers, vessels, and the tumor are displayed. *Cavity Slicing* is applied with a small radius, little smoothness, and a depth value smaller than the location of the tumor.

Afterwards, the user adjusts the radius and the smoothness of the *Cavity Slicing*. By constantly increasing the depth of the clipping geometry, one gets an

impression how the opening appears while passing risk-structures along the
way to the lesion.

9.7.4 Performance

The stated visualizations run with interactive frame rates. Table 9.7 provides an
overview of the frame rates on a Core2 Duo, 3.16 GHz with 4 GB RAM and an
NVIDIA GeForce GTX 285 graphics card. For evaluation purposes, the rendering was rotated by 360 degrees. The viewport size was 512×512.

Visualization	fps
T_1: plane slicing, cortex: view-dependent *Cavity Slicing*	15
+ tumor, vessel, tumor crossing fibers	10
+ fMRI(core activation, t-map volume rendering)	9
+ wrapped tumor crossing fibers	9
+ smoothed *Cavity Slicing*	9

Figure 9.7: Frame rates of multimodal visualizations: Volumes with their according renderings and resulting overall frame rates are depicted.

9.8 Discussion

State of the art as well as novel exploration approaches for multimodal visualizations in neurosurgical planning were developed and discussed in this chapter. Additionally, interaction methods which aim at supporting the surgeon in identifying risk structures and defining an appropriate access path to the lesion were introduced. Parts of the discussed work were presented in the IEEE Visualization Contest 2010 and was rated second as well as received an *Honorable Mention Submission* title. In the course of the contest review, two neurosurgical experts evaluated the presented prototype in terms of multimodality, quality of visualization, interaction, and clinical value. Clinicians deemed the tool as be-

ing very good from a practical and applicable point of view. Data exploration as well as risk structure identification was rated as having a high practical value as well as improving current techniques. However, uncertainty visualization for DTI and fMRI was not considered sufficiently. *Cavity Slicing* seems to pose a real contribution to current exploration tools for multimodal datasets. Both view-dependent as well as view-independent clippings were considered as beneficial in neurosurgical planning. The overall clinical value and recommendation was rated as very good.

Computer graphics techniques enable multimodal rendering, enhance the appearance of the risk structures and encoding essential information for surgery planning. However, 3D visualizations are still not common in routine clinical examinations and intervention planning: Many surgeons still mentally fuse the multivalued data in order to obtain a spatial perception of the intervention, which comprises several issues: First, it requires extensive knowledge in terms of anatomy and modality as well as several years of training. Second, neglecting the fact that the data is inherently 3D and the spatial relation of the structures is crucial, can lead to severe misinterpretations. In many cases 2D projections are used, including axial, coronal, and sagittal slices resulting from CT or MRI acquisitions. However, these projections are unable to properly highlight 3D constellations.

The access path planning stage is, same as the exploration stage, still subject to mental fusion in some clinical environments. However, a preoperative view which considers potential access paths as well as related risk structures, reduces the probability of postoperative damage. In addition, knowledge about potential surgical approaches is also beneficial for decision making within the OR. The integration of preprocessed data through a navigation system provides the linkage between preoperative planning and the actual intervention. Furthermore, overlays within the OR microscope highlight risk structures during the intervention.

For all these reasons, a holistic 3D-based approach for neurosurgery, including multimodal visualization and intuitive interaction with the data for both preoperative planning as well as during the intervention, poses a real benefit.

Part VI

Conclusion

10 Summary

Insight into the human neuronal network is essential for fundamental neuroscience as well as neurosurgical planning. In terms of fundamental neuroscience, the brain remains an object of research since its functioning has yet to be completely mapped. A leading question for neuroscientists is which cortical activation zones are involved in specific tasks. Task-related cortical activity are measured in MRI-based experiments such as fMRI or TMS. In fMRI-based experiments, activation zones are identified by blood oxygenation. Using TMS, neuroscientists are able to block or stimulate cortical areas with high precision by inducing electrical currents. Tasks range from simple finger tapping, to identifying regions related to processes ranging from movement to complex financial decision making in order to track the physiological process of decision making. The combination of diffusion imaging-based fiber reconstructions and fMRI or TMS provides the ability to corroborate hypotheses concerning task-involved brain activation: White matter fiber pathways link brain activation areas and thus form the basis for bidirectional communication.

Lesion localization, risk structure identification, and access path definition are essential steps in neurosurgical planning procedures: The evaluation of intervention-related structures is vital in order to determine an access path as well as a resection extent that causes minimal postoperative damage. Thus, the identification of major activation zones as well as connecting white matter paths is crucial since damage to either can result in severe postoperative patient impairment.

However, a contribution that aim to solve the mentioned neuroscientific and neurosurgical issues is only put forward if MRI data is sufficiently processed and visualized by software tools. This work comprises an introduction and motivation in Part I, followed by the proposed medical visualization approaches

including intra-voxel diffusion evaluation in Part II, white matter tract reconstruction in Part III, diffusion data visualization in Part IV, as well as a clinical application in Part V. In the following, the contribution of each part is summarized.

The presented work begins with a brief introduction on the history of neuroscience and neuroanatomy. Neuroscientific questions were examined and discussed to provide background knowledge for the following approaches. Principles of molecular diffusion, how diffusion is measured and modeled, as well as possible diffusion distributions are explained in subsequent sections. An important issue of this work is to discuss the contribution of HARDI to neuroscience. For this reason, the challenge provoked by crossing neuronal pathways, as well as adequate diffusion reconstruction and modeling schemes for these configurations is considered in greater detail. The introduction closes with a HARDI dataset description.

HARDI-based diffusion profile classification is essential for subsequent processing. Two indices were introduced: The first (MFC) is a global classification approach which applies a morphological pipeline. The second (ISMI) is a local method which comprises a local ODF analysis. Both approaches arrange diffusion profiles into the classes isotropic diffusion (gray matter) and anisotropic diffusion (white matter). Furthermore, they proved to successfully classify white matter distributions into either one or multiple intra-voxel fiber configurations.

The following part applies the previously developed diffusion index, MFC, to neuronal fiber reconstruction. The deterministic tractography approach uses the previously introduced global diffusion classifier in order to facilitate line propagation in regions with complex fiber configurations. In addition, the approach performs several ODF evaluation steps in order to determine the most appropriate propagation direction. Furthermore, local distance configurations, such as the streamline position within a neuronal bundle, are considered. A phantom and a human brain dataset were used for evaluation and proved the reconstruction power in challenging regions such as fiber crossings and fannings.

Three-dimensional visualization is an important issue after fiber reconstruction. The presented methods include an advanced line rendering approach, a visualization of intra-bundle diffusion characteristics, and an focus and context approach for intersecting neuronal pathways. The first approach focuses on line representations: An efficient GPU-based tube rendering approach was realized in combination with diffusion index color mapping. Furthermore, the depth-dependent halo rendering, proposed by Everts et al. [29] and a screen space ambient occlusion technique are included to facilitate spacial understanding.

The subsequently proposed intra-bundle diffusion visualization approach combines hull visualization with diffusion index information. Underlying bundle anisotropy is mapped on the surface of a fiber encompassing hull by implementing a GPU-based raycasting approach. Local diffusion information reveals the degree of integrity and facilitates the exploration of intra-voxel fiber constellations. Visual enhancements, such as silhouettes, ambient occlusion, and Phong illumination, were applied and evaluated in the course of a user study: The significance as well as the benefit of the approach was proven in the evaluation. In addition, clinical applications in which the approach contributes were named. Despite the novel insight, the method provide, color maps, and illumination methods have to be applied with great care since they alter the appearance and can lead to misinterpretations.

HARDI enables a more precise reconstruction of the interwoven neuronal network due to the advanced acquisition and modeling scheme. However, this fact implies that resulting renderings are more intricate than visualizations resulting from DTI, and interpretation is challenging. Therefore, several focus and context rendering approaches were designed for HARDI fiber visualizations. The proposed approaches use previously introduced fiber and bundle renderings and are divided into inner-bundle and intersecting-bundle visualizations: Inner-bundle visualizations focus on streamlines within one bundle whereas intersecting bundle representations highlight fiber crossing areas by applying cutting techniques. The resulting visualizations emphasize important bundle features while obscuring visual clutter resulting form interwoven line representations.

The last part of this work presents a clinical application of MRI volume visualizations; namely, neurosurgical planning. A multimodal planning tool featuring a combined MRI volume visualization and access path estimation is proposed. Focus and context renderings are applied to determine risk structures, such as vessels, white matter pathways or activation areas within their anatomical background. Furthermore, the definition and evaluation of various access paths is feasible in order to determine the surgical intervention at minimal risk.

11 Outlook

The presented work takes steps towards HARDI data processing, visualization and discusses its contribution to clinical and neuroscientific questions. In addition, visualization and interaction strategies for neurosurgical planning are proposed. However, many challenges and scientific questions remain in terms of MRI processing and visualization which are introduced in the following and were partly published in [63].

Acquisition and reconstruction aspects of HARDI. The presented conclusions of HARDI processing and visualization approaches are essential for future neuro-examinations. However, the main reason why HARDI has yet to be implemented in everyday clinical examinations is that the acquisition time and the MRI parameters such as the required angular resolution, gradient strength, and duration, have yet to be completely defined. Recently several have approaches appeared that can solve the mentioned problem.

Prčkovska et al. [84, 85] made a first step towards defining appropriate diffusion MRI parameters such as b-value, number of gradients, diffusion strength, and diffusion time. The authors propose optimal diffusion parameters such as minimal angular resolutions for HARDI acquisitions for certain fiber crossing configurations. However, they also mentioned the dependency of acquisition parameters on various factors for example the crossing angle of neuronal fibers or the resolution of the image sequence. As a result, an overall solution for HARDI acquisition parameters is challenging and undefined.

Spherical ridgelets present, similar to SHs, a set of spherical basis functions to represent the diffusion signal. Using spherical ridgelets for ODF reconstruction and modeling enables compressed sensing, a sampling technique which assumes a sparse MRI signal. As follows, the acquisition time for HARDI can be

reduced and therefore a similar timing to DTI is obtained. This makes HARDI feasible for clinical implementation.

Global diffusion indices for HARDI. In this work, two diffusion classification indices were proposed which classify white matter diffusion profiles into single and multiple intra-voxel fiber populations. However, an interesting issue is the further classification of multiple diffusion profiles. In particular, the differentiation of fanning, crossing, and kissing distributions. This discrimination has great potential in diffusion imaging since subsequent tractography algorithms benefit from it: The propagation direction can be determined according to the underlying fiber course. As follows, a simple tractography approach is sufficient. However, global approaches are required in order to clearly identify the intra-voxel fiber distribution: Due to acquisition issues, noise, and modeling artifacts, HARDI-based postprocessing approaches have to handle ambiguous local ODFs.

Savadjiev et al. [105] made a first step towards a more precise voxel classification using information about the diffusion distribution in the neighborhood of the current voxel. The authors introduce a curve inference method to reconstruct fiber courses. Thereby, the differentiation between curving and fanning fiber courses is feasible.

In the work of Engelhardt [28], different diffusion reconstruction methods as well as methods defining the fODF are investigated. Based on the resulting diffusion PDFs, anisotropy classifiers are proposed which aim to differentiate the intra-voxel fiber distribution in greater detail. To accomplish this task, global diffusion information is incorporated into classification: The ODF maximum of neighboring voxels is examined for current ODF maximum evaluation.

Advanced tractography methods for HARDI. A contribution of this work is the development of a deterministic tractography approach using HARDI. Streamline approaches reconstruct neuronal pathways individually. Contrary to this local approach, global fiber tractography considers the whole neuronal network and is consequently more advantageous than local reconstructions. However,

their computational complexity and the accompanying long reconstruction time which is not clinically feasible stands against them.

As a result, efficient implementation of global tractography approaches poses an interesting contribution to HARDI fiber reconstruction. Reisert et al. [89] proposed a first global reconstruction method which is applicable in a clinical environment. The authors demonstrated the reconstruction power of the algorithm using a fiber phantom.

HARDI visualization.   HARDI provokes visualization issues that differ from DTI due to the potentially interwoven fiber tracts. Several approaches towards a user-friendly examination of the data were proposed in the course of this work. The introduced methods pose initial approaches to visualizing the detailed information provided by the ODF but at the same time avoid visual clutter. An interesting issue is the user interaction with these HARDI visualizations in order to gain more information on demand.

In addition, issues such as the estimation and visualization of uncertainty, which is a current research topic, is also interesting in terms of HARDI: Changes in acquisition protocols and reconstructing settings, such as ODF classification or tractography parameters, can lead to different neuronal pathway results. Brecheisen et al. [14] proposed an approach to visualize the impact of tractography parameters for DTI. Similar approaches can be beneficial for HARDI as well.

Clinical implementation and evaluation of approaches.   This thesis discusses two state of the art issues in neuro-visualizations: the processing and visualization of HARDI data and neurosurgical planning. At the current state, both aspects can not be combined since the acquisition of HARDI datasets for neurosurgical cases is challenging. However, all presented visualizations discuss potential clinical applications such as answering the question if white matter is infiltrated or displaced by a lesion. Therefore, further evaluation of advanced diffusion imaging and visualization methods is needed in order to contribute to neurosurgical planning.

The implementation of HARDI tractography into a TMS navigation system has great potential to resolve neuronal connections more accurate. This is of special interest in fundamental neuroscience where small pathways are involved in complex tasks.

Bibliography

[1] IEEE visualization contest 2010: Multimodal visualization for neurosurgical planning. `http://viscontest.sdsc.edu/2010`, last accessed September 2012.

[2] The Fiber Cup: A tractography contest at the MICCAI conference 2009. `http://www.lnao.fr/spip.php?rubrique79`, last accessed September 2012.

[3] AGANJ, I., LENGLET, C., AND SAPIRO, G. ODF reconstruction in Q-ball imaging with solid angle consideration. In *IEEE International Symposium on Biomedical Imaging: From Nano to Macro (ISBI)* (2009), pp. 1398–1401.

[4] BASSER, P. J., MATTIELLO, J., AND LEBIHAN, D. MR diffusion tensor spectroscopy and imaging. *Biophysics 66*, 1 (1994), 259–267.

[5] BASSER, P. J., PAJEVIC, S., PIERPAOLI, C., DUDA, J., AND ALDROUBI, A. In vivo fiber tractography using DT-MRI data. *Magnetic Resonance in Medicine 44*, 4 (2000), 625–632.

[6] BASSER, P. J., AND PIERPAOLI, C. Microstructural features measured using diffusion tensor imaging. *Jounal of Magnetic Resonance* (1996), 209–219.

[7] BEAR, M., CONNORS, B., PARADISO, M., BEAR, M. F., CONNORS, B. W., AND PARADISO, M. A. *Neuroscience: Exploring the Brain*, second ed. Lippincott Williams & Wilkins, 2001.

[8] BEHRENS, T., JOHANSEN-BERG, H., JBABDI, S., RUSHWORTH, M., AND WOOLRICH, M. Probabilistic diffusion tractography with multiple fibre orientations: What can we gain? *NeuroImage 34*, 1 (2007), 144–155.

[9] BERMAN, J. I., CHUNG, S., MUKHERJEE, P., HESS, C. P., HAN, E. T., AND HENRY, R. G. Probabilistic streamline Q-ball tractography using the residual bootstrap. *NeuroImage 39*, 1 (2008), 215–222.

[10] BEYER, J., HADWIGER, M., WOLFSBERGER, S., AND B, K. High-quality multimodal volume rendering for preoperative planning of neurosurgical interventions. *IEEE Transactions on Visualization and Computer Graphics 13* (2007), 1696–1703.

[11] BLAAS, J., BOTHA, C., PETERS, B., VOS, F., AND POST, F. Fast and reproducible fiber bundle selection in DTI visualization. In *IEEE Visualization (VIS)* (2005), pp. 59–64.

[12] BLAAS, J., BOTHA, C. P., MAJOIE, C., NEDERVEEN, A., VOS, F. M., AND POST, F. H. Interactive visualization of fused fMRI and DTI for planning brain tumor resections. In *SPIE Medical Imaging* (2007), vol. 6509. paper nr 6509-60.

[13] BORN, S., WELLEIN, D., RHONE, P., PFEIFLE, M., FRIEDRICH, J., AND BARTZ, D. Neurosurgical intervention planning with VolV. IEEE Visualization Contest 2010 - Honorable Mention Submission, sep 2010.

[14] BRECHEISEN, R., PLATEL, B., VILANOVA, A., AND TER HAAR ROMENY, B. Parameter sensitivity visualization for DTI fiber tracking. *IEEE Transactions on Visualization and Computer Graphics 15*, 6 (2009), 1441–1448.

[15] BRUCKNER, S., GRIMM, S., KANITSAR, A., AND GRÖLLER, M. E. Illustrative context-preserving volume rendering. In *IEEE/Eurographics Symposium on Visualization (EuroVis)* (2005), pp. 69–76.

[16] BURDACH, K. F. *Vom Baue und Leben des Gehirns.* Leipzig (Dyk), 1819-1826.

[17] CAMPBELL, J. S. W., SIDDIQI, K., RYMAR, V. V., SADIKOT, A. F., AND PIKE, B. G. Flow-based fiber tracking with diffusion tensor and Q-ball data: Validation and comparison to principal diffusion direction techniques. *NeuroImage 27*, 4 (2005), 725–736.

[18] CHAO, Y.-P., CHEN, J.-H., CHO, K.-H., YEH, C.-H., CHOU, K.-H., AND LIN, C.-P. A multiple streamline approach to high angular resolution diffusion tractography. *Medical Engineering & Physics 30*, 8 (2008), 989–996.

[19] CHEN, W., ZHANG, S., CORREIA, S., AND EBERT, D. S. Abstractive representation and exploration of hierarchically clustered diffusion tensor fiber tracts. *Computer Graphics Forum 27*, 3 (2008), 1071–1078.

[20] CHEN, Y., GUO, W., ZENG, Q., YAN, X., HUANG, F., ZHANG, H., HE, G., VEMURI, B. C., AND LIU, Y. Estimation, smoothing, and characterization of apparent diffusion coefficient profiles from high angular resolution DWI. In *Computer Vision and Pattern Recognition* (2004), pp. 588–593.

[21] DESCOTEAUX, M., ANGELINO, E., FITZGIBBONS, S., AND DERICHE, R. Apparent diffusion coefficients from high angular resolution diffusion images: Estimation and applications. *Magnetic Resonance in Medicine 56*, 2 (2006), 395–410.

[22] DESCOTEAUX, M., ANGELINO, E., AND S. FITZGIBBONS, R. D. Regularized, fast and robust analytical Q-ball imaging. *Magnetic Resonance in Medicine 58*, 3 (2007), 497–510.

[23] DESCOTEAUX, M., DERICHE, R., KNÖSCHE, T. R., AND ANWANDER, A. Deterministic and probabilistic tractography based on complex fibre orientation distributions. *IEEE Transactions on Medical Imaging 28*, 2 (2009), 269–286.

[24] DIEPENBROCK, S., PRASSNI, J.-S., LINDEMANN, F., BOTHE, H.-W., AND ROPINSKI, T. Pre-operative planning of brain tumor resections. IEEE Visualization Contest 2010 - Winning Entry, 2010.

[25] DIEPENBROCK, S., PRASSNI, J.-S., LINDEMANN, F., BOTHE, H.-W., AND ROPINSKI, T. Interactive Visualization Techniques for Neurosurgery Planning. *Eurographics (Short Papers)* (2011).

[26] EICHELBAUM, S., HLAWITSCHKA, M., HAMANN, B., AND SCHEUER-
MANN, G.   Image-space tensor field visualization using a LIC-like
method.   In *Visualization in Medicine and Life Sciences 2*, L. Linsen,
B. Hamann, H. Hagen, and H.-C. Hege, Eds., Mathematics and Visual-
ization. Springer-Verlag, 2012, pp. 193–210.

[27] EINSTEIN, A. Über die von der molekularkinetischen Theorie der Wärme
geforderte Bewegung von in ruhenden Flüssigkeiten suspendierenden
Teilchen. *Annalen der Physik 17* (1905), 549–569.

[28] ENGELHARDT, S. Developing a voxel classifier using high angular reso-
lution diffusion data, 2012.

[29] EVERTS, M. H., BEKKER, H., ROERDINK, J. B., AND ISENBERG, T. Depth-
dependent halos: Illustrative rendering of dense line data. *IEEE Transac-
tions on Visualization and Computer Graphics 15* (2009), 1299–1306.

[30] FILLARD, P., DESCOTEAUX, M., GOH, A., GOUTTARD, S., JEURISSEN,
B., MALCOLM, J., RAMIREZ-MANZANARES, A., REISERT, M., SAKAIE,
K., TENSAOUTI, F., YO, T., MANGIN, J.-F., AND POUPON, C. Quantita-
tive evaluation of 10 tractography algorithms on a realistic diffusion MR
phantom. *NeuroImage 56*, 1 (2011), 220–34.

[31] FRANK, L. R.   Characterization of anisotropy in high angular resolu-
tion diffusion-weighted MRI. *Magnetic Resonance in Medicine 47*, 6 (2002),
1083–1099.

[32] FUHRMANN, A., AND GRÖLLER, E.   Real-time techniques for 3D flow
visualization. In *IEEE Visualization (VIS)* (1998), pp. 305–312.

[33] GASTEIGER, R., NEUGEBAUER, M., BEUING, O., AND PREIM, B.   The
FLOWLENS: A Focus-and-Context visualization approach for explo-
ration of blood flow in cerebral aneurysms. *IEEE Transactions on Visu-
alization and Computer Graphics 17*, 12 (2011), 2183–2192.

[34] GOH, A. Deterministic tractography using orientation distribution functions estimated with probability density constraints and spatial regularity. In *MICCAI workshop on Diffusion Modelling and the Fiber Cup* (2009).

[35] GOLDAU, M., WIEBEL, A., HLAWITSCHKA, M., SCHEUERMANN, G., AND TITTGEMEYER, M. Visualizing DTI parameters on boundary surfaces of white matter fiber bundles. In *International Conference on Computer Graphics and Imaging (IASTED)* (2011), pp. 53–61.

[36] GRAY, H. *Gray's Anatomy of the Human Body*. 1918.

[37] HAGMANN, P., JONASSON, L., MAEDER, P., THIRAN, J.-P., WEDEEN, V. J., AND MEULI, R. Understanding diffusion MR imaging techniques: From scalar diffusion-weighted imaging to diffusion tensor imaging and beyond. *Radiographics 26*, Suppl 1 (2006), 205–223.

[38] HAHN, E. L. Spin echoes. *Physical Review 80* (1950), 580–594.

[39] HAHN, H. K., KLEIN, J., NIMSKY, C., REXILIUS, J., AND PEITGEN, H.-O. Uncertainty in diffusion tensor based fibre tracking. In *Medical Technologies in Neurosurgery*, vol. 98. 2006, pp. 33–41.

[40] HANNULA, H., NEUVONEN, T., SAVOLAINEN, P., HILTUNEN, J., MA, Y.-Y. Y., ANTILA, H., SALONEN, O., CARLSON, S., AND PERTOVAARA, A. Increasing top-down suppression from prefrontal cortex facilitates tactile working memory. *NeuroImage 49*, 1 (2009), 1091–1098.

[41] HARDENBERGH, J., BUCHBINDER, B. R., THURSTON, S. A. M., LOMBARDI, J. W., AND HARRIS, G. J. Integrated 3D visualization of fMRI and DTI tractography. In *IEEE Visualization (VIS)* (2005), pp. 94–95.

[42] JEURISSEN, B., LEEMANS, A., TOURNIER, J.-D., AND SIJBERS, J. Fiber tracking on the Fiber Cup phantom using constrained spherical deconvolution. In *MICCAI workshop on Diffusion Modelling and the Fiber Cup* (2009).

[43] JIANU, R., DEMIRALP, C., AND LAIDLAW, D. Exploring 3D DTI fiber tracts with linked 2D representations. *IEEE Transactions on Visualization and Computer Graphics 15*, 6 (2009), 1449–1456.

[44] JOHANSEN-BERG, H., AND BEHRENS, T. E., Eds. *Diffusion MRI: From quantitative measurements to in vivo neuroanatomy.* Elsevier, 2009.

[45] JONES, D. K., Ed. *Diffusion MRI: Theory, Methods and Applications.* Oxford University Press, 2010.

[46] JONES, D. K., HORSFIELD, M. A., AND SIMMONS, A. Optimal strategies for measuring diffusion in anisotropic systems by magnetic resonance imaging. *Magnetic Resonance in Medicine 42*, 3 (1999), 515–525.

[47] JOSHI, A., SCHEINOST, D., VIVES, K., SPENCER, D., STAIB, L., AND PAPADEMETRIS, X. Novel interaction techniques for neurosurgical planning and stereotactic navigation. *IEEE Transactions on Visualization and Computer Graphics 14*, 6 (2009), 1587–1594.

[48] KADEN, E., ANWANDER, A., AND KNÖSCHE, T. R. Variational inference of the fiber orientation density using diffusion MR imaging. *NeuroImage 42*, 4 (2008), 1366–1380.

[49] KINDLMANN, G. Superquadric tensor glyphs. In *IEEE TVCG/EG Symposium on Visualization* (2004), pp. 147–154.

[50] KINDLMANN, G., AND WESTIN, C.-F. Diffusion tensor visualization with glyph packing. *IEEE Transactions on Visualization and Computer Graphics 12*, 5 (September-October 2006), 1329–1335.

[51] KLEIN, J., BARBIERI, S., STUKE, H., BAUER, M., EGGER, J., NIMSKY, C., AND HAHN, H. *Neuroimaging*, vol. 176. 2010, ch. On the Reliability of Diffusion Neuroimaging, pp. 1–24.

[52] KLEIN, J., HERMANN, S., KONRAD, O., HAHN, H. K., AND PEITGEN, H.-O. Automatic quantification of DTI parameters along fiber bundles. In *Bildverarbeitung für die Medizin (BVM)* (2007), pp. 272–276.

[53] KLEISER, R., STAEMPFLI, P., VALAVANIS, A., BOESIGER, P., AND KOLLIAS, S. Impact of fMRI-guided advanced DTI fiber tracking techniques on their clinical applications in patients with brain tumors. *Neuroradiology 52*, 1 (2010), 37–46.

[54] KRÜGER, J., AND FOGAL, T. Focus and context-visualization without the complexity. In *World Congress on Medical Physics and Biomedical Engineering* (2009), Springer, pp. 45–48.

[55] KRÜGER, J., SCHNEIDER, J., AND WESTERMANN, R. ClearView: An interactive context preserving hotspot visualization technique. *IEEE Transactions on Visualization and Computer Graphics 12*, 5 (2006), 941–948.

[56] LANDGRAF, P., MERHOF, D., AND RICHTER, M. Anisotropy of HARDI diffusion profiles based on the L2-Norm. In *Bildverarbeitung für die Medizin (BVM)* (2011), pp. 239–243.

[57] LAZAR, M., WEINSTEIN, D. M., TSURUDA, J. S., HASAN, K. M., ARFANAKIS, K., MEYERAND, M. E., BADIE, B., ROWLEY, H. A., HAUGHTON, V., FIELD, A., AND ALEXANDER, A. L. White matter tractography using diffusion tensor deflection. *Human Brain Mapping 18*, 4 (2003), 306–321.

[58] LINK, F., KOENIG, M., AND PEITGEN, H.-O. Multi-resolution volume rendering with per object shading. In *Vision, Modeling, and Visualization* (2006), pp. 185–191.

[59] LORENSEN, W. E., AND CLINE, H. E. Marching Cubes: A high resolution 3D surface construction algorithm. *Computer Graphics 21*, 4 (1987), 163–169.

[60] MANSSOUR, I. H., FURUIE, S. S., OLABARRIAGA, S. D., AND FREITAS, C. M. D. S. Visualizing inner structures in multimodal volume data. In *Brazilian Symposium on Computer Graphics and Image Processing (SIBGRAPI)* (2002), pp. 51–58.

[61] MERHOF, D., GREINER, G., BUCHFELDER, M., AND NIMSKY, C. Fiber selection from diffusion tensor data based on Boolean operators. In *Bildverarbeitung für die Medizin (BVM)* (2010), pp. 147–151.

[62] MERHOF, D., MEISTER, M., E., B., NIMSKY, C., AND G., G. Isosurface-based generation of hulls encompassing neuronal pathways. *Stereotactic and Functional Neurosurgery, 87* (2009), 50–60.

[63] MERHOF, D., RÖTTGER, D., AND NIMSKY, C. Diffusionsbildgebung - trends und aktuelle entwicklung. In *GI Informatik 2012 Workshop: Trends und aktelle Entwicklung für die computerassistierte Neurochirurgie* (2012), pp. 1–9.

[64] MERHOF, D., SONNTAG, M., ENDERS, F., NIMSKY, C., HASTREITER, P., AND GREINER, G. Hybrid visualization for white matter tracts using triangle strips and point sprites. *IEEE Transactions on Visualization and Computer Graphics 12* (2006), 1181–1188.

[65] MEVIS MEDICAL SOLUTIONS AG. MeVisLab, medical image processing and visualization. `http://www.mevislab.de`, last accessed September 2012.

[66] MEYNERT, T. *Psychiatry: A clinical treatise on diseases of the fore-brain based upon a study of its structure, functions, and nutrition*. New York: G.P. Putnam's Sons, 1885.

[67] MITTRING, M. Finding next Gen - CryEngine 2. In *ACM SIGGRAPH 2007 courses* (2007), pp. 97–121.

[68] MORI, S., CRAIN, B. J., CHACKO, V., AND VAN ZIJL, P. C. Three-dimensional tracking of axonal projections in the brain by magnetic resonance imaging. *Magnetic Resonance Imaging 45*, 2 (1999), 265–269.

[69] MORI, S., WAKANA, S., VAN ZIJL, P. C. M., AND POETSCHER, N. L. M. *MRI Atlas of Human White Matter, First Edition*. Elsevier Science, 2005.

[70] MOSELEY, M. E., COHEN, Y., MINTOROVITCH, J., KUCHARCZYK, J., TSURUDA, J., WEINSTEIN, P., AND NORMAN, D. Evidence of anisotropic self-diffusion. *Radiology 176* (1990), 439–445.

[71] NEXSTIM. Nextim, non-invasive functional mapping of the cortex. `http://www.nexstim.com/`, last accessed September 2012.

[72] NIMSKY, C., GANSLANDT, O., ENDERS, F., MERHOF, D., HAMMEN, T., AND BUCHFELDER, M. Visualization strategies for major white matter tracts for intraoperative use. *International Journal of Computer Assisted Radiology and Surgery 1*, 1 (2006), 13–22.

[73] NIMSKY, C., GANSLANDT, O., HASTREITER, P., WANG, R., BENNER, T., SORENSEN, A. G., AND FAHLBUSCH, R. Preoperative and intraoperative diffusion tensor imaging-based fiber tracking in glioma surgery. *Neurosurgery 56*, 1 (2005), 130–138.

[74] OTTEN, R., VILANOVA, A., AND WETTERING, H. V. D. Illustrative white matter fiber bundles. *Computer Graphics Forum 29*, 3 (2010), 1013–1022.

[75] PEETERS, T. H. J. M., PRČKOVSKA, V., VAN ALMSICK, M., VILANOVA, A., AND TER HAAR ROMENY, B. Fast and sleek glyph rendering for interactive HARDI data exploration. In *IEEE Pacific Visualization Symposium (PacificVis)* (2009), pp. 153–160.

[76] PERRIN, M., POUPON, C., COINTEPAS, Y., RIEUL, B., GOLESTANI, N., PALLIER, C., RIVIÈRE, D., CONSTANTINESCO, A., LE BIHAN, D., AND MANGIN, J.-F. Fiber tracking in Q-ball fields using regularized particle trajectories. In *Information Processing in Medical Imaging (IPMI)* (2005), pp. 52–63.

[77] PETROVIC, V., FALLON, J., AND KUESTER, F. Visualizing whole-brain DTI tractography with gpu-based tuboids and lod management. *IEEE Transactions on Visualization and Computer Graphics 13*, 6 (2007), 1488–1495.

[78] POST, F., VROLIJK, B., HAUSER, H., LARAMEE, R., AND DOLEISCH, H. The state of the art in flow visualization: Feature extraction and tracking. *Computer Graphics Forum 4*, 22 (2003), 775–792.

[79] POUPON, C., LARIBIÈRE, L., TOURNIER, G., BERNARD, J., FOURNIER, D., FILLARD, P., DESCOTEAUX, M., AND MANGIN, J.-F. A diffusion hardware phantom looking like a coronal brain slice. In *8th Annual Meeting of the ISMRM* (2010). abstract number 1270.

[80] POUPON, C., POUPON, F., ALLIROL, L., AND MANGIN, J.-F. A database dedicated to anatomo-functional study of human brain connectivity. In *12th HBM Neuroimage* (2006), no. 646.

[81] POUPON, C., RIEUL, B., KEZELE, I., PERRIN, M., POUPON, F., AND J.F., M. New diffusion phantoms dedicated to the study and validation of HARDI models. *Magnetic Resonance in Medicine 60*, 6 (2008), 1276–1283.

[82] PREIM, B., AND BARTZ, D. *Visualization in Medicine: Theory, Algorithms, and Applications (The Morgan Kaufmann Series in Computer Graphics)*. Morgan Kaufmann Publishers Inc., San Francisco, CA, USA, 2007.

[83] PREIM, B., TIETJEN, C., AND DÖRGE, C. NPR, focussing and emphasis in medical visualizations. In *Simulation und Visualisierung 2005 (SimVis)* (2005), pp. 139–152.

[84] PRČKOVSKA, V. *High Angular Resolution Diffusion Imaging. Processing and Visualization.* PhD thesis, Eindhoven University of Technology, October 2010.

[85] PRČKOVSKA, V., ROEBROECK, A., PULLENS, P., VILANOVA, A., AND TER HAAR ROMENY, B. Optimal acquisition schemes in high angular resolution diffusion weighted imaging. In *Medical Image Computing and Computer-Assisted Intervention (MICCAI)* (2008), pp. 9–17.

[86] REIL, J. Band XI, Tafel XIII, 1812.

[87] REIL, J. C. Das Balken-System oder die Hirnschenkel-Organisation im großen Gehirn. *Archiv für die Physiologie 9* (1809), 172–195.

[88] REINA, G., BIDMON, K., ENDERS, F., HASTREITER, P., AND ERTL, T. GPU-Based hyperstreamlines for diffusion tensor imaging. In *EuroVis* (2006), pp. 35–42.

[89] REISERT, M., MADER, I., ANASTASOPOULOS, C., WEIGEL, M., SCHNELL, S., AND KISELEV, V. G. Global fiber reconstruction becomes practical. *NeuroImage 54*, 2 (2011), 955–962.

[90] REISERT, M., MADER, I., AND KISELEV, V. Global reconstruction of neu-ronal fibres. In *MICCAI workshop on Diffusion Modelling and the Fiber Cup* (2009).

[91] RIEDER, C., RITTER, F., RASPE, M., AND PEITGEN, H.-O. Interactive visualization of multimodal volume data for neurosurgical tumor treat-ment. *Computer Graphics Forum 27*, 3 (2008), 1055–1062.

[92] ROPINSKI, T., STEINICKE, F., AND HINRICHS, K. H. Interactive importance-driven visualization techniques for medical volume data. In *International Fall Workshop on Vision, Modeling, and Visualization (VMV05)* (2005), pp. 273–280.

[93] RÖTTGER, D., DENTER, C., AND MÜLLER, S. Advanced line visualization for HARDI. In *Bildverarbeitung für die Medizin (BVM)* (2012), pp. 153–158.

[94] RÖTTGER, D., DUDAI, D., MERHOF, D., AND MÜLLER, S. Bundle visu-alization strategies for HARDI characteristics. In *International Symposium on Visual Computing (ISVC)* (2012), Lecture Notes in Computer Science, pp. 326–335.

[95] RÖTTGER, D., DUDAI, D., MERHOF, D., AND MÜLLER, S. ISMI: A clas-sification index for high angular resolution diffusion imaging. In *SPIE Medical Imaging* (2012). paper nr 8314-158.

[96] RÖTTGER, D., DUDAI, D., MERHOF, D., AND MÜLLER, S. Visualization and evaluation of intra-bundle diffusion characteristics. In *GI Informatik 2012 Workshop: Trends und aktelle Entwicklung für die computerassistierte Neurochirurgie* (2012), pp. 1–11.

[97] RÖTTGER, D., ENGELHARDT, S., DENTER, C., GÜSSEFELD, B., ANNETTE, H., LOCHMANN, G., OSPELT, D., PASCHKE, J., TAO, Q., AND MÜLLER, S. An exploration and planning tool for neurosurgical interventions. IEEE Visualization Contest 2010 - Honorable Mention Submission, 2010.

[98] RÖTTGER, D., ENGELHARDT, S., AND MÜLLER, S. Multimodal visualizations for pre-operative neurosurgical planning. In *GI Informatik 2011 Workshop: Emerging Technologies for Medical Diagnosis and Therapy* (2011).

[99] RÖTTGER, D., MERHOF, D., AND MÜLLER, S. The BundleExplorer: A focus and context rendering framework for complex fiber distributions. In *Eurographics Workshop on Visual Computing for Biology and Medicine* (2012), pp. 1–8.

[100] RÖTTGER, D., SEIB, V., AND MÜLLER, S. Distance-based tractography in high angular resolution diffusion MRI. *The Visual Computer 27* (2011), 729–738.

[101] RÖTTGER, D., SEIB, V., AND MÜLLER, S. MFC: A morphological fiber classification approach. In *Bildverarbeitung für die Medizin (BVM)* (2011), pp. 364–368.

[102] SAITO, T., AND TAKAHASHI, T. Comprehensible rendering of 3-D shapes. In *Computer graphics and interactive techniques* (1990), SIGGRAPH, pp. 197–206.

[103] SATO, Y., NAKAJIMA, S., ATSUMI, H., KOLLER, T., GERIG, G., YOSHIDA, S., AND KIKINIS, R. 3D multi-scale line filter for segmentation and visualization of curvilinear structures in medical images. In *CVRMed-MRCAS* (1997), Lecture Notes in Computer Science, pp. 213–222.

[104] SAVADJIEV, P., CAMPBELL, J. S. W., DESCOTEAUX, M., DERICHE, R., PIKE, G. B., AND SIDDIQI, K. Labeling of ambiguous sub-voxel fibre bundle configurations in high angular resolution diffusion MRI. *NeuroImage 41*, 1 (2008), 58–68.

[105] SAVADJIEV, P., CAMPBELL, J. S. W., DESCOTEAUX, M., DERICHE, DR., R., PIKE, G. B., AND SIDDIQI, K. Labeling of ambiguous sub-voxel fibre bundle configurations in high angular resolution diffusion MRI. *NeuroImage 41*, 1 (2008), 58–68.

[106] SEELEY, R. R., STEPHENS, T. D., AND TATE, P. *Anatomy and Physiology*. McGraw-Hill, 2000.

[107] SEIGNEURET, J. F., JANNIN, P., FLEIG, O. J., SEIGNEURET, E., MOR, X., RAIMBAULT, M., AND CEDEX, R. Multimodal and multi-informational neuronavigation. In *Computer Assisted Radiology and Surgery (CARS)* (2000), pp. 167–172.

[108] SHAMIR, R., FREIMAN, M., JOSKOWICZ, L., SHOHAM, M., ZEHAVI, E., AND SHOSHAN, Y. Robot-assisted image-guided targeting for minimally invasive neurosurgery: Planning, registration, and in-vitro experiment. In *Medical Image Computing and Computer Assisted Intervention (MICCAI)* (2005), pp. 131–138.

[109] STEJSKAL, E. O., AND TANNER, J. E. Spin diffusion measurements: Spin echoes in the presence of a time-dependent field gradient. *The Journal of Chemical Physics 42*, 1 (1965), 288–292.

[110] TALOS, I.-F., DONNELL, L. O., WESTIN, C.-F., WARFIELD, S. K., III, W. W., YOO, S.-S., PANYCH, L. P., GOLBY, A., MAMATA, H., MAIER, S. S., RATIU, P., AND GUTTMANN, C. R. G. Diffusion tensor and functional MRI fusion with anatomical MRI for image-guided neurosurgery. In *Medical Image Computing and Computer Assisted Intervention (MICCAI)* (2003), pp. 407–415.

[111] TIETJEN, C., ISENBERG, T., AND PREIM, B. Combining silhouettes, surface, and volume rendering for surgery education and planning. In *IEEE/Eurographics Symposium on Visualization (EuroVis)* (2005), pp. 303–310.

[112] TORREY, H. C. Bloch Equations with Diffusion Terms. *Physical Review 104*, 3 (1956), 563–565.

[113] TOURNIER, J.-D., CALAMANTE, F., AND CONNELLY, A. Robust determination of the fibre orientation distribution in diffusion MRI: Non-negativity constrained super-resolved spherical deconvolution. *NeuroImage 35*, 4 (2007), 1459–1472.

[114] TOURNIER, J.-D., CALAMANTE, F., GADIAN, D. G., AND CONNELLY, A. Direct estimation of the fiber orientation density function from diffusion-weighted MRI data using spherical deconvolution. *NeuroImage 23*, 3 (2004), 1176–1185.

[115] TSUCHIYA, K., MIZUTANI, Y., AND HACHIYA, J. Preliminary evaluation of fluid-attenuated incersion-recovery MR in the diagnosis of intracranial tumors. *American Journal of Neuroradiology 17*, 6 (1996), 1081–1086.

[116] TUCH, D. S. *Diffusion MRI of Complex Tissue Structure*. PhD thesis, Massachusetts Institute Of Technonogy, 2002.

[117] TUCH, D. S. Q-ball imaging. *Magnetic Resonance in Medicine 52*, 6 (2004), 1358–1372.

[118] TUCH, D. S., REESE, T. G., WIEGELL, M. R., AND WEDEEN, V. J. Diffusion MRI of complex neural architecture. *Neuron 40*, 5 (2003), 885–895.

[119] VILANOVA, A., BERENSCHOT, G., AND VAN DE PUL, C. DTI visualization with streamsurfaces and evenly-spaced volume seeding. In *Symposium on Visualization (VisSym)* (2004), pp. 173–182, 347.

[120] VILANOVA, A., ZHANG, S., KINDLMANN, G., AND LAIDLAW, D. An introduction to visualization of diffusion tensor imaging and its applications. In *Visualization and Image Processing of Tensor Fields*. Springer-Verlag, 2005, pp. 121–153.

[121] VIOLA, I., KANITSAR, A., AND GRÖLLER, M. E. Importance-driven volume rendering. In *IEEE Visualization (VIS)* (2004), pp. 139–145.

[122] WANG, L., ZHAO, Y., MUELLER, K., AND KAUFMAN, A. The magic volume lens: An interactive focus+context technique for volume rendering. In *IEEE Visualization (VIS)* (2005), pp. 367–374.

[123] WEDEEN, V., REESE, T., TUCH, D., WEIGEL, M., DOU, J.-G., WEISKOFF, R., AND CHESSLER, D. Mapping fiber orientation spectra in cerebral white matter with fourier-transform diffusion MRI, 2000.

[124] WEDEEN, V., WANG, R., SCHMAHMANN, J., BENNER, T., TSENG, W., DAI, G., PANDYA, D., HAGMANN, P., D'ARCEUIL, H., AND DE CRESPIGNY, A. Diffusion spectrum magnetic resonance imaging (DSI) tractography of crossing fibers. *NeuroImage 41*, 4 (2008), 1267–1277.

[125] WEI, C., ZHANG, S., CORREIA, S., AND TATE, D. F. Visualizing diffusion tensor imaging data with merging ellipsoids. In *IEEE Pacific Visualization Symposium (PacificVis)* (2009), pp. 145–151.

[126] WEINSTEIN, D., KINDLMANN, G., AND LUNDBERG, E. Tensorlines: Advection-diffusion based propagation through diffusion tensor fields, 1999.

[127] WEISKOPF, D. *GPU-Based Interactive Visualization Techniques (Mathematics and Visualization)*. Springer-Verlag New York, Inc., 2006.

[128] WENGER, A., KEEFE, D., ZHANG, S., AND LAIDLAW, D. H. Interactive volume rendering of thin thread structures within multivalued scientific datasets. *IEEE Transactions on Visualization and Computer Graphics 10*, 6 (2004), 664–672.

[129] YUSHKEVICH, P. A., ZHANG, H., SIMON, T., AND GEE, J. C. Structure-specific statistical mapping of white matter tracts. *NeuroImage 41*, 2 (2008), 448–461.

[130] ZHANG, S., DEMIRALP, Ç., AND LAIDLAW, D. H. Visualizing diffusion tensor MR images using streamtubes and streamsurfaces. *IEEE Transactions on Visualization and Computer Graphics 9* (October 2003), 454–462.

[131] ZHUKOV, L., AND BARR, A. H. Oriented tensor reconstruction: Tracing neural pathways from diffusion tensor MRI. In *IEEE Visualization (VIS)* (2002), pp. 387–394.

Curriculum Vitae

Name:	Diana Röttger
Date of birth:	October 18, 1983
Place of birth:	Limburg, Lahn
Nationality:	German

08/2000 - 05/2003	Wirtschaftsgymnasium Westerburg
05/2003	Graduation: High school diploma
10/2003 - 01/2009	Undergraduate and graduate studies, University of Koblenz-Landau, Germany Smaller thesis, Department of Information Technology, Lappeenranta University of Technology, Finland Topic: *VisuTeach: Visual Teaching in Image Based Classification Problems* Topic: *Evaluation of 3D Level Set Approaches for the Quantification of Aortic Aneurysms* Diploma thesis, MTI Mittelrhein, Institut für Medizintechnik und Informationsverarbeitung, University of Koblenz-Landau, Germany
01/2009	Graduation: University diploma in Computer Science, degree with high distinction

07/2009 - 03/2013	Research assistant and PhD student, Computer Graphics Research Group, University of Koblenz-Landau, Germany
	08/11–10/11 Visiting researcher, Neuroscience Unit, Institute for Physiology and Biomedicine, University of Helsinki, Finland
	01/13–03/13 Observer, Surgical Planning Laboratory, Brigham and Women's Hospital, Harvard Medical School, Boston, USA